SEPARATION CONTROL USING ZNMF DEVICES:
FLOW PHYSICS AND SCALING LAWS

By

Ye Tian and Louis N. Cattafesta III

Department of Mechanical and Aerospace Engineering
University of Florida

1

REPORT DOCUMENTATION PAGE

Public reporting burden for this collection of information is estimated to average 1 hour per response, including the time for reviewing instructions, searching data sources, gathering and maintaining the data needed, and completing and reviewing the collection of information. Send comments regarding this burden estimate or any other aspect of this collection of information, including suggestions for reducing this burden to Washington Headquarters Service, Directorate for Information Operations and Reports, 1215 Jefferson Davis Highway, Suite 1204, Arlington, VA 22202-4302, and to the Office of Management and Budget, Paperwork Reduction Project (0704-0188) Washington, DC 20503.
PLEASE DO NOT RETURN YOUR FORM TO THE ABOVE ADDRESS.

1. REPORT DATE (DD-MM-YYYY)	2. REPORT TYPE Final Technical Report	3. DATES COVERED (From - To) 15 Jan 2005 – 31 Dec 2007

4. TITLE AND SUBTITLE

Separation Control Using ZNMF Devices: Flow Physics and Scaling Laws

5a. CONTRACT NUMBER

FA9550-05-1-0093

5b. GRANT NUMBER

5c. PROGRAM ELEMENT NUMBER

6. AUTHOR(S)

Dr. Louis N. Cattafesta

5d. PROJECT NUMBER

5e. TASK NUMBER

5f. WORK UNIT NUMBER

7. PERFORMING ORGANIZATION NAME(S) AND ADDRESS(ES)

Department of Mechanical and Aerospace Engineering
University of Florida
Gainesville FL 32611

8. PERFORMING ORGANIZATION REPORT NUMBER

9. SPONSORING/MONITORING AGENCY NAME(S) AND ADDRESS(ES)

Air Force Office of Scientific Research (AFOSR)
875 N. Arlington St., Rm. 3112
Arlington, VA 22203
Brett Jeffries/NA

10. SPONSOR/MONITOR'S ACRONYM(S)
AFOSR

11. SPONSORING/MONITORING AGENCY REPORT NUMBER

12. DISTRIBUTION AVAILABILITY STATEMENT

DISTRIBUTION A: Approved for public release; distribution unlimited.

AFRL-SR-AR-TR-08-0293

13. SUPPLEMENTARY NOTES

14. ABSTRACT

The primary goal of this research is to implement a closed-loop control system to control separated flow and to evaluate the performance of the controller. A control system that includes an array of actuators, sensors (pressure sensors or lift/drag balance) and a digital controller is proposed to control flow separation in a closed-loop fashion. The first chapter introduces the flow physics and active control approaches of flow separation. It is organized as follows. First, a brief overview of separation control is provided to orient the reader, followed by the motivation. Than a technical background section is presented to review previous work reported in the literature. Finally, the objectives and technical approaches of this research are presented.

15. SUBJECT TERMS

16. SECURITY CLASSIFICATION OF:			17. LIMITATION OF ABSTRACT	18. NUMBER OF PAGES	19a. NAME OF RESPONSIBLE PERSON
a. REPORT Unclassified	b. ABSTRACT Unclassified	c. THIS PAGE Unclassified	Unclassified	104	19b. TELEPONE NUMBER (Include area code) (703)

3

Nomenclature

c	Airfoil chord length
C_D	Drag coefficient (D/qc)
C_L	Lift coefficient (L/qc)
C_p	Static pressure coefficient ($\frac{p - p_\infty}{q}$)
C_μ	Steady momentum coefficient (J/qc)
$\langle C_\mu \rangle$	Oscillatory momentum coefficient ($\langle J \rangle /qc$)
D	Drag
$\dfrac{dC_p}{d(x/c)}$	Pressure recovery coefficient
f_c	Filter cutoff frequency
f_e	Excitation frequency
f_m	Modulation frequency
f_{sep}	Shedding frequency of separated flow (U_∞ / X_{TE})
f_{wake}	Wake shedding frequency (U_∞ / W_{wake})
F^+	Reduced excitation frequency ($f X_{TE} / U_\infty$)
h	Slot width
J	Steady jet momentum ($\rho U_j^2 h$)
$\langle J \rangle$	Oscillatory jet momentum ($\rho u_j^2 h$)
L	Lift
p	Static local pressure
p_∞	Free stream pressure
q	Free stream dynamic pressure ($\rho U_\infty^2 / 2$)
u_j	Oscillatory jet velocity
U_j	Mean jet velocity
U_∞	Free stream velocity
X_{SEP}	Distance from separation points to trailing edge
X_{TE}	Distance from excitation slot to trailing edge
ρ	Air density
θ	Boundary layer momentum thickness
σ_s^2	Variance of signal
σ_n^2	Variance of noise

Abbreviations

AM	Amplitude Modulation
AOA	Angle Of Attack
BM	Burst Modulation
DAQ	Data AcQuisition
DSP	Digital Signal Processing
ID	IDentification
LDV	Laser Doppler Velocimetry
MSE	Mean Square Error
PIV	Particle Image Velocimetry
PM	Pulse Modulation
PSD	Power Spectral Density
SJA	Synthetic Jet Actuator
SNR (dB)	Signal to Noise Ratio

Abstract

Flow separation has severe adverse effects on performance of flow-related devices (e.g., lift loss of aircrafts). Active control of separated flow has received extensive attention as it is able to mitigate or eliminate flow separation effectively. Most research has been open-loop in nature (i.e., manually adjusting control inputs to achieve best results). Closed-loop control of separated flow has many potential advantages over open-loop control, namely optimization in multi-dimensional domain with constraints, adaptability to changing flow conditions, etc. In this research, adaptive closed-loop control is used to reattach the separated flow over a NACA 0025 airfoil using multiple zero-net-mass-flux (ZNMF) actuators that cover the central 33% of the airfoil span. In particular, two distinct approaches are used. Adaptive disturbance rejection algorithms are used to apply dynamic feedback control of separated flow. The closed-loop control results show ~ 7 x improvements in the lift/drag ratio, with a corresponding increase in lift and reduced drag and concomitant reductions in the fluctuating surface pressure spectra. On the other hand, a simplex optimization approach uses the lift and drag measured by a strain-gauge balance for feedback and searches for the optimal actuation parameters in a closed-loop fashion. The constrained optimization results seeking to maximize lift-to-drag ratio are promising and reveal the importance of forcing nonlinear interactions between the shear layer and wake instabilities.

6

1   Introduction

The primary goal of this research is to implement a closed-loop control system to control separated flow and to evaluate the performance of the controller. A control system that includes an array of actuators, sensors (pressure sensors or lift/drag balance) and a digital controller is proposed to control flow separation in a closed-loop fashion.

This first chapter introduces the flow physics and active control approaches of flow separation. It is organized as follows. First, a brief overview of separation control is provided to orient the reader, followed by the motivation. Then a technical background section is presented to review previous work reported in the literature. Finally, the objectives and technical approaches of this research are presented.

1.1   Overview

Flow separation is identified as one of the most important flow phenomena due to its severe adverse effects on flow-related devices. Following the introduction of the concept of the boundary layer by Prandtl (1904), flow separation has received considerable attention in the fluid dynamics community.

Flow separation is the breakaway or detachment of fluid from a solid surface (Greenblatt and Wygnanski 2000). Flow separation incurs a large amount of energy/lift loss and limits the performance of many flow-related devices (e.g., airplanes, diffusers, etc.). Researchers have been trying to eliminate or at least mitigate flow separation for over a century because of its large potential payoff in many applications.

As shown in Figure 1-4, control of separated flow is divided into two main categories: active control and passive control. Active control provides external energy into the flow while passive control does not. Some passive separation control methods, such as geometrical shaping and turbulators (i.e., turbulence generators), are commonly used because of their simplicity and feasibility. On the other hand, tremendous progress has been made in active separation control over the past twenty years. Traditional active separation control methods, such as steady blowing and suction, were initially used to control flow separation (Gad-el-Hak 2000). These methods were able to control of separation to some extent. However, they were far from optimal because the overall energy required input required to gain a meaningful lift increase or drag reduction was comparable to the energy saved via control of separation (Greenblatt and Wygnanski 2000).

Schubauer and Skramstad (1948) first introduced a breakthrough in active flow control: periodic excitation. This technique requires much less energy than traditional steady active methods and accelerates and regulates the generation of large coherent structures that are primarily responsible for the transport of momentum across the flow (Greenblatt and Wygnanski 2000). The increased large coherent structures make the flow more resistant to separation. Periodic excitation has subsequently been shown to be superior to steady boundary layer control methods by many researchers (Seifert 1996; Greenblatt and Wygnanski 2000; Nishri and Wygnanski 1998). Because of these reasons, periodic excitation is now widely used to control flow separation. Optimal excitation locations, waveforms shapes, and frequencies of periodic perturbations have been systematically studied by numerous researchers (Seifert and Pack 2003A, Amitay et al. 2001). Yet none of these studies has used feedback control to "optimize" the excitation waveform.

One of the most important aspects of separation control is the actuation mechanism that introduces periodic perturbations into the flow structure. Internal acoustic excitation (Hsiao et al. 1990; Huang et al. 1987), speakers (Narayanan and Banaszuk 2003), oscillatory blowing valves (Allen et al. 2000), and MEMS-based actuators (Rathnasingham and Breuer 2003), etc. have been investigated. Among these, synthetic jet or zero-net mass flux (ZNMF) actuators have been the focus of significant research for the past decade due to their utility in flow control applications (Glezer and Amitay 2002). ZNMF actuators utilize the working fluid and do not require an external fluid source, which makes them very attractive from a systems implementation perspective. Significant progress has been made in the modeling and design of such devices (Gallas et al. 2003, 2005). More details of the synthetic jet actuators used in this research are described in Chapter 4. The driving frequency, location, and momentum coefficient of the actuation are the primary parameters that characterize their performance (Amitay et al. 2001).

Although separation control has received extensive attention, to date most studies have focused on open-loop separation control. In the author's opinion, this open-loop approach is due to a fluid mechanics bias to avoid using a more complex closed-loop control approach. Closed-loop separation control has the potential to save more energy than open-loop methods (Cattafesta et al. 1997) and make separation control systems adaptable to different flow conditions. Few experimental studies have focused on closed-loop separation control. For example, Allan et al. (2000) attempted to tune a PID controller for closed-loop separation control and showed that the integral gain was the most effective as a result of the large time constant of their low bandwidth actuator system. However, the realized model and controller were simple. Their results merely scratched the surface of what can possibly be accomplished. Therefore, it is believed that control of flow separation using an array of high bandwidth actuators and surface sensors (pressure or shear stress) is an excellent candidate for closed-loop separation control. Hence, implementation of feedback controllers including more advanced modeling and control algorithms to flow separation control is proposed and is the focus of this research.

1.2 Motivation

Numerous applications of separation control, each with significant potential payoffs, have been identified (Greenblatt and Wygnanski 2000). Many separation control strategies have been applied on civil and military aircrafts and underwater vehicles. However, most of the applications are open-loop in nature because of their simplicity. Although some closed-loop separation control research has been done (Allan et al. 2000; Banaszuk et al. 2003, etc), they are not sufficiently developed to be implemented on real vehicles. The goal of this research is to design and implement various closed-loop control systems for control of separated flows and to seek physical insights behind the control schemes. The main advantages of closed-loop separation control potentially include better performance, energy efficiency and adaptability to changing of flow conditions.

1.3 Background

1.3.1 Two-Dimensional Separation Flow Physics

Under the circumstances of an adverse pressure gradient ($dp/dx > 0$), fluid particles are retarded by both the increasing pressure as well as wall skin friction. If the adverse pressure gradient is of sufficient strength, fluid particles near the wall are likely to separate from the wall and move upstream. This is due to the fact that these particles have finite kinetic energy and cannot penetrate far into the adverse pressure gradient region. The flow separates from the boundary layer and forms large scale vortical structures in the separated region (Figure 1-1).

Assuming two-dimensional, incompressible, steady flow with negligible gravity, the streamwise ("x") component of the momentum equation at the wall reduces to

$$u\frac{\partial u}{\partial x} + v\frac{\partial u}{\partial y} = -\frac{1}{\rho}\frac{dp}{dx} + v\left(\frac{\partial^2 u}{\partial x^2} + \frac{\partial^2 u}{\partial y^2}\right) \tag{1}$$

or

$$v\frac{\partial^2 u}{\partial y^2} = \frac{1}{\rho}\frac{dp}{dx} \tag{2}$$

where $v = \mu/\rho$ is the kinematic viscosity, y is the wall normal coordinate, x is the streamwise coordinate with a corresponding u velocity and streamwise pressure gradient dp/dx.

From eqn. (2), we can see that only an adverse pressure gradient ($dp/dx > 0$) can cause a point of inflection in the velocity profile and the curvature changing sign to make the profile S-shape. In this case, separation will occur when the adverse pressure gradient is strong enough to make the right hand side of eqn. (2) positive (shown in Figure 1-1).

1.3.2 Effects of Flow Separation

In the separation region, the normal velocity component significantly increases as well as the thickness of boundary layer. Therefore, the boundary layer approximations are no longer valid and the problem can no longer be solved using boundary layer theory.

Flow separation significantly changes the pressure distribution around the surface. Such deviations are usually detrimental. As an example, Figure 1-3 shows the C_L and C_D of a NACA0025 airfoil versus angle of attack measured by a lift/drag balance at $Re \approx 100,000$. When the angle of attack increases from zero degree, both C_L and C_D increase as expected. However, C_L drops dramatically due to flow separation at about 13 degrees of angle of attack. At the same time, C_D continues to increase beyond the inception of stall. Both of these effects generally have a negative impact on the airplane performance. However, some applications utilize flow separation. For example, the use of spoilers on airplanes during landing reduces the lift and increases drag to allow the brakes to work more efficiently.

More commonly, we want to mitigate or eliminate flow separation. Typical applications of flow separation control include: separation control of various airfoils to increase C_{Lmax} for larger payload (Greenblatt and Wygnanski 2000; Seifert and Pack 2002; etc); to reduce engine power and noise at takeoff (Gad-el-Hak 2000); to increase efficiency of diffusers (i.e. pressure recovery) (Banaszuk et al. 2003); etc.

1.3.3 Control of Flow Separation

Because of the effects mentioned above and the large potential payoff, researchers have been preoccupied with delaying flow separation or eliminating it entirely. As suggested by Cattafesta et al. (2003), the classification of flow control is chosen as shown in Figure 1-4 to be consistent with terminology used in active noise and vibration control. Active control is subdivided into open-loop versus closed-loop control. Closed-loop control can be further classified into quasi-static versus dynamic, the distinction between the two being whether or not the feedback control is performed on a time scale with the dynamical scales of the flow. Since fluid flows are inherently nonlinear (Wu et al. 1998), the standard frequency preservation of a linear system does not hold. Consequently, nonlinear feedback control on a very slow time compared to the characteristic times scales of the flow is, in fact, possible and attractive. In

essence, this so-called quasi-static control becomes a nonlinear optimization problem. This research will investigate both classes of closed-loop control shown in Figure 1-4.

Other fluid dynamic issues have been studied extensively, such as the effects of Reynolds number, frequency, actuator and sensor locations, momentum coefficient, surface curvature, and compressibility, etc.. Although the topic of this research is closed-loop separation control, the results and conclusions from the open-loop control studies should serve as a sound physical basis for effective control and are reviewed below.

1.3.3.1 Open-loop separation control.

Periodic excitation has been shown to be much more effective than steady forcing because it enhances the momentum transport across the flow domain at a substantial reduction in energy expenditure. It accelerates and regulates the generation of large coherent structures that are primarily responsible for the momentum transport across the flow (Greenblatt and Wygnanski 2000). The enhanced momentum transport forces the separated flow to reattach to the surface and form a thick turbulent boundary layer in a time-averaged sense. The reattachment of the boundary layer regains the pressure suction zone on the upper surface of the airfoil and thus enhances the lift performance. Furthermore, the superposition of weak suction on the periodic excitation enhances the receptivity of the separated shear layer to the fundamental excitation frequency and thus the effectiveness of periodic excitation (Seifert and Pack 2002).

Given the improved performance of periodic excitation to control flow separation, researchers have sought to optimize separation control via time-consuming parametric variations. Significant parameters or conditions that affect the performance of separation control have been identified. Although they are discussed separately below, one should keep in mind that these factors are all coupled with each other.

Actuation frequency. First, consider the characteristic flow structures associated with separated flow. Based on previous studies, Mittal et al. (2005) summarize the three situations with regards to separated flow, as shown in Figure 1-5. In post-stall flow (case C in Figure 1-5), leading-edge shear layer rollup and vortex shedding in the wake are two characteristic features (Wu et al. 1998). Huerre and Monkewitz (1990) suggest that this type of shear flow (with a pocket of absolute instability of sufficient size) may display intrinsic dynamics of the same nature as in a closed-flow system, in which disturbances can grow upstream (i.e. global instability). Therefore, it is reasonable to postulate that separated flow over an airfoil acts as a nonlinear multi-frequency closed-flow system. In such a system, the shear layer instability (with characteristic frequency f_{SL}) and the global wake instability (with vortex shedding frequency f_{wake}) may interact with each other in a nonlinear fashion. In case B, a closed separation bubble is present at some distance downstream of the leading edge. In this case there are potentially three characteristic flow frequencies in the separated flow: f_{SL}, f_{wake} and f_{sep}, where the new scale, f_{sep}, corresponds to the characteristic frequency of the separation bubble.

The scales of the three frequencies are $f_{SL} \sim U/\theta_{SL}$, $f_{SL} \sim U/L_{sep}$ and $f_{wake} \sim U/W_{wake}$, where θ_{SL} is the shear layer thickness, L_{sep} is the length of the separation bubble and W_{wake} is the width of wake. Prasad and Williamson (1996) also show that $f_{SL} = A Re^B f_{wake}$, where $A = 0.0235$ and $B = 0.67$. Since there are different relevant length scales that are included in the three characteristic frequencies, one should expect a significant variation in the observed frequency scales and the corresponding optimal frequency.

10

The present study is focused on how flow systems respond to modulated (e.g. AM, BM, PM) unsteady excitations by ZNMF devices targeting the inherent flow instabilities that lead to the presence of these characteristic flow frequencies. The goal is to search for optimal forcing schemes that most effectively mitigate flow separation via nonlinear interaction of the instabilities.

Much research has been conducted to determine what excitation frequencies are most effective for separation control. However, except for the general agreement that periodic excitation is far more effective than steady blowing, the range of optimal actuation frequencies is a current subject of intense debate. A dimensionless actuation frequency is typically defined for this purpose. However, three slightly different definitions have been given for a so-called dimensionless frequency F^+: 1) $F^+ = f_e X_{TE}/U_\infty$, where f_e is the excitation frequency, X_{TE} is the distance from the excitation slot to the trailing edge and U_∞ is the free stream velocity; 2) $F^+ = f_e L_{sep}/U_\infty$, where L_{sep} is the distance from separation to reattachment; and 3) $F^+ = f_e c/U_\infty$, where c is the chord length. These three are nearly identical for post-stall flow (where the separation bubble length is approximately the airfoil chord), but they scale very differently if a closed separation bubble of finite extent is present. One should notice that none of these definitions is related to the shear layer frequency (f_{SL}). Most researchers implicitly ignore this important frequency when studying separation control.

Herein, some results regarding actuation frequency in previous studies are summarized. Among studies that define $F^+ = f_e X_{TE}/U_\infty$, Wygnanski and his colleagues conclude that the optimal excitation frequency is of order unity $F^+ = O(1)$ (Seifert et al. 1996, Nishri and Wygnanski 1998, Greenblatt and Wygnanski 2000) and have found that so-called high frequency fording $F^+ = O(10)$ is ineffective for their airfoil (NACA 0015) and flow conditions. Conversely, using the same definition of F^+, Amitay et al. (2001) found that when the excitation frequency $F^+ \geq O(10)$, the lift-to-pressure drag ratio was larger than that when the excitation frequency $F^+ < 4$. Honohan et al (2000) also suggested that higher reduced frequencies ($F^+ \geq 10$) can be effective. They argued that it is because the high frequency excitation produces a virtual aerodynamic surface modification that thins the turbulent boundary layer and results in a local favorable pressure gradient.

Besides this argument, there may be two other possible reasons accounting for this interesting discrepancy. First, the length-scale X_{TE} may not be appropriate for their airfoil because of the formation of a closed separation bubble. Instead, if L_{sep} were used, this discrepancy might not exist. Second, as mentioned earlier, the shear layer frequency f_{SL} may also be important (Mittal et al 2005). Here, $f_{SL} \propto U/\theta$, where θ is the boundary layer momentum thickness and not X_{TE} or L_{sep}. The different frequency scales are indicative of different flow instabilities that may exist in the flow and, if present, may compete with each other (Wu et al 1998). When periodic excitation is introduced, one or more of these instabilities may be energized. The controlled flow may then be regulated, and thus lift performance may be enhanced. This may explain the observed variations of the optimal excitation frequency.

Along these lines, an innovative forcing approach that uses multiple harmonically related frequencies is presented by Narayanan and Banaszuk (2003). They demonstrated improvements of this new approach versus single frequency sinusoidal forcing in control of separation in a

diffuser, although its effectiveness requires further investigation. To extend this idea further, one can use excitations with multiple frequency components corresponding to the characteristic frequencies mentioned above. This idea will be investigated in this research.

Excitation amplitude. Another key control parameter in a ZMNF device is jet velocity V_J (some characteristic velocity measure, e.g. the peak or an average velocity). In the literature, the jet frequency is usually non-dimensionalized as $F^+ = fL_{sep}/U_\infty$, where L_{sep} is, for example, the length of separation region and U_∞ is the free stream velocity. The jet velocity is usually non-dimensionalized by U_∞. Various researchers have shown that control authority varies monotonically with V_J/U_∞ for a sinusoidal excitation up to some maximum value (Seifert et al. 1993, 1996, 1999; Glezer and Amitay 2002; Mittal and Rampunggoon 2002). In practice, especially in high speed flows, control authority is often lacking. From an efficiency standpoint, it is desirable to control a flow with minimal actuator input.

Modulation signals. Piezoelectric actuators have fast dynamic response and low power consumption. However, the use of piezoelectric actuators has been limited because of the diminution in their response outside a narrow frequency band around their resonance frequency and the need for testing over a wide frequency range due to the issues discussed in the last section.

Wiltse and Glezer (1993) introduced a clever amplitude modulation method to flow control problems to overcome this problem. The piezoelectric actuator is resonantly driven with a carrier waveform, $e(t)$, which is amplitude modulated with a time-harmonic wave train:

$$e(t)=[1+\varepsilon\sin(\omega_m t+\varphi_m)]A_r\sin(\omega_c t) \tag{3}$$

where A_r is the amplitude of the carrier signal, ε is the degree of modulation ($0 \le \varepsilon \le 1$), ω_c is the carrier frequency (or the resonant frequency of the actuator) in rad/s, ω_m is the modulation frequency (which is also the desired excitation frequency or receptive frequency of the flow) in rad/s, and φ_m is the phase of the modulating signal. By using trigonometric identities, one can show that $e(t)$ contains frequency components at ω_c and $\omega_c \pm \omega_m$, However, when the excitation amplitude is high enough, $e(t)$ is demodulated by the nonlinear fluid dynamical system that is associated with the formation and coalescence of nominally spanwise vortices. This nonlinearity results in the presence of ω_c and $\omega_c \pm \omega_m$ and also ω_m in the flow. In practice, ω_c is set at the resonance frequency of the piezoelectric actuator (which is usually $\gg \omega_m$) and ω_m is set at the desired low frequency corresponding to the desired excitation frequency f_e.

Along these lines, other modulation signals such as burst modulation and pulse modulation can also be used. This modulation technique allows the actuator operating at its resonant frequency to generate a significant flow disturbance while effectively manipulating flows at characteristic frequencies of the flow. It provides a much more flexible approach than matching the resonant frequency of the actuator with the receptive frequencies of the flow.

However, some features of the technique should also be kept in mind. First, the actuator is driven continuously near its resonant frequency, so the probability of mechanical failure is greater than when it is driven off resonance. Second, as mentioned above, demodulation of the waveform is due to nonlinearities of the flow and actuator. As a result, feedback controllers

designed based on a linear assumption may not work as desired. This aspect will be studies in this research.

Actuation location. It is argued by many researchers that the optimal actuation location is at the vicinity of the point of separation (Amitay et al. 2001, Seifert et al. 1996, Seifert and Pack 2003). This is physically plausible since the disturbances introduced at this location can most effectively transport momentum between the free shear layer and the separated region. However, this has not been systematically studied because of some practical limitations, namely the difficulty of installing multiple actuators inside an airfoil. Amitay et al. (2001) used an unconventional airfoil that had an aft portion of a symmetric airfoil attached to a circular cylinder forebody with a synthetic jet slot that could be adjusted by rotating the cylinder. They state that the closer the control is located to the observed separation point, the less power is required to reattach the flow. They also made an interesting point that if either the separation location is unknown or practical limitations preclude control near the separation location, the momentum coefficient C_μ may be manipulated to achieve optimal performance.

Besides the effects of actuation location discussed above, the interaction of adjacent synthetic jet actuators has been investigated by Holman et al. (2003). They found that relative phasing between adjacent actuators does not appear to affect the effectiveness of separation control significantly for their airfoil (NACA 0025) and flow conditions ($R_e = 10^5$ and $AOA = 12°$).

In summary, based on the previous studies it is suggested that slightly upstream of the separation location is the "best" place to introduce actuation. Furthermore, a combination of upstream leading edge and downstream trailing edge actuations may also be a good candidate and remains to be investigated (Mittal et al 2005). Wu et al (1998) discuss this idea in the context of the Kutta-Joukowski lift formula ($L=-\rho U\Gamma$), which assumes the flow is incompressible and steady. In the formula, L is the lift, U is free stream velocity and Γ is the circulation (a counterclockwise circulation is assumed positive). Although the separation is an unsteady process, this formula still holds in a time-averaged sense for the entire flow. Based on these arguments, if the combination of leading edge and trailing edge actuation can be designed to alter the circulation of the airfoil, it should be able to control flow separation in some manner.

Effects of Reynolds number and compressibility. It is shown that control of flow separation is insensitive to the Reynolds number at high chord Reynolds numbers of 11~30 million (Seifert and Pack 2003 A, B, Greenblatt and Wygnanski 2000). The Reynolds number has a very weak effect on pressure distributions around the surface, regardless of the Mach number.

On the other hand, strong Reynolds number effects are identified in the airfoil baseline performance at moderately compressible flow conditions (Seifert and Pack 2001). Reynolds number effects weaken as the Mach number increases and a stronger shock wave develops. Compressibility tends to elongate the separation bubble and reduce the capability of periodic excitation to shorten the separation bubble with similar excitation frequencies and momentum (Seifert and Pack 2001).

It is also suggested by Seifert and Pack (2001) that in the presence of shock waves the excitation location should be slightly upstream of the shock wave. If the excitation is introduced well upstream of the shock wave, it has a detrimental effect on lift, drag and wake steadiness.

13

1.3.3.2 Closed-loop separation control

Closed-loop experimental separation control has not yet received significant attention. This section first reviews some development of the micro-electro-mechanical systems (MEMS) based actuators because of their potential importance to high bandwidth closed-loop control systems. Then the limited previous work on closed-loop separation control is presented.

For closed-loop flow control systems, the desired actuators should be fast, power efficient, and reliable. In previous separation control studies, acoustic excitation (Hsiao et al. 1990 and Huang et al. 1987) seems facility dependent because the acoustic drivers stimulate the wind tunnel resonant modes to excite the separated flow; oscillatory blowing valves (Allen et al. 2000) appear to have slow dynamic response; active flexible wall transducers (Sinha 2001) have complicated structures despite its high actuation efficiency and ability to actuate and sense with the same hardware. These drawbacks have limited the use of these actuators.

On the other hand, synthetic jet (ZNMF) actuators have been the focus of significant research activities for the past decade due to their utility in flow control applications (Glezer and Amitay 2002). They utilize the working fluid and do not need external fluid injection. They can force the momentum transfer across the flow without net mass flux (thus the name "synthetic"). The design of synthetic jets is also flexible and the working frequency range can be tuned according to different flow control applications. In addition, the recent paper by Gallas et al. (2003) presents a lumped element model of a piezoelectric-driven synthetic jet actuator. They provide a novel method to design and model synthetic jets, which makes them very suitable for closed-loop separation control. In lumped element modeling (LEM), the individual components of a synthetic jet are modeled as elements of an equivalent electrical circuit using conjugate power variables (i.e., power = generalized flow x generalized effort). The frequency response function of the circuit is derived to obtain an expression for Q_{out}/V_{AC}, the volume flow rate per applied voltage. The comparison between the LEM and experimental frequency response is shown in Figure 1-6.

For a variety of reasons, closed-loop control in a real-time experiment has been traditionally difficult to achieve. In reduced-scale laboratory experiments, the characteristic frequencies of separated turbulent flows are proportionally higher than those on full-scale models, which requires high frequency sensing and actuating capabilities. Furthermore, real-time experiments require the digital control system to sample at a minimum of twice of the highest frequency of interest. The availability of hardware (including actuators, sensors and real-time control systems) therefore imposes significant limitations on the complexity of the closed-loop control system. Lower order system models are typically required to reduce the complexity of the system.

Many model-based approaches are being developed and have shown promising results. Proper Orthogonal Decomposition (POD) based low order models have been studied extensively (Holmes et al. 1998; Tadmor et al. 2007) owing to their relatively high resolution and low computational intensity. Other reduced-basis models have also been studied (Coller et al. 2000; Wang et al. 2003). These models require that multiple measurements are simultaneously available in the flow field. However, this is impractical in feedback separation control and surface measurements are required in most applications. Ausseur et al. (2007) implemented a POD/mLSM proportional feedback control using the velocity field and surface pressure data to delay flow separation.

Some non-model based control approaches have gained favor because they bypass the complication of modeling separated flow while focusing on the primary control objectives. For

example, Banaszuk et al. (2003) and Becker et al. (2006) used an extremum-seeking closed-loop control algorithm to optimize the pressure recovery and lift, respectively. The present author in Tian et al. (2006) used a multi-dimensional optimization algorithm to optimize lift-to-drag ratio over an airfoil. These approaches are capable of "training" the excitation signals to be most effective in terms of the objective functions (i.e., pressure recovery, lift-to-drag ratio, etc.). The main drawback of the above approaches is that they operate on a time scale that is much larger than that of the flow dynamics. In other words, they work on time-averaged objective functions by explicitly taking advantage of the nonlinear nature of the fluid dynamics. This approach has the drawback of having to deal or cope with the nonlinear dynamics with no guarantee of success. This kind of approach is an example of the quasi-static control scheme shown in Figure 1-4.

On the other hand, the dynamic feedback control is used to model and control separated flow structures based on surface pressure data alone. The well-developed adaptive system identification (ID) algorithms in the controls community are utilized to model the flow system dynamics between the actuators and unsteady surface pressure sensors. The system ID algorithms generate known actuation signals and relate these signals with the surface pressure response measured by sensors. Linear dynamical equations are then used to model the relationship in a gradient descent sense (Haykin 2002). The system therein includes the dynamics of the actuators, the flow structures excited by the actuation, and the dynamics of the sensors. The system information is then used to predict the subsequent evolution of the pressure fluctuations. Control is applied using a spanwise zero-net-mass-flux (ZNMF) actuator slot by attempting to reduce the power of the surface pressure fluctuations in a closed-loop fashion, thus suppressing the unsteady flow fluctuations based on predicted flow characteristics. A similar idea has been applied to control of flow-induced cavity oscillations (Cattafesta et al. 1999) and turbulent boundary layer control (Rathnasingham and Breuer 2003). This kind of approach can be categorized as a dynamic control scheme shown in Figure 1-4.

1.3.4 Closed-Loop Control Algorithms

According to the classification in Figure 1-4, the control algorithms can be divided into two categories: quasi-static and dynamic. Optimization algorithms are used in this research as quasi-static algorithms. They are used to optimize target functions (such as lift, pressure recovery, etc.) in a recursive but static or time-averaged fashion. On the other hand, recursive system identification and disturbance rejection algorithms are widely used in active noise control area as dynamic algorithms. No one has attempted to apply these algorithms to the closed-loop separation control problem. This section gives a brief review of the two types of the algorithms. Details will be given in chapter 2.

1.3.4.1 Optimization algorithms

Optimization algorithms are widely used by decision-makers (e.g. economists, governments). They often need to choose an action to optimize target or cost functions, such as income, profit, etc. In a typically optimization problem, one is given a single function f that depends on one or more independent variables. The goal is to find the value of those variables where f is a maximum or a minimum value. In this research, various optimization algorithms are used to maximize/minimize different cost functions, such as lift, drag and pressure recovery. When using the optimization algorithms, some constraints are typically included in the algorithms. For example, one often seeks to limit the energy expenditure while optimizing the cost function. One should also notice that, unlike the applications used by the decision-makers, the cost functions used in this research are measured by sensors instead of analytical functions.

Some established minimization and maximization algorithms are summarized by Press et al. (1992). Most optimization algorithms can be easily implemented in a multi-dimensional space. The downhill simplex algorithm and the Powell's algorithm do not require derivative calculations. Between these two algorithms, the downhill simplex algorithm is more concise and self-contained. Both of them require storage of order N^2, where N is the number of dimensions or independent variables. Two other algorithms, the conjugate gradient and quasi-Newton methods, do require the calculation of derivatives. The conjugate gradient method requires only order N storage, while the quasi-Newton method requires storage of order N^2. On the other hand, none of the algorithms mentioned above are guaranteed to find a global extremum. They can lead to local extrema. Finding a global extremum is actually a very difficult problem. Two standard methods are typically used to improve the probability of finding a global extremum: 1) search for local extrema from various initial conditions and pick the most extreme of these; 2) perturb a local extremum to see if the algorithm goes back to the same value or finds a better result.

There are several global search algorithms that are currently active in research(e.g. Genetic Algorithms (GA) (Holland 1975), Particle Swarm Optimization (PSO) (Kennedy 1997) and Simulated Annealing Method (Haftka and Gürdal 1992)). The genetic algorithms and the particle swarm optimization are both derived from biology. They are population-based algorithms, namely they generate a population of points at each iteration and the population approaches an optimal solution. The GA and PSO take advantage of the large search population to increase probability of approaching a global optimum. The simulated annealing method is an analogy with thermodynamics, especially with the way metals cool and anneal, in which process nature finds the minimum energy state. The essence of the algorithm is to allow increase of cost function with some probability to improve the changes to find a global minimum.

Another optimization algorithm that has been applied to flow control problems is called the extremum-seeking algorithm. As a self-optimizing control algorithm, the extremum-seeking control was first introduced in the 1950s. After Krstic and Wang (1999) provided the stability studies, there has been a resurgence of interest of this control algorithm. Banaszuk et al. (2003) attempted to use this algorithm in the diffuser separation control problem. They were successful in maximizing the pressure recovery in the diffuser. They also used this algorithm to control combustion instability (Banaszuk et al. 2000).

1.3.4.2 System identification and disturbance rejection algorithms

System identification and disturbance rejection technologies are well developed and various algorithms are available in the active noise control area. Cattafesta et al. (1999) have applied these algorithms to other flow control problems, such as cavity resonance control. No one has attempted to apply this kind of approach to the separation control problem. In this research, this approach is investigated. Some system identification and disturbance rejection algorithms are reviewed in this section.

System identification algorithms. In general, system identification (ID) uses measured signals (i.e., inputs and outputs of the system) to identify (or estimate) the unknown system dynamics. It provides necessary system information for control algorithms. System identification algorithms can be divided into two categories: offline (or batch) and online (or recursive). Offline algorithms first acquire data and then try to estimate a low-order dynamical system model using these data offline. Online algorithms identify systems recursively while acquiring data in real-time. Online system identification is also known as adaptive filtering.

16

Least square (LS) identification algorithm is a generally used offline algorithm. Akers and Bernstein (1997 A) applied this approach to the ARMARKOV/LS identification algorithm with an ARMARKOV representation (see Chapter 2 for a detailed description of the algorithm). The ARMARKOV/LS identification algorithm uses vectors comprised of input-output data with a least-squares criterion to estimate a weight matrix containing a specified number of Markov (i.e., pulse response) parameters of the system. Then the eigensystem realization algorithm (ERA) (Juang 1994) is used to construct a minimal state space realization of the system. This is referred to as the ARMARKOV/LS/ERA identification algorithm.

The ARMARKOV/LS/ERA identification algorithm has two clear advantages compared to the ARMA/LS identification algorithm (Akers and Bernstein 1997 A). First, eigenvalues of the ARMARKOV representation are less sensitive to noise compared with eigenvalues of the ARMA representation. Second, the singular value decomposition of a block Hankel matrix constructed from the estimated Markov parameters provides an efficient model order indicator (Juang 1994, pp. 139).

As far as online algorithms are concerned, the least-mean-square (LMS) algorithm is the most commonly used algorithm. A more computationally intensive algorithm called the recursive-least-square (RLS) algorithm has faster convergence and smaller steady-state error than the LMS algorithm (Haykin 2002) but is more computationally intensive. Two different types of structure that can be applied to each of the algorithms are the finite-impulse-response (FIR) and the infinite-impulse-response (IIR) filters. The FIR filter is widely used due to its simple architecture and inherent stability as an all-zero model. However, its simple structure introduces difficulties for a system with low damping. The IIR filter can solve this problem with significantly lower-order and, therefore, lead to reduced computational expense. Unfortunately, the disadvantages of an IIR filter include more complicated adaptive algorithms compared with an FIR filter and the possible stability problems introduced by the pole(s) in the model (Haykin 2002; Shynk 1989; Netto and Diniz 1995).

Applying the LMS algorithm to the ARMARKOV representation, Akers and Bernstein (1997 B) introduced the recursive ARMARKOV/Toeplitz algorithm that is based upon recursive identification of the Markov parameters of a system. It estimates the Markov parameters recursively using time-domain, input-output data and then constructs the estimated model with the Markov parameters.

Disturbance rejection algorithms. As mentioned earlier, one of the possible control schemes for closed-loop separation control is to reduce velocity and pressure fluctuations in the separated region. This control scheme is generally called disturbance rejection.

Disturbance rejection controllers have been widely used in active noise control applications (Kuo and Morgan 1996). Recently, researchers have started to apply adaptive controllers to flow control problems. For example, Cattafesta et al. (1999) used an adaptive system to suppress the disturbance induced by the flow over a weapons-bay cavity. The advantages of using adaptive controllers are that they can adapt themselves according to different flow conditions and that they can potentially reduce the energy cost associated with the flow control problems. Cattafesta et al. (1997) showed that the control of cavity flow with closed-loop control requires one order-of-magnitude less power than that with open loop control.

Commonly used disturbance rejection algorithms include Filtered-X LMS (FXLMS), Filtered-U LMS (FULMS), Filtered-X RLS (FXRLS) and Filtered-U RLS (FXRLS) algorithms (Kuo and Morgan 1996). Besides these, the ARMARKOV adaptive control algorithm was first introduced by Venugopal and Berstein (1997) and further developed by Sane et al. (2001). The

17

underling model structure of the ARMARKOV adaptive control algorithm is the ARMARKOV representation, which is an extension of the ARMA representation with explicit impulse response (Markov) parameters. The ARMARKOV adaptive control algorithm doesn't require a model of the control-to-reference transfer function nor does it require a model of the transfer function from plant disturbances to sensors (Sane et al. 2001). The only transfer function needed is the control to performance transfer function, which can be identified simultaneously using the recursive ARMARKOV/Toeplitz system identification algorithm described in the previous section.

1.4 Objectives

- To explore suitable linear and nonlinear control objectives and strategies for closed-loop control of separated flows.
- To implement optimization algorithms and system identification/disturbance rejection algorithms for closed-loop control of separated flow on a wind tunnel airfoil model (NACA 0025).
- To analyze performance, adaptability, costs, and limitations of closed-loop separation control algorithms.
- To investigate the relevant flow physics of successful feedback control strategies.

1.5 Approach

The proposed closed-loop separation control includes two key parts: modeling and control strategies. As far as modeling is concerned, two types of approaches can be implemented to model the flow characteristics: 1) a reduced-order flow model based on the Navier-Stokes equations, 2) system identification techniques. The first approach is widely used in computational flow control simulations. This research will concentrate on experimental studies by using system identification techniques that have not yet been applied to the separation control problem. The dynamical systems model will include the dynamics of actuators, sensors, and the flow system. Then the disturbance rejection algorithm is used to suppress flow fluctuations (e.g., measured by unsteady pressure transducers).

One the other hand, for the non-model based optimization algorithms, no system identification is needed. The possible cost functions for the algorithm are summarized as follows. Since the suction pressure region of the upper surface of the airfoil is primarily responsible for lift generation and drag reduction, the static pressure recovery coefficient $dC_p/d(x/c)$ over the upper surface of the airfoil is a reasonable candidate as a cost function to maximize for feedback separation control. Other candidates for cost functions are lift and drag or combinations of these (e.g., lift/drag ratio). The benefit of using lift/drag is that L/D is a global or integrated quantity and is less sensitive to sensor location. The objectives for the controller are clear, i.e. to minimize drag and to maximize lift or the ratio of lift/drag. The experimental setup uses a lift/drag balance for this purpose.

1.6 Outline of This Dissertation

A theoretical background on system identification, control, and optimization algorithms will be discussed in Chapter 2. Simulation results and validation experiments of the algorithms will then be presented in Chapter 3. Chapter 4 describes the experimental setup and techniques for this research. Chapter 5 presents experimental results and discussion. Summary and future work will be presented in the last chapter.
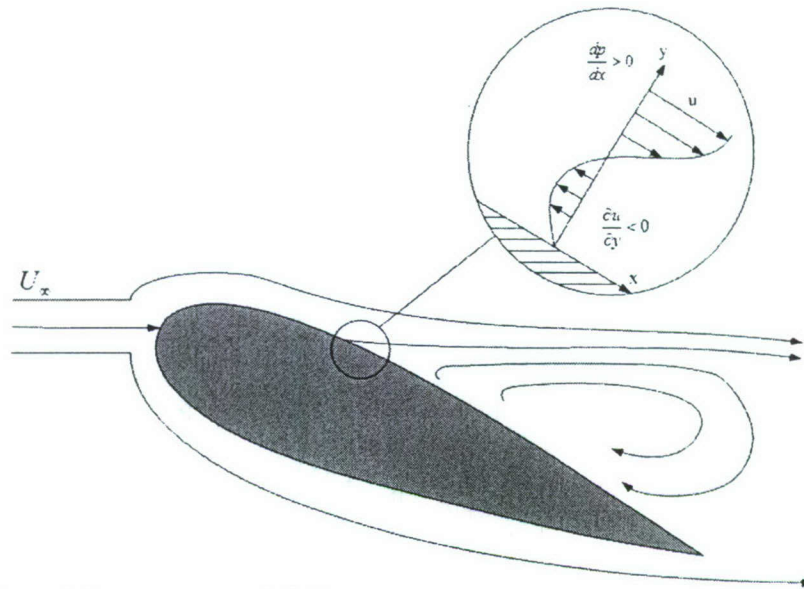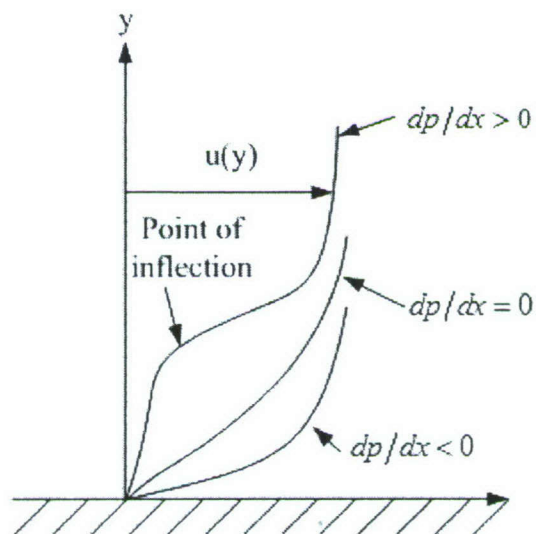
Figure 1-1. Separation of flow over an airfoil.

Figure 1-2. Types of velocity profiles as a function of pressure gradient (White 1991).

Error! Objects cannot be created from editing field codes.
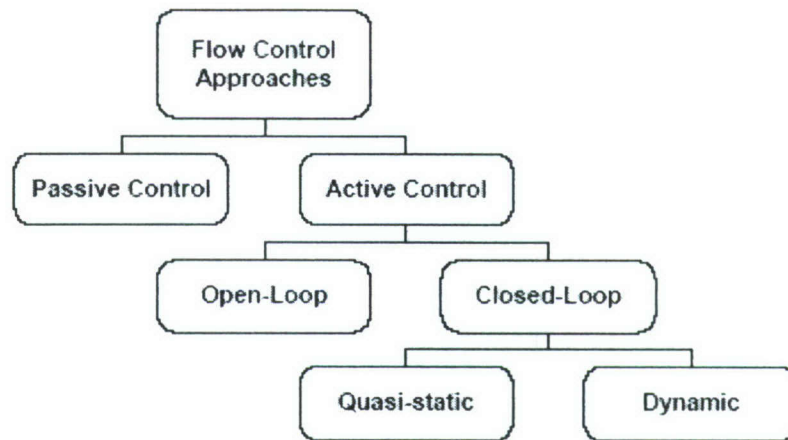Figure 1-3. Lift and drag coefficients of NACA 0025 airfoil at $\text{Re} \approx 100{,}000$.

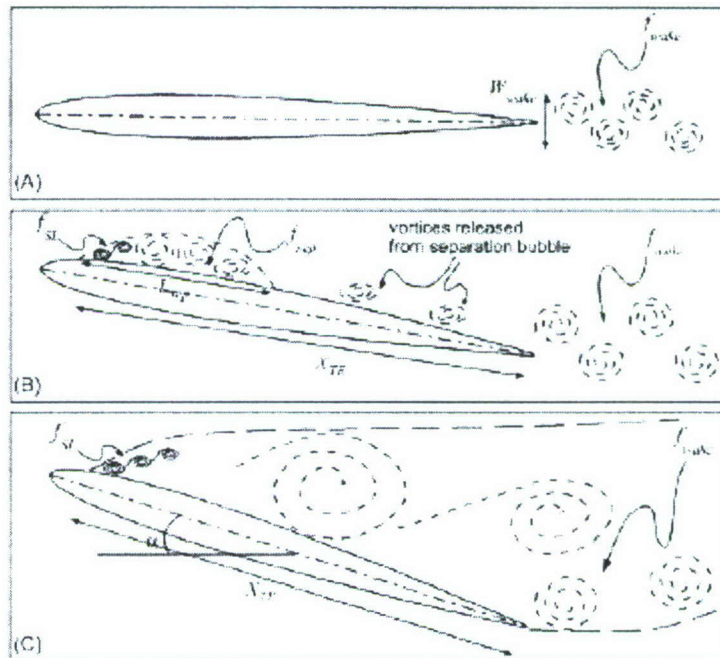Figure 1-4. Classification of flow control. (Cattafesta et al. 2003)

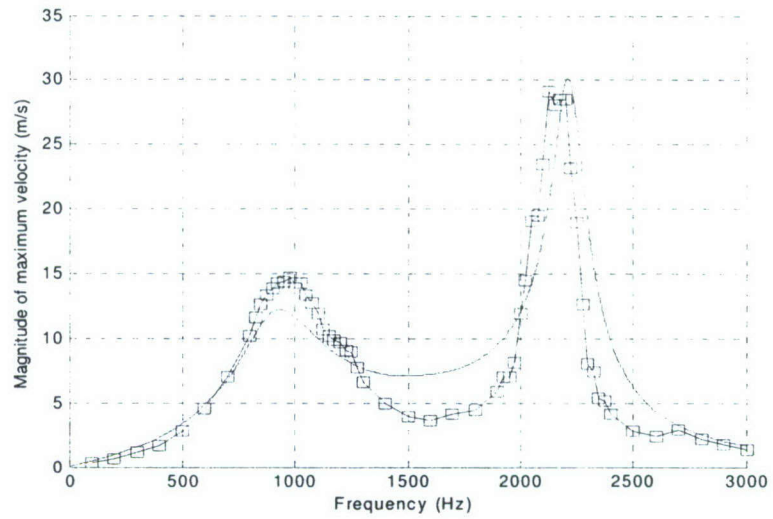Figure 1-5. Characterization of possible frequency scales in separated flow (Mittal et al. 2005).

Figure 1-6. Comparison between the lumped element model (-) and experimental frequency response (□) measured using phase-locked LDV for a prototypical synthetic jet (Gallas et al. 2003).

2   Theoretical Background

This chapter presents detailed descriptions and derivations of the algorithms that are used in this research. The algorithms include optimization, system identification, and disturbance rejection algorithms.

2.1   Optimization Algorithms

Some established minimization and maximization algorithms are summarized by Press et al. (1992). The downhill simplex algorithm and the Powell's algorithm do not require derivative calculations, which makes them good candidates for this research since derivative calculations are problematic for (usually noisy) experimental data. Between these two algorithms, the downhill simplex algorithm is more concise and self-contained. The so-called extremum-seeking algorithm has been applied to a flow control problem by Banaszuk et al. (2003). Thus, this algorithm is also summarized here.

2.1.1   Downhill Simplex Algorithm

The downhill simplex algorithm is implemented to minimize an objective function (e.g., drag-to-lift ratio). The benefits of the algorithm are its simplicity, applicability to multidimensional optimization and robust performance. The algorithm searches downhill in a straightforward fashion that makes no prior assumptions about the function. The downhill simplex algorithm requires only function evaluations, not derivatives. Since it does not make any assumptions about the function, it can be very slow sometimes. However, it can be very robust in the sense that it guarantees to find a minimum (at least a local minimum) (Press et al. 1992).

A simplex is the geometrical object consisting, in N dimensions, of $N+1$ points (or vertices) whereas the $N+1$ points span a N-dimensional vector space (Press et al. 1992). For example, in two dimensions, a simplex is a triangle. In three dimensions, it is a tetrahedron, although not necessarily a regular tetrahedron. The downhill simplex algorithm makes use of the geometrical concept of a simplex and works its way in the local downhill direction until it encounters a (at least, local) minimum.

The key steps of the downhill simplex algorithm are summarized as follows:

- Evaluate the cost function at chosen initial points. Note that there should be $N+1$ initial points, defining an initial simplex. For two or higher dimensions, the initial points should not be linearly dependent.
- Take a series of steps to move in the downhill direction. As an example, the steps for three-dimensional search are illustrated in Figure 2-1. In the figure, "Reflection" means that the algorithm reflects the highest (i.e. worst) point about the center of the three lower (i.e. better) points with some coefficients to the other side of the plane and then evaluates the cost function at the reflected point. "Expansion" means to expand further along the reflection direction when the "Reflection" point does improve (i.e., lower the cost function). "Contraction" means to move the highest (i.e. worst) point towards the plane formed by the three lower (i.e. better) points, thus contracting the original simplex. To summarize, all the necessary steps taken here are to move the worst point reference to the plane formed by the other better points to search for a better point.

- Stop when some termination criteria are met. For example, the moving distance is smaller than some tolerance value.

2.1.2 Extremum Seeking Algorithm

Artiyur and Krstic (2003) present the theoretic details and some applications of the extremum-seeking algorithm. Simulations using the algorithm can be done following the block diagram in Figure 2-2. The simple proof that this algorithm will drive $f(\theta)$ to its extremum is summarized below.

First, assume that $f(\theta)$ has a minimum f^* and can be approximated as the following form:

$$f(\theta)=f^*+\frac{f^{''}}{2!}\left(\theta-\theta^*\right)^2 \tag{4}$$

where θ^* is the optimal input and $f^{''}$ is the local curvature of the cost function $f(\theta)$ near θ^*. Since it is assumed that $f(\theta)$ has a minimum, $f^{''}$ should be larger than zero for this case.

Next, define the estimated error:

$$\tilde{\theta}=\theta^*-\hat{\theta} \tag{5}$$

where $\hat{\theta}$ is the estimated optimal input.

From Figure 2-2,

$$\theta=\hat{\theta}+a\sin(wt)=\theta^*-\tilde{\theta}+a\sin(wt) \tag{6}$$

Substituting equation (6) into equation (4) results in

$$y=f(\theta)=f^*+\frac{f^{''}}{2}\left[a\sin(wt)-\tilde{\theta}\right]^2 \tag{7}$$

Expand equation (7) and apply $\sin^2(wt)=\dfrac{1-\cos(2wt)}{2}$ to obtain

$$\begin{aligned}y&=f^*+\frac{f^{''}a^2}{2}\sin^2(wt)-f^{''}a\tilde{\theta}\sin(wt)+\frac{f^{''}\tilde{\theta}^2}{2}\\&=f^*+\frac{f^{''}a^2}{4}-\frac{f^{''}a^2}{4}\cos(2wt)-f^{''}a\tilde{\theta}\sin(wt)+\frac{f^{''}\tilde{\theta}^2}{2}\end{aligned} \tag{8}$$

From Figure 2-2, this signal y will pass through a high pass filter $\dfrac{s}{s+w_h}$. Let $0<w_h<w$, then all the DC components in equation (8) will be removed while the oscillatory terms remain.

$$\eta\approx-\frac{f^{''}a^2}{4}\cos(2wt)-f^{''}a\tilde{\theta}\sin(wt) \tag{9}$$

Next, η is multiplied by $a\sin(wt)$ to give

$$\varepsilon=-\frac{f^{''}a^2}{4}\cos(2wt)\sin(wt)-f^{''}a\tilde{\theta}\sin(wt)^2 \tag{10}$$

Using the trigonometric identities $\sin^2(wt)=\dfrac{1-\cos(2wt)}{2}$ and $\cos(2wt)\sin(wt)=\dfrac{\sin(3wt)-\sin(wt)}{2}$ results in

$$\varepsilon = -\frac{f''a^2}{4}\frac{\sin(3wt)-\sin(wt)}{2} - f''a\tilde{\theta}\frac{1-\cos(2wt)}{2}$$

$$= -\frac{f''a\tilde{\theta}}{2} + \frac{f''a^2}{8}\sin(wt) - \frac{f''a^2}{8}\sin(3wt) + \frac{f''a\tilde{\theta}}{2}\cos(2wt) \qquad (11)$$

From Figure 2-2, this signal ε passes through a low pass filter. Let $0<w_1<w$, then all the high frequency terms will be removed and only the DC term remains.

$$\varepsilon \gg -\frac{f''a\tilde{\theta}}{2} \qquad (12)$$

This signal then passes through an integrator

$$\hat{\theta} = \frac{f''a\tilde{\theta}}{2}\frac{k}{s} \qquad (13)$$

This gives

$$\hat{\theta}s = \dot{\hat{\theta}} = \frac{f''ak}{2}\tilde{\theta} \qquad (14)$$

From equation (5), assuming f^* is fixed, then

$$\dot{\tilde{\theta}} = -\dot{\hat{\theta}} \qquad (15)$$

From equations (14) and (15), one can obtain the first-order differential equation

$$\dot{\tilde{\theta}} = -\frac{f''ak}{2}\tilde{\theta} \qquad (16)$$

with the solution

$$\tilde{\theta} = \tilde{\theta}_0 e^{-\frac{f''ak}{2}t} \qquad (17)$$

Since f'' is assumed to be positive and a and k are positive constants, the estimated error $\tilde{\theta}$ will exponentially decay to zero.

2.2 System Identification Algorithms

System identification (ID) uses measured signals (i.e., inputs and outputs of the system) to identify (or estimate) the unknown parameters of an assumed dynamical systems model. It thus provides the necessary system information for control algorithms. System identification algorithms can be divided into two categories: offline (or batch) and online (or recursive). Offline algorithms first digitize a data record and then try to estimate the system using these data offline, usually via a least squares method. Conversely, online algorithms identify systems recursively while acquiring data in real-time. Online system identification is also known as adaptive filtering.

In this research, three system ID algorithms will be investigated: ARMARKOV/LS, ARMARKOV/LS/ERA and recursive ARMARKOV/Toeplitz algorithms. They are all based on the ARMARKOV representation, which explicitly contains Markov parameters (i.e., pulse response) of the system. The well known ARMA representation contains only one Markov parameter and is a special case of the ARMARKOV representation. The main advantage of these algorithms is their robustness with respect to low signal-to-noise ratios (Akers and Bernstein 1997 A, B). The ARMARKOV/LS algorithm is an offline algorithm and implements

24

an overparameterized realization of the system. The ARMARKOV/LS/ERA algorithm uses the same procedures to identify the system parameters as the ARMARKOV/LS algorithm, but implements a minimal realization of the system. The recursive ARMARKOV/Toeplitz algorithm is an online algorithm. The advantage of using an online algorithm is that it can adapt to the changing system.

2.2.1 ARMARKOV/LS Algorithm

Consider the discrete-time finite-dimensional linear time-invariant system:

$$x(k+1)=Ax(k)+Bu(k)$$
$$y(k)=Cx(k)+Du(k)$$

(18)

where $A \in R^{n \times n}, B \in R^{n \times i}, C \in R^{l \times n}, D \in R^{l \times i}$, and i and l are the number of inputs and outputs, respectively, of the system. For a single-input/single-output (SISO) system, $i=l=1$. The algorithm is derived below for a SISO system.

The Markov parameters H_j are defined by

$$H_j \triangleq D \qquad j=-1$$
$$H_j \triangleq CA^jB \qquad j \geq 0$$

(19)

Next, define the ARMARKOV regressor vector $\Phi_\mu(k) \in R^{2n+\mu}$:

$$\Phi_\mu(k) \triangleq \begin{bmatrix} y(k-\mu) \\ \vdots \\ y(k-\mu-n+1) \\ u(k) \\ \vdots \\ u(k-\mu-n+1) \end{bmatrix}$$

(20)

where n is the order of the system and μ is the number of Markov parameters. Here, y and u denote measured input and output of the system described in equation (18), respectively.

Next define the estimated output of the system

$$\hat{y}(k)=\hat{W}\Phi_\mu$$

(21)

where the ARMARKOV weight matrix $\hat{W}$ is defined by

$$\hat{W} \triangleq [-A_\mu \ H_{-1} \ L \ H_{\mu-2} \ B_\mu]$$

(22)

and

$$A_\mu \triangleq [\alpha_{\mu,1} \cdots \alpha_{\mu,n}] \in R^{1 \times n}$$
$$B_\mu \triangleq [\beta_{\mu,1} \cdots \beta_{\mu,n}] \in R^{1 \times n}$$

(23)

The expression of the weight matrix $\hat{W}_\mu$ is then determined to minimize the output error cost function defined below.

First, define the output error

$$\varepsilon(k) \equiv y(k)-\hat{y}(k)$$

(24)

and the output mean squared error cost function

25

$$J \equiv \frac{1}{N}\sum_{k=1}^{N}\frac{1}{2}\varepsilon^2(k)=\frac{1}{N}\sum_{k=1}^{N}\frac{1}{2}\varepsilon^T(k)\varepsilon(k) \tag{25}$$

where N is the number of measurements.

Substituting equations (20), (21), (22) and (24) into equation (25) results in

$$\Rightarrow J=\frac{1}{N}\sum_{k=1}^{N}\frac{1}{2}\left(y(k)-\hat{W}\Phi(k)\right)^T\left(y(k)-\hat{W}\Phi(k)\right) \tag{26}$$

$$\Rightarrow J=\frac{1}{N}\sum_{k=1}^{N}\frac{1}{2}\left(y^T(k)-\Phi^T(k)\hat{W}^T\right)\left(y(k)-\hat{W}\Phi(k)\right) \tag{27}$$

$$\Rightarrow J=\frac{1}{N}\sum_{k=1}^{N}\frac{1}{2}(y^T(k)y(k)-\Phi^T(k)\hat{W}^Ty(k)$$
$$-y^T(k)\hat{W}\Phi(k)+\Phi^T(k)W^T\hat{W}(k)\Phi(k)) \tag{28}$$

Because $\Phi^T(k)\hat{W}^Ty(k)$ and $y^T(k)\hat{W}\Phi(k)$ are transposes of each other and are also scalars, they are equal to each other. So,

$$J=\frac{1}{N}\sum_{k=1}^{N}\frac{1}{2}\left(y^T(k)y(k)-2\Phi^T(k)\hat{W}^Ty(k)+\Phi^T(k)W^T\hat{W}(k)\Phi\right) \tag{29}$$

To find the $\hat{W}$ to minimize the output error cost function defined in equation (25), we set the partial derivative of J with respect to $\hat{W}$ equal to zero. So,

$$\frac{\partial J}{\partial \hat{W}}=\frac{\partial^T J}{\partial \hat{W}^T}=0 \tag{30}$$

From matrix calculus, we derive each term of J in equation (29) first,

$$\frac{\partial}{\partial \hat{W}^T}\left(y^T(k)y(k)\right)=0 \tag{31}$$

$$\frac{\partial^T}{\partial \hat{W}^T}\left(2\Phi^T(k)\hat{W}^Ty(k)\right)=2\left(\left(\Phi^T(k)y(k)\right)^T\right)^T=2\Phi^T(k)y(k) \tag{32}$$

$$\frac{\partial^T}{\partial \hat{W}^T}\left(\Phi^T(k)\hat{W}^T\hat{W}\Phi(k)\right)=\left[\frac{\partial\left(\Phi^T(k)\hat{W}^T\hat{W}\Phi(k)\right)}{\partial(\hat{W}^T\hat{W})}\frac{d(\hat{W}^T\hat{W})}{d\hat{W}^T}\right]^T$$
$$=\left[\Phi^T(k)\Phi(k)\left(2\hat{W}^T\right)\right]^T \tag{33}$$
$$=2\hat{W}\Phi^T(k)\Phi(k)$$

Thus,

$$\frac{\partial^T J}{\partial \hat{W}^T}=0=\frac{1}{N}\sum_{k=1}^{N}\frac{1}{2}\left[-2\Phi^T(k)y(k)+2\hat{W}\Phi^T(k)\Phi(k)\right] \tag{34}$$

$$\Rightarrow \frac{1}{N}\sum_{k=1}^{N}\hat{W}\Phi^T(k)\Phi(k)=\frac{1}{N}\sum_{k=1}^{N}\Phi^T(k)y(k) \tag{35}$$

26

Finally, the expression of the weight matrix $\hat{W}$ to minimize the output error cost function is given by

$$\hat{W}=\left[\frac{1}{N}\sum_{k=1}^{N}\Phi^{T}(k)y(k)\right]\left[\frac{1}{N}\sum_{k=1}^{N}\Phi^{T}(k)\Phi(k)\right]^{-1} \tag{36}$$

After extracting the coefficients A_{μ}, B_{μ} and H_{j} from $\hat{W}$ via equation (22), we can obtain the system transfer function of the ARMARKOV representation, which is defined as follows

$$G_{1}(z)=\frac{H_{-1}z^{\mu+n-1}+L+H_{\mu-2}z^{n}+\beta_{\mu,1}z^{n-1}+L+\beta_{\mu,n}}{z^{\mu+n-1}+\alpha_{\mu,1}z^{n-1}+L+\alpha_{\mu,n}} \tag{37}$$

This is called the ARMARKOV/LS identification algorithm and this algorithm assumes the numerator has the same order of the denominator for simplicity. For the systems whose numerators and denominators do not have the same order, some parameters described in equation (37) will be identified to be approximately zero.

The well-known ARMA representation only has one explicit Markov parameter and it is a special form of the ARMARKOV representation with $\mu=1$ in (37)

$$G_{2}(z)=\frac{H_{-1}z^{n}+\beta_{1,1}z^{n-1}+L+\beta_{1,n}}{z^{n}+\alpha_{1,1}z^{n-1}+L+\alpha_{1,n}} \tag{38}$$

For system identification problems, the order of the system is usually not known in advance, so we adjust n and μ to improve the performance of the system identification algorithm.

2.2.2 ARMARKOV/LS/ERA Algorithm

The ARMARKOV/LS/ERA algorithm obtains a minimal realization of the transfer function of the system from the Markov parameters. It uses the same algorithm as the ARMARKOV/LS algorithm to obtain the weight matrix $\hat{W}$ by equation (36). Then the Markov parameters H_{j} can be extracted from equation (36) by using equation (22). Next, define the Markov block Hankel matrix for a SISO system:

$$H_{r,s,j}\triangleq\begin{pmatrix} H_{j} & \cdots & H_{j+s} \\ \vdots & \ddots & \vdots \\ H_{j+r} & \cdots & H_{j+r+s} \end{pmatrix} \tag{39}$$

where r,s are any positive integers. In this research, r is set to be equal to s for convenience.

Then, we apply the singular value decomposition as describe in Akers and Bernstein (1997A)

$$H_{r,s,0}=PS_{r,s}Q^{T} \tag{40}$$

where $P^{T}P=Q^{T}Q=I$ and $S_{r,s}=$ diagonal matrix of singular values.

From the Eigenvalue Realization Algorithm (ERA), (Juang 1994, pp. 133-137)

27

$$A = S_{r,s}^{-1/2} P^T H_{r,s,1} Q S_{r,s}^{-1/2}$$
$$B = S_{r,s}^{1/2} Q^T E_s$$
$$C = E_r^T P S_{r,s}^{1/2}$$
$$D = H_{-1}$$

(41)

where $E_i = \begin{bmatrix} 1 \\ 0_{i \times 1} \end{bmatrix}$. The ERA also requires $r, s \geq n-1$.

This arrives at the minimal state space realization of the system

$$G_3(z) = C(zA - I)^{-1} B + D$$

(42)

This is called the ARMARKOV/LS/ERA algorithm. It is a minimal realization because the system order can be chosen as a minimal value when using the singular value decomposition in equation (40). However, an important drawback of this algorithm is that the singular value decomposition in equation (2.23) is very computational intensive.

Theoretically, the rank of the $S_{r,s}$ matrix should be the rank of the system. However, in practical applications, the singular value decomposition will return more singular values than the system order due to measurement noise, and so the extra singular values should be small. So, only the largest n singular values obtained by the singular value decomposition will be used.

2.2.3 Recursive ARMARKOV/Toeplitz Algorithm

First, define the ARMARKOV regressor vector $\Phi_\mu(k) \in R^{2n+2p-2+\mu}$:

$$\Phi_\mu(k) \triangleq \begin{bmatrix} y(k-\mu) \\ \vdots \\ y(k-\mu-p-n+2) \\ u(k) \\ \vdots \\ u(k-\mu-p-n+2) \end{bmatrix}$$

(43)

where n is the order of a system, μ is the number of Markov parameters, and a new parameter p determines the averaging window of input-output data that appears in the above regressor vector.

It follows that

$$\hat{y}(k) = \hat{W}\Phi_\mu$$

(44)

where the ARMARKOV/Toeplitz weight matrix $\hat{W} \in R^{p \times (2n+2p-2+\mu)}$ is the block-Toeplitz matrix defined by

$$\hat{W}_\mu \triangleq \begin{bmatrix} -A_\mu & 0 & \cdots & 0 & H_{-1} & \cdots & H_{\mu-2} & B_\mu & 0 & \cdots & 0 \\ 0 & \ddots & \ddots & \vdots & 0 & \ddots & \ddots & \ddots & \ddots & & \vdots \\ \vdots & \ddots & \ddots & 0 & \vdots & \ddots & \ddots & \ddots & \ddots & \ddots & 0 \\ 0 & \cdots & 0 & -A_\mu & 0 & \cdots & 0 & H_{-1} & \cdots & H_{\mu-2} & B_\mu \end{bmatrix}$$

(45)

and $A_{\mu} \triangleq [\alpha_{\mu,1} \cdots \alpha_{\mu,n}] \hat{I} R^{1 \times n}$, $B_{\mu} \triangleq [\beta_{\mu,1} \cdots \beta_{\mu,n}] \in R^{1 \times n}$, and H_j are the Markov parameters.

As before, define the output error $\varepsilon(k)$ and the output error cost function $J(k)$

$$\varepsilon(k) \triangleq Y(k) - \hat{Y}(k) \tag{46}$$

$$J(k) \triangleq \frac{1}{2} \varepsilon^T(k) \varepsilon(k) \tag{47}$$

Next, the gradient of $J(k)$ with respect to $\hat{W}(k)$ can be calculated by

$$\frac{\partial J(k)}{\partial \hat{W}(k)} = -U \circ [\varepsilon(k) \Phi^T(k)] \tag{48}$$

where $\circ$ denotes the Hadamard product (i.e. element-wise matrix product) and $U \in R^{p \times (2n+2p-2+\mu)}$ is defined by

$$U \triangleq \begin{bmatrix} I_{1 \times n} & 0 & \cdots & 0 & I_{1 \times (\mu+n)} & 0 & \cdots & 0 \\ 0 & \ddots & \ddots & \vdots & 0 & \ddots & \ddots & \vdots \\ \vdots & \ddots & \ddots & 0 & \vdots & \ddots & \ddots & 0 \\ 0 & \cdots & 0 & I_{1 \times n} & 0 & \cdots & 0 & I_{1 \times (\mu+n)} \end{bmatrix} \tag{49}$$

Finally, the recursive update law for the weight matrix $\hat{W}$ is given by

$$\hat{W}(k+1) = \hat{W}(k) - \eta(k) \frac{\partial J(k)}{\partial \hat{W}(k)} \tag{50}$$

In equation (50), $\eta(k)$ is the *adaptive step size*. The optimal adaptive step size $\eta_{opt}(k)$ is defined as

$$\eta_{opt}(k) \triangleq \frac{\|\varepsilon(k)\|_2^2}{\left\| \dfrac{\partial J(k)}{\partial \hat{W}(k)} \right\|_2^2} \tag{51}$$

where $\|\cdot\|_2$ denotes the spectral norm.

The computationally efficient step size $\eta_{eff}(k)$ (namely, it is more computational efficient since it only needs to calculate the normal ARMARKOV regressor vector $\Phi_{\mu}(k)$) is defined as

$$\eta_{eff}(k) \triangleq \frac{1}{\|\Phi_{\mu}(k)\|_2^2} \tag{52}$$

In order to assure convergence, $\eta(k)$ should satisfy $\eta(k) = \alpha \eta_{opt}(k)$ or $\eta(k) = \alpha \eta_{eff}(k)$, where $\alpha \in (0, 2)$.

After $\hat{W}$ matrix is obtained by (50), we can extract the coefficients A_{μ}, B_{μ} and H_j from (22). Then, we can obtain the system transfer function of the ARMARKOV representation form, which is defined in equation (37). Since the A_{μ}, B_{μ} and H_j coefficients are updated every iteration, this algorithm is called as the recursive ARMARKOV/Toeplitz algorithm.

2.3 Adaptive Disturbance Rejection Algorithms

Disturbance rejection controllers have been widely used in active noise control applications (Kuo and Morgan 1996). A block diagram of a standard disturbance rejection problems is shown in Figure 2-3, where w is the disturbance, u is the control signal, y is the reference signal, z is the performance signal and G_c is the disturbance rejection controller. The goal for the controller is to generate a control signal u to minimize some cost function of the performance signal. The four transfer matrices, namely, the primary path G_{zw}, the secondary path G_{zu}, the reference path G_{yw} and the feedback path G_{yu}, are standard terminology in the noise control literature (Kuo and Morgan 1996). The feedforward-type disturbance rejection algorithms, such as FXLMS and FXRLS, assume that $G_{yu}=0$ (no feedback path) and $G_{yw}=I$. On the other hand, the ARMARKOV disturbance rejection algorithm does not make these assumptions. All the disturbance rejection algorithms require identifying the secondary path G_{zu} by online or offline system identification methods.

2.3.1 ARMARKOV Disturbance Rejection Algorithm

Consider the linear discrete time two-input/two-output system (shown in Figure 2-3) given by

$$z(k)=G_{zw}w(k)+G_{zu}u(k) \tag{53}$$

$$y(k)=G_{yw}w(k)+G_{yu}u(k) \tag{54}$$

where the disturbance $w(k)$, the control $u(k)$, the reference $y(k)$ and the performance $z(k)$ are in R^{m_w}, R^{m_u}, R^{l_y} and R^{l_z} respectively, and m and l denote the number of inputs and outputs, respectively. The system transfer matrices G_{zw} (primary path), G_{zu} (secondary path), G_{yw} (reference path) and G_{yu} (control path) are in $R^{l_z \times m_w}$, $R^{l_z \times m_u}$, $R^{l_y \times m_w}$ and $R^{l_y \times m_u}$, respectively. The objective of the active noise or vibration control problems is to determine a controller $G_c \in R^{m_u \times l_y}$ that produces a control signal $u(k)=G_c y(k)$ such that the performance measure $z(k)$ is minimized (Sane et al. 2001). A measurement of $z(k)$ is used to adapt G_c.

The ARMARKOV form of (53) - (54) is

$$
z(k) = \sum_{j=1}^{n} -\alpha_j z(k-\mu-j-1)+\sum_{j=1}^{\mu} H_{zw,j-2}w(k-j+1)+\sum_{j=1}^{n} B_{zw,j}w(k-\mu-j-1)
$$
$$
+\sum_{j=1}^{\mu} H_{zu,j-2}u(k-j+1)+\sum_{j=1}^{n} B_{zu,j}u(k-\mu-j+1) \tag{55}
$$

$$
y(k)=\sum_{j=1}^{n} -\alpha_j y(k-\mu-j-1)+\sum_{j=1}^{\mu} H_{yw,j-2}w(k-j+1)+\sum_{j=1}^{n} B_{yw,j}w(k-\mu-j-1)
$$
$$
+\sum_{j=1}^{\mu} H_{yu,j-2}u(k-j+1)+\sum_{j=1}^{n} B_{yu,j}u(k-\mu-j+1) \tag{56}
$$

where $\alpha_j \in R$, $B_{zw,j}, H_{zw,j} \in R^{l_z \times m_w}$, $B_{zu,j}, H_{zu,j} \in R^{l_z \times m_u}$, $B_{yw,j}, H_{yw,j} \in R^{l_y \times m_w}$, $B_{yu,j}, H_{yu,j} \in R^{l_y \times m_u}$, n is the order of the system, and μ is the number of the Markov parameters.

Then, we define the extended performance vector $Z(k)$, the extended measurement vector $Y(k)$, and the extended control vector $U(k)$ as

$$Z(k) \triangleq \left[z(k) \; L \; z(k-p+1) \right]^T \tag{57}$$

$$Y(k) \triangleq \left[y(k) \; L \; y(k-p+1) \right]^T \tag{58}$$

$$U(k) \triangleq \left[u(k) \; L \; u(k-p_c+1) \right]^T \tag{59}$$

where p is an averaging or windowing parameter and $p_c = (\mu+n+p-1)$.

The ARMARKOV regressor vectors Φ_{zw} and Φ_{yw} are defined by

$$\Phi_{zw} \triangleq \left[z(k-\mu) \cdots z(k-\mu-p-n+2) \quad w(k) \cdots w(k-\mu-p-n+2) \right]^T \tag{60}$$

and

$$\Phi_{yw} \triangleq \left[y(k-\mu) \cdots y(k-\mu-p-n+2) \quad w(k) \cdots w(k-\mu-p-n+2) \right]^T \tag{61}$$

Then (55) and (56) can be written as

$$Z(k) = W_{zw} \Phi_{zw} + B_{zu} U(k) \tag{62}$$

$$Y(k) = W_{yw} \Phi_{yw} + B_{yu} U(k) \tag{63}$$

where W_{zw}, B_{zu}, W_{zw} and B_{yu} are the ARMARKOV weight matrices. Only B_{zu} will be used in the control algorithm (shown later), and it will be obtained using the ARMARKOV/Toeplitz system identification algorithm. The ARMARKOV control matrix B_{zu} is given by

$$B_{zu} \triangleq \begin{bmatrix} H_{zu,-1} \cdots H_{zu,\mu-2} & B_{zu,1} \cdots B_{zu,n} & 0_{l_z \times m_u} \cdots 0_{l_z \times m_u} \\ 0_{l_z \times m_u} & \ddots & \ddots & \ddots & \ddots & \vdots \\ \vdots & \ddots & \ddots & \ddots & \ddots & 0_{l_z \times m_u} \\ 0_{l_z \times m_u} & \cdots & H_{zu,-1} & H_{zu,\mu-2} & B_{zu,1} & \cdots & B_{zu,n} \end{bmatrix} \tag{64}$$

where $0_{l_z \times m_u}$ is the zero matrix.

Next, the ARMARKOV adaptive disturbance rejection algorithm is derived. The control signal $u(k)$ is given by

$$u(k) = \sum_{j=1}^{n_c} -\alpha_{c,j} u(k-\mu_c-j+1) + \sum_{j=1}^{\mu_c} H_{c,j-2} y(k-j+1) + \sum_{j=1}^{n_c} B_{c,j} y(k-\mu_c-j+1) \tag{65}$$

where $\alpha_{c,j} \in R$ and $H_{c,j}, B_{c,j} \in R^{m_u \times l_y}$.

Similarly, the delayed versions are

$$u(k-1) = \sum_{j=1}^{n_c} -\alpha_{c,j} u(k-\mu_c-j) + \sum_{j=1}^{\mu_c} H_{c,j-1} y(k-j) + \sum_{j=1}^{n_c} B_{c,j} y(k-\mu_c-j) \tag{66}$$

$$\vdots$$

$$u(k\text{-}p_c+1)=\sum_{j=1}^{n_c}\text{-}\alpha_{c,j}u(k\text{-}\mu_c\text{-}j\text{-}p_c+2)$$

$$+\sum_{j=1}^{\mu_c}H_{c,j\text{-}1}y(k\text{-}j\text{-}p_c+2)+\sum_{j=1}^{n_c}B_{c,j}y(k\text{-}\mu_c\text{-}j\text{-}P_c+2) \tag{67}$$

Substituting all these equations in (59) and reordering gives

$$U(k)=\sum_{i=1}^{P_c}L_i\theta(k\text{-}i+1)R_i\Phi_{uy}(k) \tag{68}$$

where

$$\theta(k)\triangleq\left[\text{-}\alpha_{c,1}(k)I_{m_u}\ \cdots\ \text{-}\alpha_{c,n_c}(k)I_{m_u}\quad H_{c,0}(k)\cdots H_{c,\mu_c\text{-}2}(k)\quad B_{c,1}(k)\cdots B_{c,n_c}(k)\right] \tag{69}$$

$$\Phi_{uy}(k)\triangleq\left[u(k\text{-}\mu_c)\cdots u(k\text{-}\mu_c\text{-}n_c\text{-}p_c+2)\quad y(k)\cdots y(k\text{-}\mu_c\text{-}n_c\text{-}p_c+1)\right]^T \tag{70}$$

$$L_i\triangleq\begin{bmatrix}0_{(i\text{-}1)m_u\times m_u}\\I_{m_u}\\0_{(p_c\text{-}i)m_u\times m_u}\end{bmatrix} \tag{71}$$

and

$$R_i\triangleq\begin{bmatrix}0_{q_1\times(i\text{-}1)m_u}&I_{q_1\times q_1}&0_{q_1\times(p_c\text{-}i)m_u}&0_{q_1\times(i\text{-}1)l_y}&0_{q_1\times q_2}&0_{q_1\times(p_c\text{-}i)l_y}\\0_{q_2\times(i\text{-}1)m_u}&0_{q_2\times q_1}&0_{q_2\times(p_c\text{-}i)m_u}&0_{q_2\times(i\text{-}1)l_y}&I_{q_2\times q_2}&0_{q_2\times(p_c\text{-}i)l_y}\end{bmatrix} \tag{72}$$

with $q_1\triangleq n_cm_u$ and $q_2\triangleq(n_c+\mu_c\text{-}1)l_y$.

Thus from (62) and (68), we obtain

$$Z(k)\triangleq W_{zw}\Phi_{zw}(k)+B_{zu}\sum_{i=1}^{P_c}L_i\theta(k\text{-}i+1)R_i\Phi_{uy}(k)=W_{zw}\Phi_{zw}(k)+B_{zu}U(k) \tag{73}$$

Next, evaluate the performance of the current value of $\theta(k)$ based upon the behavior of the system during the previous p steps to result in the definition of the estimated performance $\hat{Z}(k)$ by

$$\hat{Z}(k)\triangleq W_{zw}\Phi_{zw}(k)+B_{zu}\sum_{i=1}^{P_c}L_i\theta(k)R_i\Phi_{uy}(k) \tag{74}$$

Substituting (73) into (74), we obtain the estimated performance in terms of known and measured variables

$$\hat{Z}(k)\triangleq Z(k)\text{-}B_{zu}\left(U(k)\text{-}\sum_{i=1}^{P_c}L_i\theta(k)R_i\Phi_{uy}(k)\right) \tag{75}$$

Using (75), we define the estimated performance cost function

$$J(k)=\frac{1}{2}\hat{Z}^T(k)\hat{Z}(k) \tag{76}$$

The purpose for the ARMARKOV adaptive controller is to obtain the controller parameters $\theta(k)$ such that the performance cost function $J(k)$ is minimized. Using matrix derivative formulae, the gradient of $J(k)$ with respect to $\theta(k)$ is given by

$$\frac{\partial J(k)}{\partial \theta(k)} = \sum_{i=1}^{p_c} L_i^T B_{zu}^T \hat{Z}(k) \Phi_{uy}^T(k) R_i^T \tag{77}$$

The gradient is used in the update law

$$\theta(k+1) = \theta(k) - \eta(k) \frac{\partial J(k)}{\partial \theta(k)} \tag{78}$$

where $\eta(k)$ is the adaptive step size. An implementable adaptive step size $\eta_{imp}(k)$ is used

$$\eta_{imp}(k) \triangleq \frac{1}{p_c \left\| B_{zu} \right\|_F^2 \left\| \Phi_{uy}(k) \right\|_2^2} \tag{79}$$

where $\left\| \cdot \right\|_F$ and $\left\| \cdot \right\|_2$ denote the Frobenius norm and the spectral norm (Golub and Van Loan 1996), respectively.

The steps involved in implementing the ARMARKOV adaptive disturbance rejection algorithm are summarized as follows:

- Obtain the matrix B_{zu} (eqn. (64)) by using the recursive ARMARKOV/Toeplitz system identification algorithm (eqn. (45)) or the offline ARMARKOV/LS (eqn. (36)).

- Calculate the control signal $u(k)$ from the controller parameter matrix $\theta(k)$ and the vector $\Phi_{uy}(k)$ (eqn. (68)).

- Use the signals $u(k)$, $z(k)$ and $y(k)$ to update the vectors $\hat{Z}(k)$ (eqn.(75)) and $\Phi_{uy}(k)$ (eqn. (70)).

- Calculate the gradient $\frac{\partial J(k)}{\partial \theta(k)}$ (eqn. (77)).

- Calculate the implementable adaptive step size $\eta_{imp}(k)$ (eqn. (79)).

- Update the controller parameter matrix $\theta(k) \rightarrow \theta(k+1)$ (eqn (78)).
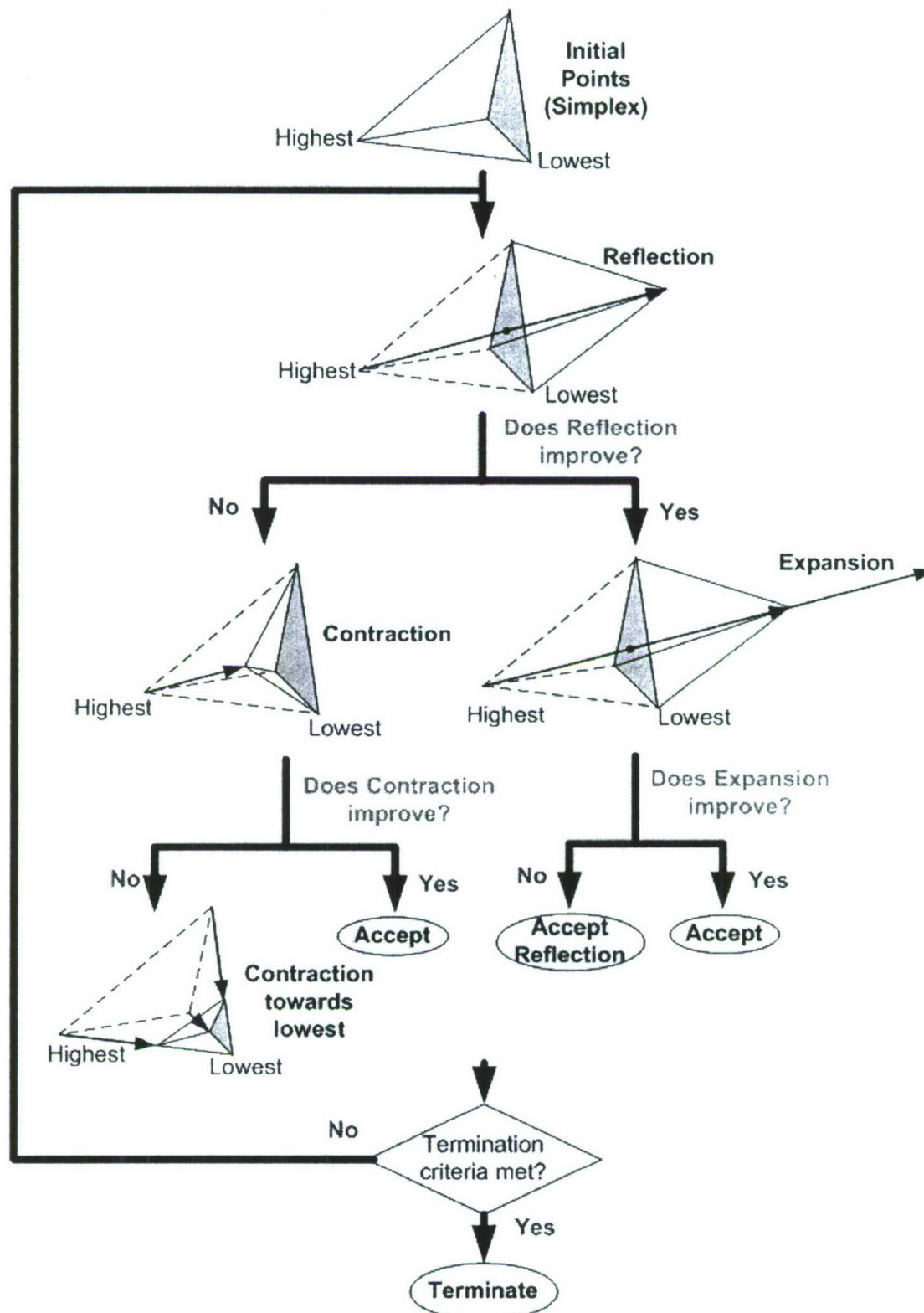
Figure 2-1. Flow chart of downhill simplex algorithm.
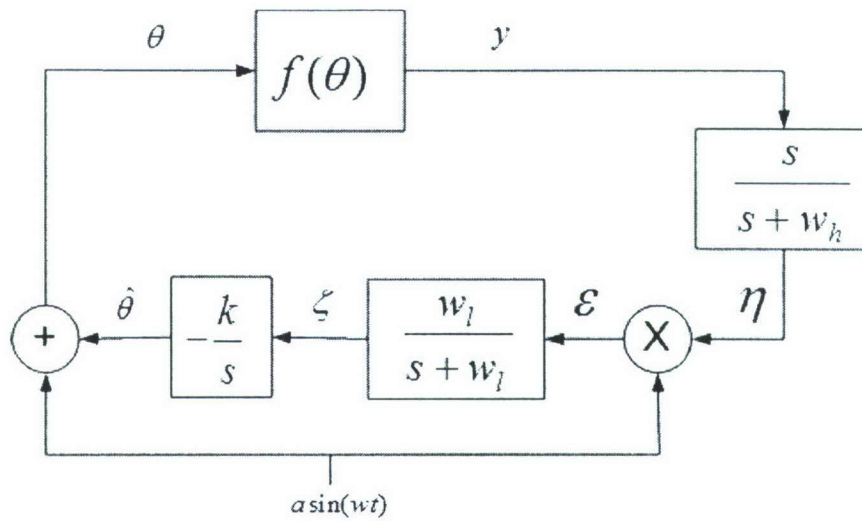
Figure 2-2. Block diagram for the extremum seeking control.
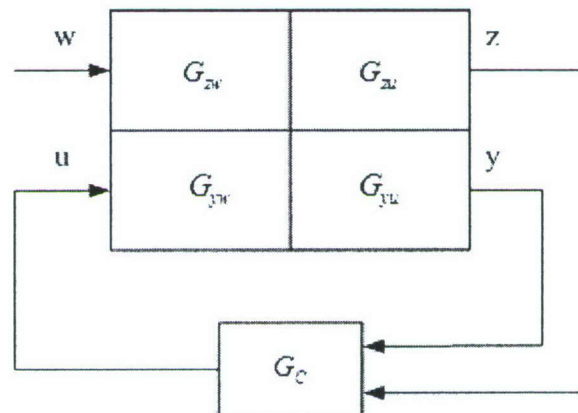
Figure 2-3. Block diagram of disturbance rejection control.

3   Simulation and Validation experiments

Before the algorithms are used for closed-loop separation control in the wind tunnel experiments, they are tested by using Matlab/Simulink simulations or validation experiments. The purpose of this chapter is to ensure that the algorithms work as desired.

3.1   Optimization Simulations

3.1.1   Downhill Simplex Simulation Results

The downhill simplex algorithm is programmed in Matlab. The performance of the algorithm is illustrated by a 1-dimensional and a 2-dimensional simulation cases. This algorithm can be easily extended to higher dimensions.

In the 1-dimensional case, the cost function $f(x)$ is chosen to be an 8th order polynomial function of x, which has a local minimum at $x=14.2$ and a global minimum at $x=67.3$ as shown in Figure 3-1. Two initial conditions are selected to demonstrate that this algorithm can be "trapped" by a local minimum. The first initial condition is at about $x=45$. One should notice that for this 1-dimensional problem, there should be two independent points (a simplex) as the initial condition. As shown in Figure 3-1, the downhill simplex algorithm crawls down to the global minimum (red trace). On the other hand, the second initial condition is at about $x=30$, which leads the algorithm to the local minimum (blue trace). This is dictated by the inherent "downhill" nature of the algorithm.

Another example is to demonstrate how the downhill simplex algorithm works in two-dimensional space. The cost function is obtained in Matlab by the "peaks" command. The formula for the cost function is as follows:

$$Z = 3\left[(1\text{-}x)^2 e^{-x^2} -(y+1)^2\right] - 10(\frac{x}{5} -x^3 -y^5)e^{-x^2 -y^2} - \frac{1}{3}e^{-(x+1)^2 -y^2} \tag{80}$$

This function has two local minima and a global minimum as shown in Figure 3-2. Similar as the 1-dimensoinal case, the optimization algorithm converges to either a local minimum (blue trace) or the global minimum (red trace) depending on the initial condition. Although each iteration of the algorithm requires several steps (Chapter 2), it only takes 9 iterations to find the global minimum. This result is encouraging and suggests that it can be fast for some cases. One can also adjust the termination tolerance to control the time consumption. On the other hand, the time consumption of the separation control experiments is also dependent on other factors, such as data acquisition. This will be discussed further in Chapter 5.

3.1.2   Extremum Seeking Simulation Results

The extremum seeking algorithm is implemented in Simulink. Figure 3-3 shows the simulation block diagram for the extremum seeking control. In the simulation, the algorithm seeks a maximum instead of a minimum. One can easily modify the program to search for a minimum by adding a negative sign to the cost function. Two numerical models are tested. The first model is a quadratic function $f=f^*-\left(\theta\text{-}\theta^*\right)^2$, which has a single maximum f^* at $\theta=\theta^*$ as shown in Figure 3-4. In this case, f^* is set to 10 and θ^* is set to 5. The second model is a double hump model, which is fitted by a 8th order polynomial function, which is the same as the model shown in Figure 3-1 with a opposite sign. It has a local maximum and a global maximum as shown in Figure 3-5.

The ARMARKOV disturbance rejection algorithm requires the following three parameters: the order of the controller n_c, the number of Markov parameters of the controller μ_c and the adaptive step size constant γ that controls the convergence rate of the controller.

The controller uses the system information identified by the ARMARKOV/Toeplitz system ID with the parameters of $p=n=2$, $\mu=10$ and SNR=20 dB (shown in Figure 3-21). All cases of the controller design use the same identified system.

Band-limited white noise with frequency of $0 - 150$ Hz and variance of 0.09 is used to excite the disturbance piezoceramics. Figure 3-26 and Figure 3-27 show the time data of the performance and control signals with the parameters of $n_c=2$, $\mu_c=20$ and $\Upsilon=1$. The system ID is off for the whole period and the controller is off initially and turned on at $t = 20$ sec. In Figure 3-28, the power spectra of the performance signal with control off and on are compared. The power spectra were calculated by using the time data of 20-second duration with NFFT=1024, 50% overlap and a hanning window. The "control on" case is taken after the controller is turned on for 30 seconds. The performance of suppression is calculated by $10g\log_{10}\left(\sigma_{off}^2/\sigma_{on}^2\right)$ and this case gives 11.7 dB suppression. Interestingly, in Figure 3-28, the power around 70 Hz and 120 Hz of the "control on" case is higher than that of the "control off" case. This is generally defined as spillover (Hong and Bernstein 1998). Hong and Bernstein (1998) used the Bode integral constraint to analyze the spillover problem and concluded that the spillover is inevitable if the reference and performance signals are collocated or the disturbance and control actuators are collocated. For this vibration control test, the reference and performance signals are collocated, thus the spillover is unavoidable.

Figure 3-29, Figure 3-30 and Figure 3-32 show the performance of the disturbance rejection algorithm with varying n_c, μ_c and Υ, respectively, while other parameters are held constant. From Table 3-2 and Table 3-3, it is interesting to find that there is not much difference of the suppression performance for varying n_c and μ_c. However, the step size parameter Υ does play a significant role. Larger Υ gives much faster convergence and better performance. However, if Υ is too large, it is possible for the controller to become unstable. This tradeoff should be kept in mind when choosing Υ.

The disturbance rejection controller can also be run at the "ID and control" mode. In this mode, the band-limited white noise with frequency of $0 - 150$ Hz and variance of 0.09 is used to excite the disturbance piezoceramics. Meanwhile, the band-limited white noise with frequency of $0 - 150$ Hz and variance of 0.01 is added to the controller output. The control signal is shown in Figure 3-33 and the performance signal is shown in Figure 3-34. Comparing with Figure 3-27, the control signal of the "ID and control" case is significantly larger at the beginning because of the additive signal u_{ID} and the evolution of the controller output is "buried" under it.

Figure 3-35 compares the power spectra of the performance signal of the two different modes. It is surprising that the "ID and control" mode results in lower power around the natural frequency of the beam. This is hard to see in Figure 3-34 because the "ID, then control" mode seems much better. However, it is not surprising that the "ID and control" mode results in higher power at other frequencies than the natural frequency because of the additive signal u_{ID}. In addition, Table 3-5 shows that the "ID, then control" mode gives better suppression performance of the overall power.

Unfortunately, for this setup, it is not feasible to test the adaptability of the two modes. However, this will be done in the wind tunnel experiments.

As a summary, the computational tests are conducted first to determine how the parameters affect the computational complexity of the system ID and control algorithms. It is shown that the averaging window number p has much more significant impact on the computational intensity than the other two parameters for the system ID algorithm. The dependence of the computational complexity vs. n is approximately twice of that for μ. Similarly it is found that the turnaround time of the control algorithm is approximately linearly proportional to n_c and μ_c, while the slope for n_c is approximately twice of that for μ_c.

The ARMARKOV/Toeplitz system ID algorithm successfully identifies the system (control model) and results in very good frequency response approximations. A significant improvement of the performance of the ARMARKOV system ID over the ARMA (when $\mu=1$) system ID is found. However, too many Markov parameters of the ARMARKOV system ID may be detrimental to the performance. Higher SNR improves the performance, thus when the system ID is conducted with unknown noise, the input signal should be chosen as large as possible within the maximum allowable level.

The order of the controller n_c and the number of Markov parameters μ_c do not play significant roles on the performance of the ARMARKOV controller for this vibration control test. However, this conclusion may vary with different systems and remains to be investigated. The step size constant Υ significantly affects the convergence rate of the controller. Υ should be chosen as large as possible before it makes the controller unstable. The spillover effect is identified in this vibration control test. This effect is unavoidable because the "reference signal" and "performance signal" are collocated (Hong and Bernstein 1998).

summarizes all the parameters that are used in the simulations. Recall that the detailed derivation of algorithm is given in Chapter 2. Note that the parameters a and w are the main factors that affect the convergence rate and stability. Thus, they are varied in the simulations to understand how they affect the performance of the algorithm.

Figure 3-6 demonstrates how a affects the convergence rate while w is fixed to be 50 Hz. Clearly, the convergence rate increases when a decreases. This is consistent with the analytical solution shown in eqn. (17) for $k=1/a^2$, where the convergence rate ($f^{"}ak/2$) is dependant on $1/a$. However, when a is too small, the algorithm becomes unstable. Figure 3-7 shows how w affects the convergence rate while a is fixed to be 0.001. Apparently, the convergence rate increases with w. When w is too large, the algorithm again becomes unstable.

Figure 3-8 and Figure 3-9 show the results of the double hump model. Clearly, the extremum seeking algorithm drives the cost function f to the local minimum.

3.2 Vibration Control Testbed Setup

Figure 3-10 shows a detailed sketch of the whole vibration control testbed setup. A thin aluminum cantilever beam with one piezoceramic plate bonded to each side is fixed on a block base and connected to the ground. The two piezoceramic plates are used to excite the beam by applying electrical field across their thickness. The piezoceramic plate bonded to the upper side of the beam is called the "disturbance piezoceramic" because it is used to apply a disturbance excitation to the beam. The piezoceramic plate bonded to the lower side of the beam is called the "control piezoceramic" because it is supplied with the controller output signal to counteract the disturbance actuator. The beam system has a natural frequency of about 97 Hz.

The goal of the disturbance rejection controller is to mitigate the vibration of the aluminum beam generated by an unknown disturbance signal. The controller tries to generate a signal to counteract the vibration of the aluminum beam generated by the "disturbance piezoceramic". The performance (or the residue) signal of the controller is measured at the center of the tip of the beam by a laser-optical displacement sensor. The performance signal is filtered by a high pass filter with $f_c = 1H_z$ to filter out the dc offset of the displacement sensor and then amplified by an amplifier with a gain of 10.

The disturbance and control signals are generated by our dSPACE (Model DS1005) DSP system with 466MHz PowerPC CPU and amplified by two separate channels of an amplifier by a same gain of 50. The types and conditions of the signals are discussed in details in the next section. The dSPACE system has a 16-bit A/D and a 16-bit D/A board. The computer can acquire data using Mlib/Mtrace programs in MATLAB through the dSPACE system.

The whole system was a two-input/two-output system. One input was the control signal and the other input was the "unmeasured" disturbance signal. The two outputs are termed a "reference output" and a "performance output". For this validation test, the reference and performance outputs were identical. The disturbance rejection algorithm was implemented in the Simulink environment and compiled and downloaded to the dSPACE system. The disturbance signal was band-limited white noise with frequency of 0-150 Hz.

The disturbance rejection algorithm runs in one of the following two modes: 1) "ID, then control" (shown in Figure 3-11): the system (control model) is identified by the ARMARKOV/Toeplitz system ID algorithm and the identified system weight matrix B_{zu} is transferred to the ARMARKOV control algorithm; then the controller is turned on and the "control signal" is switched to the controller output. 2) "ID and control" (shown in Figure 3-12): the ID and control are turned on simultaneously. The input (u_{ID}) to the system for ID can be either band-limited white noise or a repetitive linear chirp signal. The controller uses the identified system to achieve maximum suppression of the vibration of the beam, subject to constraints on the maximum allowable actuator signal. The "ID and control" mode is better when the system is a time variant system because this mode updates the system information during every iteration. However, the "ID and control" mode adds an additional signal u_{ID} to the control signal all the time and this certainly affects the performance of the disturbance rejection controller. The tradeoff between the adaptation ability and effects on the performance should be kept in mind.

3.3 Results of the Vibration Control Tests

3.3.1 Computational Tests

For real-time control applications, the turnaround time (defined as the time for the program to execute one iteration) is required to be less than the sampling time. Complex algorithms are computationally intensive and have large turnaround time, which requires choosing a corresponding larger sampling time (or a smaller sampling frequency f_s). From the Shannon sampling theorem, the sampling frequency must be larger than twice the highest frequency of interest to avoid aliasing. Thus, algorithms with high computational complexity may not be feasible in flow control applications. The tradeoff between choosing a large f_s to satisfy the sampling theorem and choosing a small f_s to allow a large turnaround time must be considered. This section analyzes the effects of varying the parameters of the ID and control

algorithms on the computational intensity. This serves as a reference for choosing the parameters with regard to the computational intensity.

The sampling frequency was 1024 Hz for the computational tests. In Figure 3-13 and Figure 3-14, the turnaround time of the system ID algorithm by varying either μ, n or p is plotted, while the other two parameters are fixed at unity. It is shown that the turnaround time is approximately linearly proportional to both μ and n, while the slope for n is approximately twice of that for μ. The dependence of the turnaround time on p is approximately quadratic. Clearly the averaging window number p has much more significant impact on the computational intensity than the other two parameters. Figure 3-15 investigates the effects of varying p on the computational intensity with respect to n+μ. As shown, the computational intensity is proportional to p. From these results, it is suggested to hold p to be a small number and increase μ to improve the system ID performance.

Figure 3-16 shows the effects of varying n_c or μ_c on the computational intensity of the ARMARKOV disturbance rejection algorithm. The results are similar to those of the system ID algorithm. The turnaround time is approximately linearly proportional to n_c and μ_c while the slope for n_c is approximately twice that for μ_c.

3.3.2 System Identification

The ARMARKOV/Toeplitz system ID algorithm requires the following three parameters: the order of the system n, the number of Markov parameters μ, and a parameter p that determines the size of the averaging window. The SNR is also a parameter that can affect the performance of the system ID algorithm. When the number of Markov parameters is unity, the ARMARKOV model reduces to an ARMA model. The values of the parameters are limited by the requirement that the turnaround time must be less the sampling time. As shown in the last section, μ has the smallest effect on the turnaround time; thus in this section the performance of the system ID algorithm with varying μ is compared.

The offline non-parametric fit of the frequency response of the beam system is also implemented as a comparison and shown as green dot lines in Figure 3-20 - Figure 3-23. The non-parametric fit uses the "invfreqz" command in MATLAB and implements a second order approximation. The "invfreqz" command returns the system matrices A and B of the state space representation. The zero-pole map of the non-parametric fitted system is shown in Figure 3-17. As shown, the beam system is a low damping system because it has two poles that are very close to the unit circle. The controllability matrix is $[B\ AB]=[1\ 1.655;0\ 1]$ (for a second order system), which has full rank 2. This means that the system is controllable.

The sampling frequency was 1024 Hz. The input signal used for the system ID was a periodic chirp signal. The frequency response shown in Figure 3-20 - Figure 3-23 was implemented with NFFT=1024, no overlap, and a rectangular window.

Figure 3-18 shows a very good match between the measured and fitted outputs of the system with the system ID parameters of p=n=2, μ=10 and SNR=20 dB. Meanwhile, as shown in Figure 3-19, the weight tracks of the system ID converge at about 0.5 seconds.

Figure 3-20 to Figure 3-23 show the comparison between the measured and fitted frequency response with the system ID parameters of p=n=2, SNR=20 dB and varying μ. A significant improvement of the system ID is obtained when μ changes from 1 (ARMA case) to 10. Figure 3-24 compares the mean square error (MSE) verse time of the system ID with

40

varying μ. Surprisingly, it is found that the case with $\mu=10$ has the best performance. This indicates that for the beam system, increasing the number of Markov parameters does not necessarily improve the system ID performance. This also suggests that for a certain system, there may exist an optimal number of Markov parameters. It is also shown in Figure 3-24 that for the case with $\mu=40$, the convergence rate is slower than the case with $\mu=1$, although the final MSE is better. This indicates that too many Markov parameters may be detrimental to the performance of the ARMARKOV/Toeplitz system ID.

Figure 3-25 compares the mean square error (MSE) verse time of the system ID with varying SNR. The SNR is computed by using the formula: $SNR=10\log_{10}(\sigma_s^2/\sigma_n^2)$, where σ_s^2 is the variance of the control signal and σ_n^2 is the variance of the disturbance signal. It is clear that the system ID performs better with a higher SNR. This suggests that when the system ID is conducted with unknown disturbance, it is better to apply a large system input within the maximum allowable range.

3.3.3 Adaptive Disturbance Rejection

The ARMARKOV disturbance rejection algorithm requires the following three parameters: the order of the controller n_c, the number of Markov parameters of the controller μ_c and the adaptive step size constant γ that controls the convergence rate of the controller.

The controller uses the system information identified by the ARMARKOV/Toeplitz system ID with the parameters of $p=n=2$, $\mu=10$ and SNR=20 dB (shown in Figure 3-21). All cases of the controller design use the same identified system.

Band-limited white noise with frequency of 0 – 150 Hz and variance of 0.09 is used to excite the disturbance piezoceramics. Figure 3-26 and Figure 3-27 show the time data of the performance and control signals with the parameters of $n_c=2$, $\mu_c=20$ and $\gamma=1$. The system ID is off for the whole period and the controller is off initially and turned on at t = 20 sec. In Figure 3-28, the power spectra of the performance signal with control off and on are compared. The power spectra were calculated by using the time data of 20-second duration with NFFT=1024, 50% overlap and a hanning window. The "control on" case is taken after the controller is turned on for 30 seconds. The performance of suppression is calculated by $10g\log_{10}\left(\sigma_{off}^2/\sigma_{on}^2\right)$ and this case gives 11.7 dB suppression. Interestingly, in Figure 3-28, the power around 70 Hz and 120 Hz of the "control on" case is higher than that of the "control off" case. This is generally defined as spillover (Hong and Bernstein 1998). Hong and Bernstein (1998) used the Bode integral constraint to analyze the spillover problem and concluded that the spillover is inevitable if the reference and performance signals are collocated or the disturbance and control actuators are collocated. For this vibration control test, the reference and performance signals are collocated, thus the spillover is unavoidable.

Figure 3-29, Figure 3-30 and Figure 3-32 show the performance of the disturbance rejection algorithm with varying n_c, μ_c and γ, respectively, while other parameters are held constant. From Table 3-2 and Table 3-3, it is interesting to find that there is not much difference of the suppression performance for varying n_c and μ_c. However, the step size parameter γ does play a significant role. Larger γ gives much faster convergence and better performance. However, if γ is too large, it is possible for the controller to become unstable. This tradeoff should be kept in mind when choosing γ.

The disturbance rejection controller can also be run at the "ID and control" mode. In this mode, the band-limited white noise with frequency of 0 – 150 Hz and variance of 0.09 is used to excite the disturbance piezoceramics. Meanwhile, the band-limited white noise with frequency of 0 – 150 Hz and variance of 0.01 is added to the controller output. The control signal is shown in Figure 3-33 and the performance signal is shown in Figure 3-34. Comparing with Figure 3-27, the control signal of the "ID and control" case is significantly larger at the beginning because of the additive signal u_{ID} and the evolution of the controller output is "buried" under it.

Figure 3-35 compares the power spectra of the performance signal of the two different modes. It is surprising that the "ID and control" mode results in lower power around the natural frequency of the beam. This is hard to see in Figure 3-34 because the "ID, then control" mode seems much better. However, it is not surprising that the "ID and control" mode results in higher power at other frequencies than the natural frequency because of the additive signal u_{ID}. In addition,

Table 3-5 shows that the "ID, then control" mode gives better suppression performance of the overall power.

Unfortunately, for this setup, it is not feasible to test the adaptability of the two modes. However, this will be done in the wind tunnel experiments.

As a summary, the computational tests are conducted first to determine how the parameters affect the computational complexity of the system ID and control algorithms. It is shown that the averaging window number p has much more significant impact on the computational intensity than the other two parameters for the system ID algorithm. The dependence of the computational complexity vs. n is approximately twice of that for μ. Similarly it is found that the turnaround time of the control algorithm is approximately linearly proportional to n_c and μ_c, while the slope for n_c is approximately twice of that for μ_c.

The ARMARKOV/Toeplitz system ID algorithm successfully identifies the system (control model) and results in very good frequency response approximations. A significant improvement of the performance of the ARMARKOV system ID over the ARMA (when $\mu=1$) system ID is found. However, too many Markov parameters of the ARMARKOV system ID may be detrimental to the performance. Higher SNR improves the performance, thus when the system ID is conducted with unknown noise, the input signal should be chosen as large as possible within the maximum allowable level.

The order of the controller n_c and the number of Markov parameters μ_c do not play significant roles on the performance of the ARMARKOV controller for this vibration control test. However, this conclusion may vary with different systems and remains to be investigated. The step size constant Υ significantly affects the convergence rate of the controller. Υ should be chosen as large as possible before it makes the controller unstable. The spillover effect is identified in this vibration control test. This effect is unavoidable because the "reference signal" and "performance signal" are collocated (Hong and Bernstein 1998).

Table 3-1. Parameters for the simulations.

Fs (Hz)	500
Perturbation amplitude	$a = 0.001, 0.002, 0.005$
Adaptation gain	$k = 1/a^2$
Perturbation frequency (Hz)	$w = 30, 40, 50$

High pass filter cutoff frequency (Hz)	$w_h = 10$
Low pass filter cutoff frequency (Hz)	$w_l = 10$

Table 3-2. Suppression performance of the disturbance rejection algorithm with $\mu_c = 20$, $\Upsilon = 0.1$ and varying n_c.

$\mu_c = 20$, $\Upsilon = 0.1$	$n_c = 1$	$n_c = 5$	$n_c = 10$
Suppression (dB)	8.9	8.6	9.0

Table 3-3. Suppression performance of the disturbance rejection algorithm with $n_c = 2$, $\Upsilon = 0.1$ and varying μ_c.

$n_c = 2$, $\Upsilon = 0.1$	$\mu_c = 1$	$\mu_c = 20$	$\mu_c = 40$
Suppression (dB)	8.4	8.7	7.9

Table 3-4. Suppression performance of the disturbance rejection algorithm with $n_c = 2$, $\mu_c = 20$ and varying Υ.

$n_c = 2$, $\mu_c = 20$	$\Upsilon = 0.01$	$\Upsilon = 0.1$	$\Upsilon = 1$
Suppression (dB)	3.9	8.9	11.7

Table 3-5. Suppression performance of the disturbance rejection algorithm at different modes with $n_c = 2$, $\mu_c = 20$ and $\Upsilon = 0.1$.

$n_c = 2$, $\mu_c = 20$ and $\Upsilon = 0.1$	ID, then control	ID and control
Suppression (dB)	7.1525	4.9994
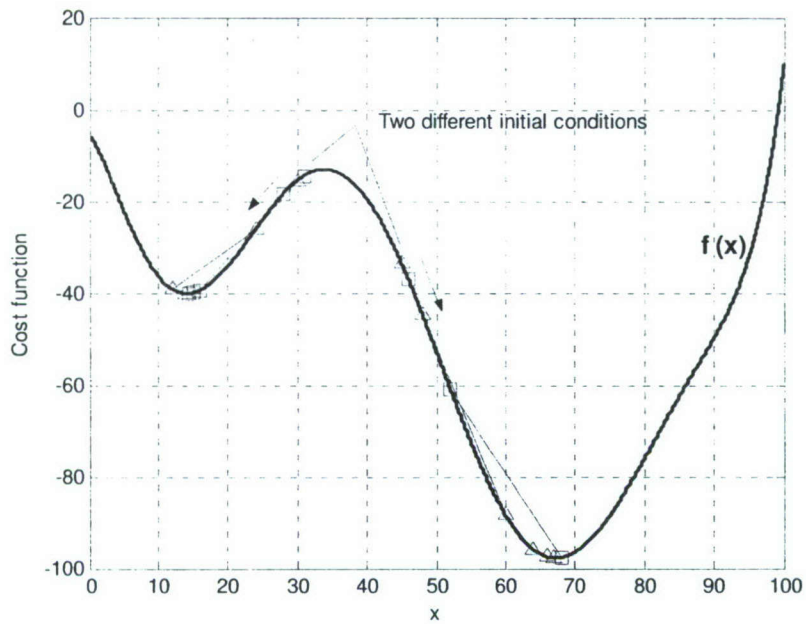
Figure 3-1. One-dimensional example of the downhill simplex algorithm.
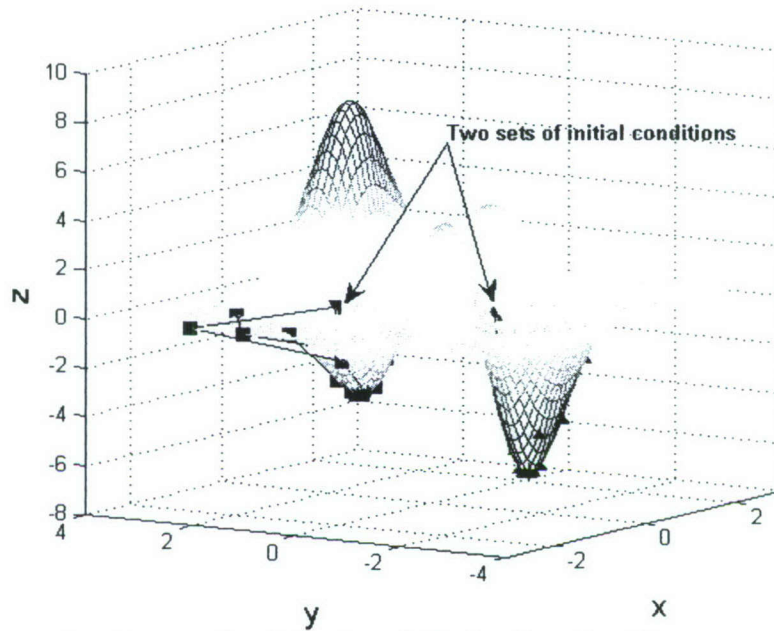
Figure 3-2. Two-dimensional example of the downhill simplex algorithm.
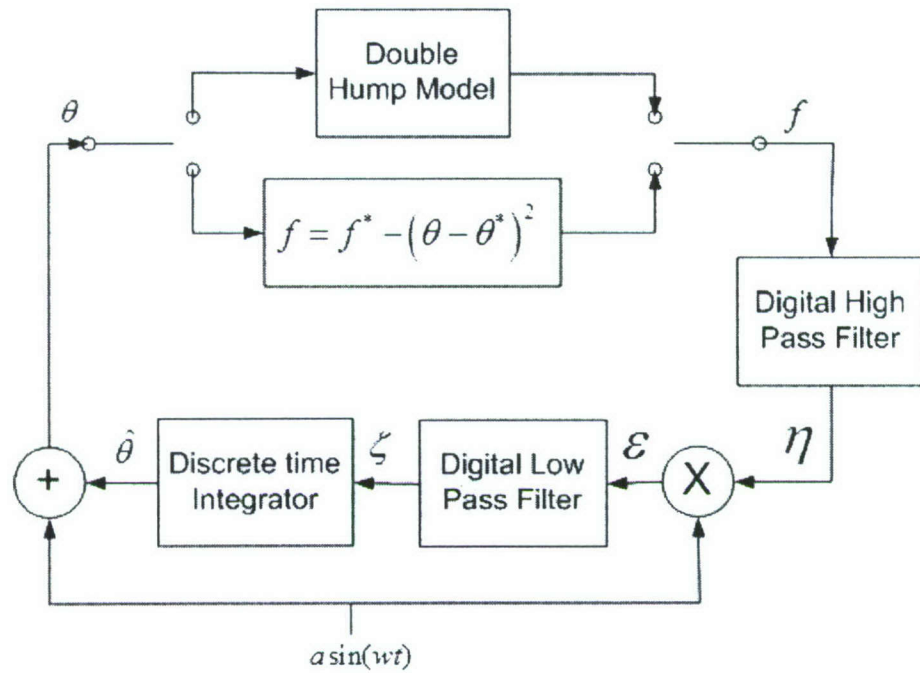
Figure 3-3. Simulation block diagram for extremum seeking control.
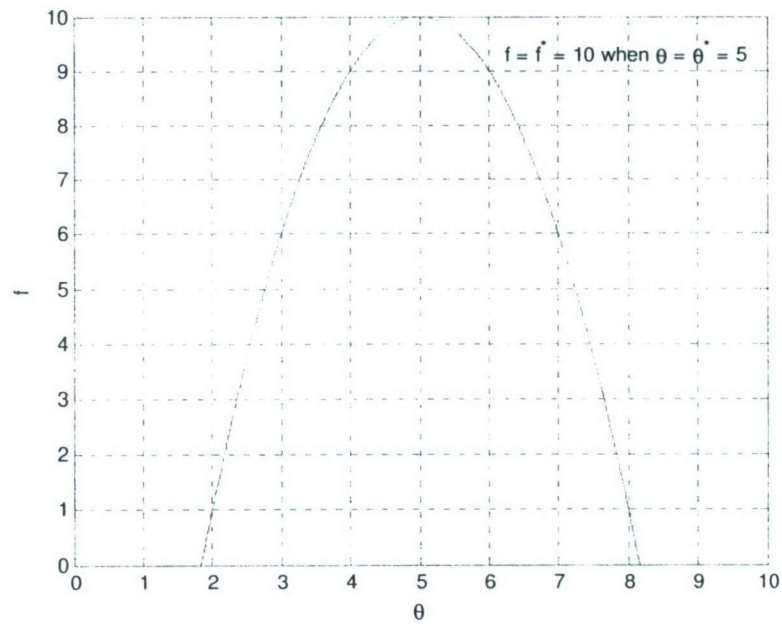
Figure 3-4. Single global maximum test model: $f=f^*-(\theta-\theta^*)^2$, where $f^*=10$ and $\theta^*=5$.
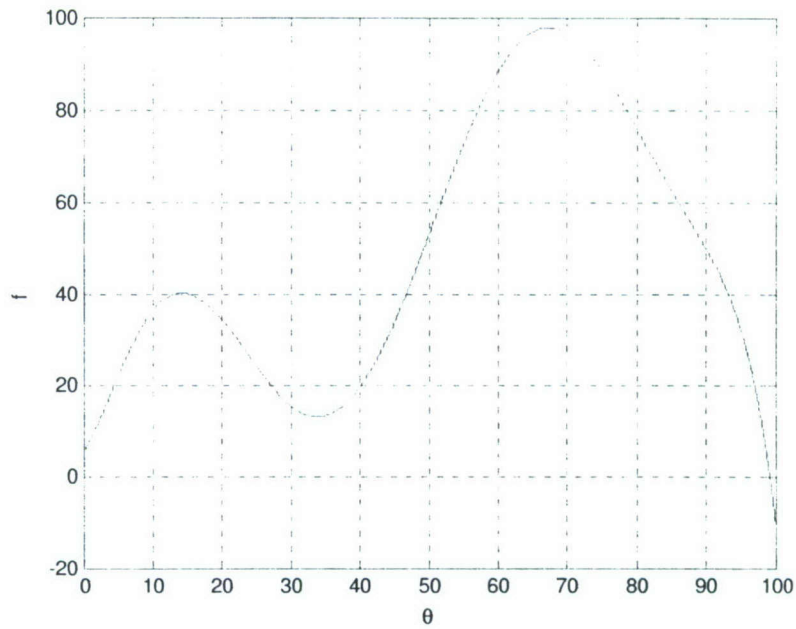
Figure 3-5.　Double hump model with one local maximum and one global maximum. The function is fitted by a polynomial:
$$f(\theta)=-1.2e^{-12}\theta^8-1.6e^{-10}\theta^7+1.4e^{-7}\theta^6-2.3e^{-5}\theta^5$$
$$+1.5e^{-3}\theta^4-4.4e^{-2}\theta^3+3.8e^{-1}\theta^2+2.3\theta+5.4$$
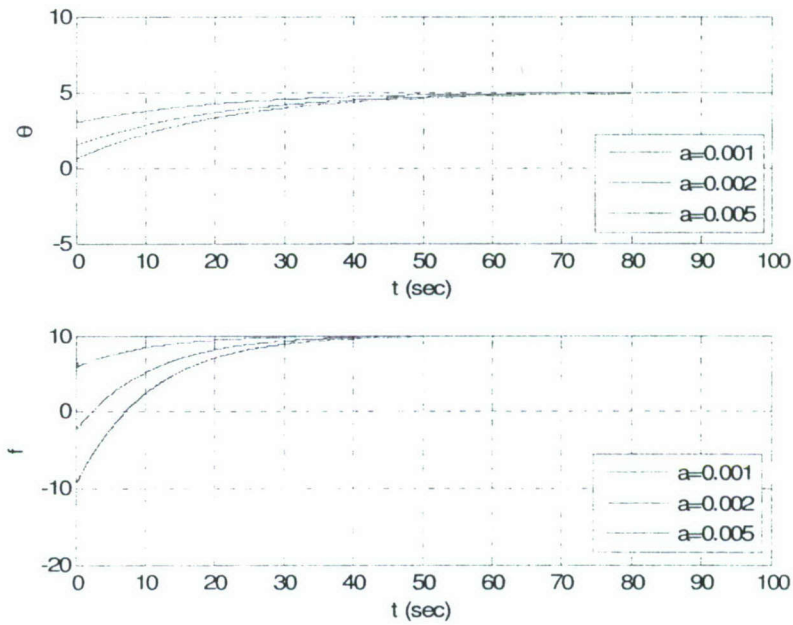
Figure 3-6.　θ converges to the optimal input $\theta^*=5$ and f converges to the global maximum $f^*=10$ at various convergence rates due to various values of a while $w=50$.
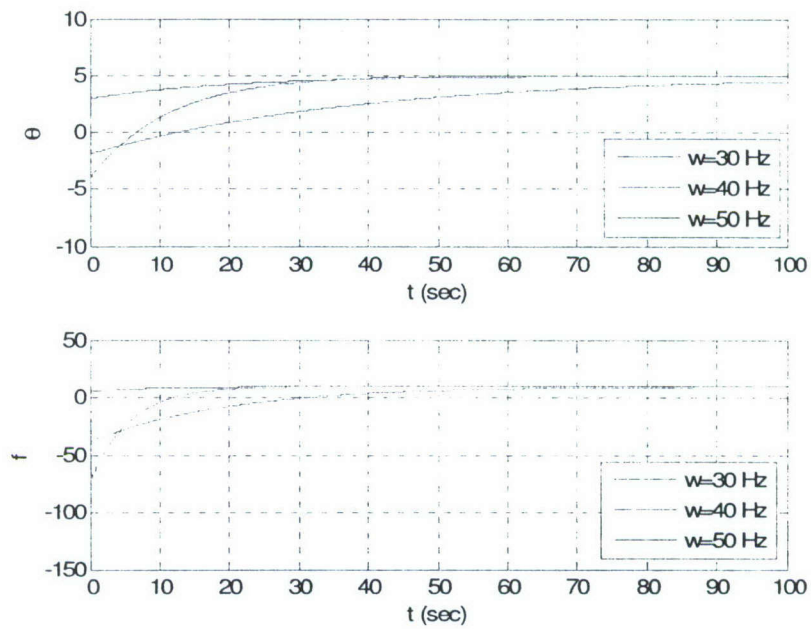
46

Figure 3-7. θ converges to the optimal input $\theta^*=5$ and f converges to the global maximum $f^*=10$ at various convergence rates due to various values of w while a=0.001.
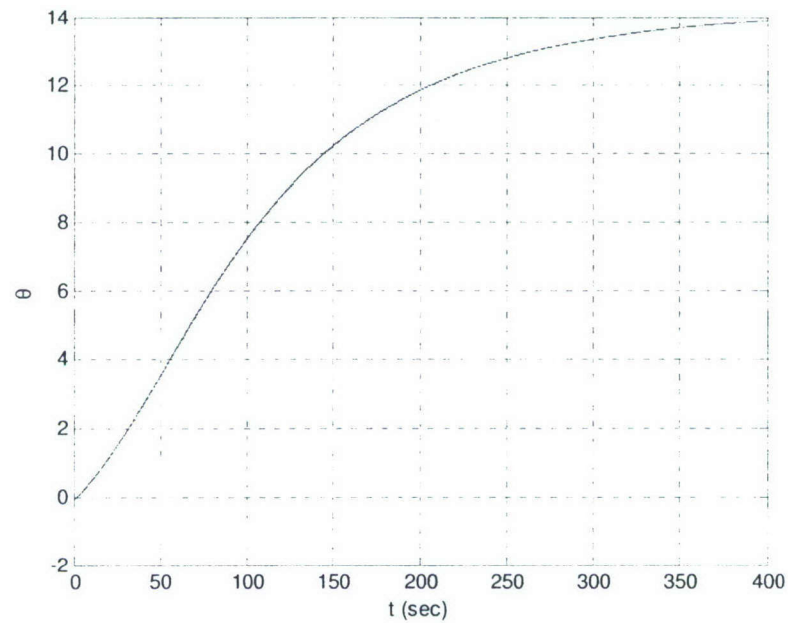
Figure 3-8. θ converges to the local optimal input (see Figure 3-5) $\theta^*=14$. (a=0.001,w=50).
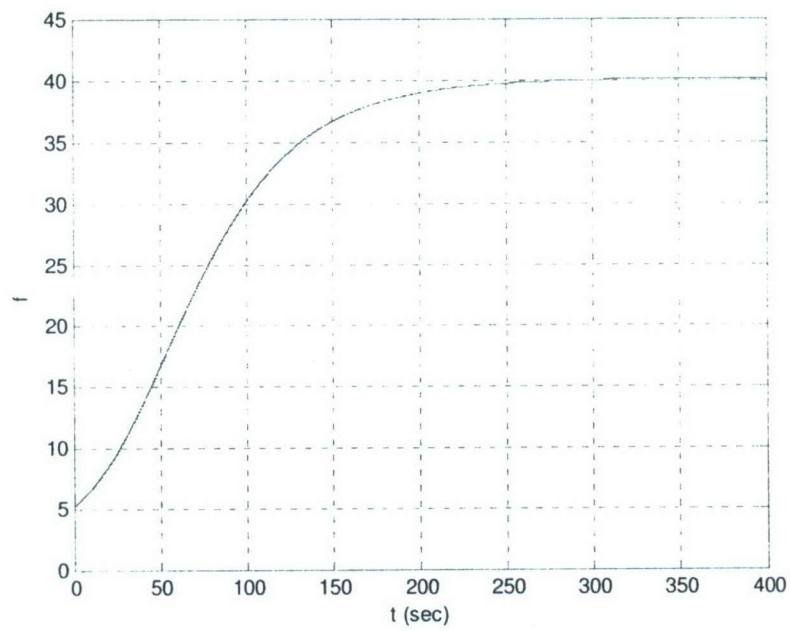
Figure 3-9. f converges to the local maximum (see Figure 3-5) f=40. (a=0.001,w=50).
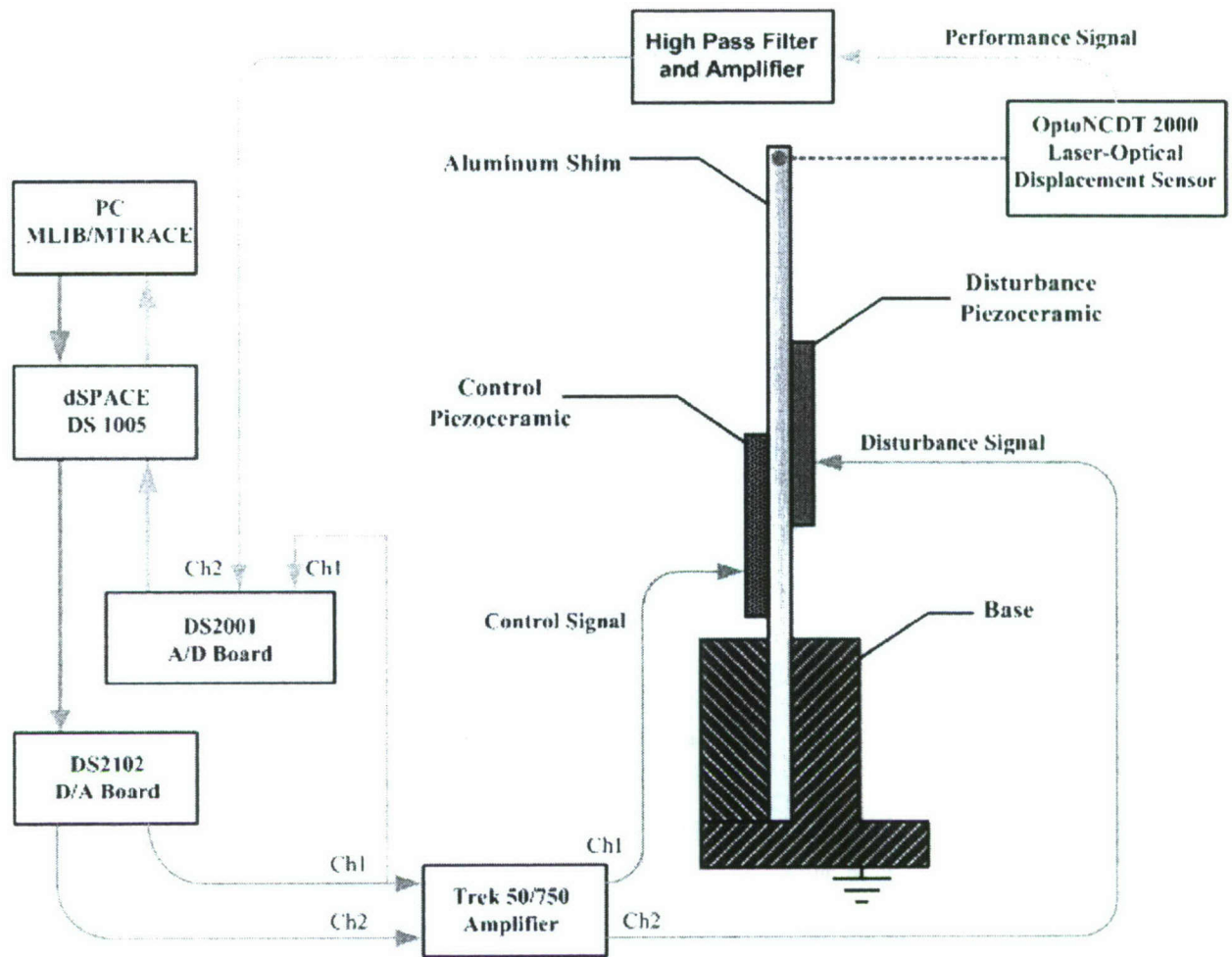
Figure 3-10. Vibration Control Testbed.
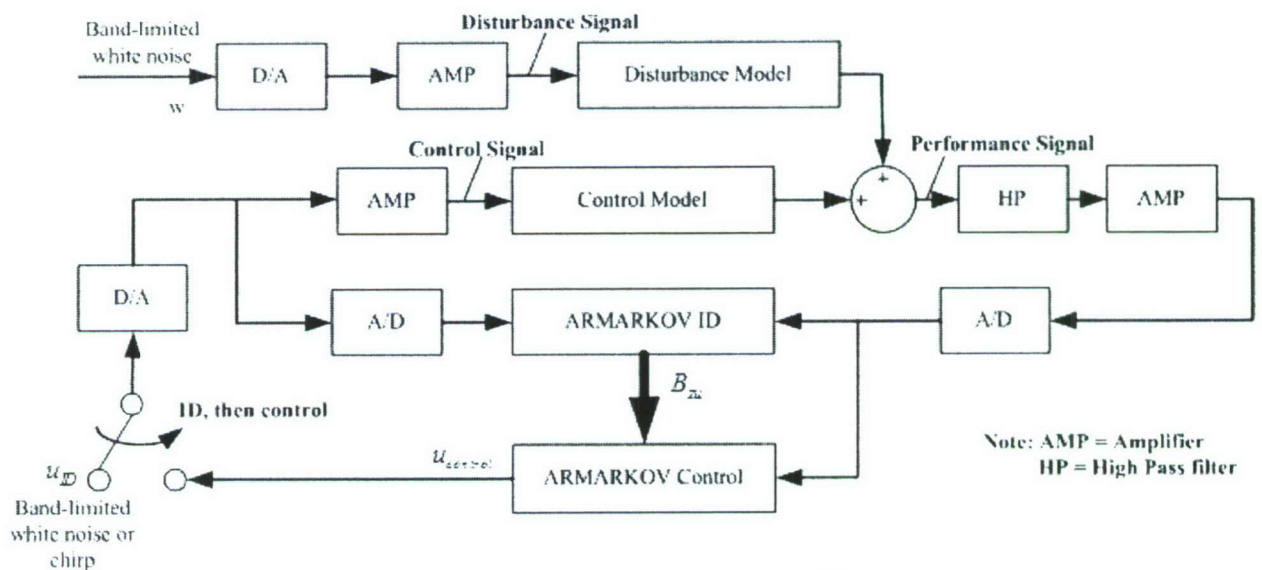
Figure 3-11. Block diagram of vibration control with "ID, then control".
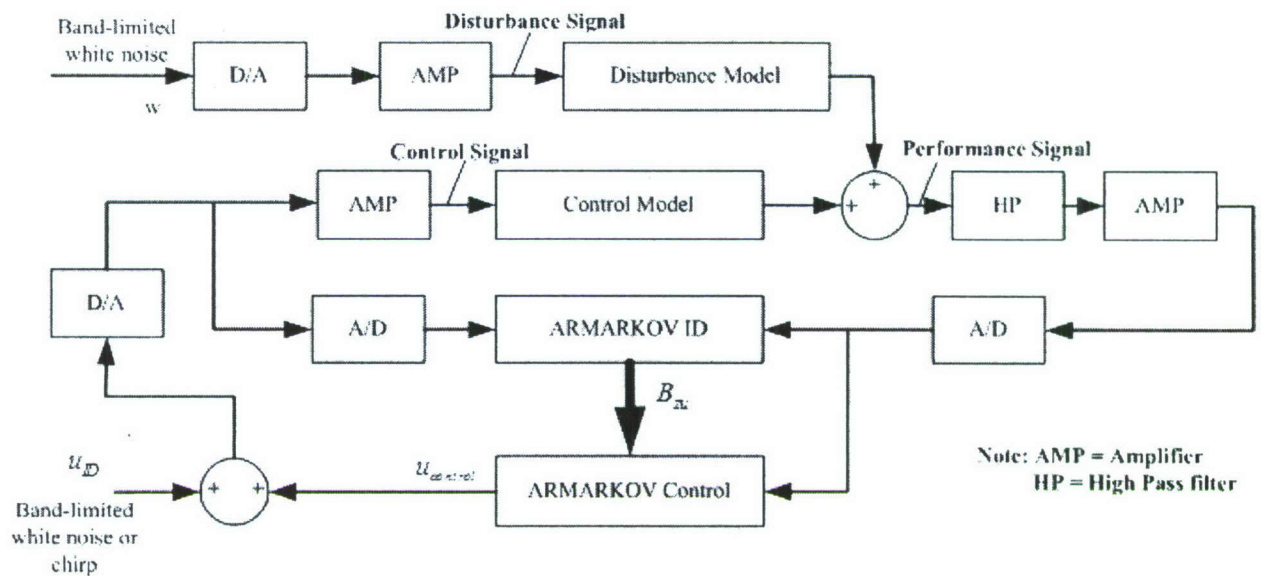
Figure 3-12. Block diagram of vibration control with "ID and control".
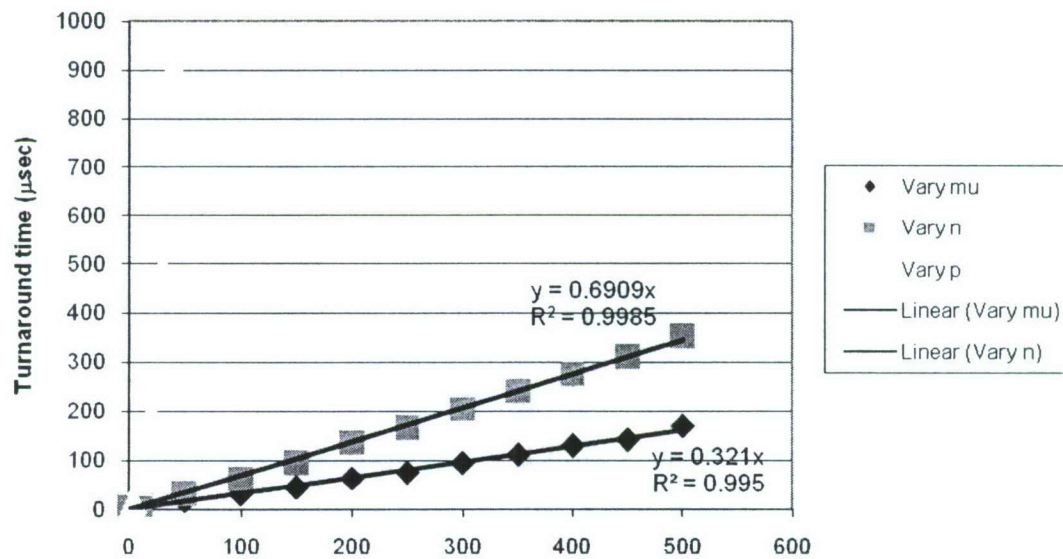
Figure 3-13. Effects of varying μ, n or p on the computational intensity of the ARMARKOV/Toeplitz system ID.
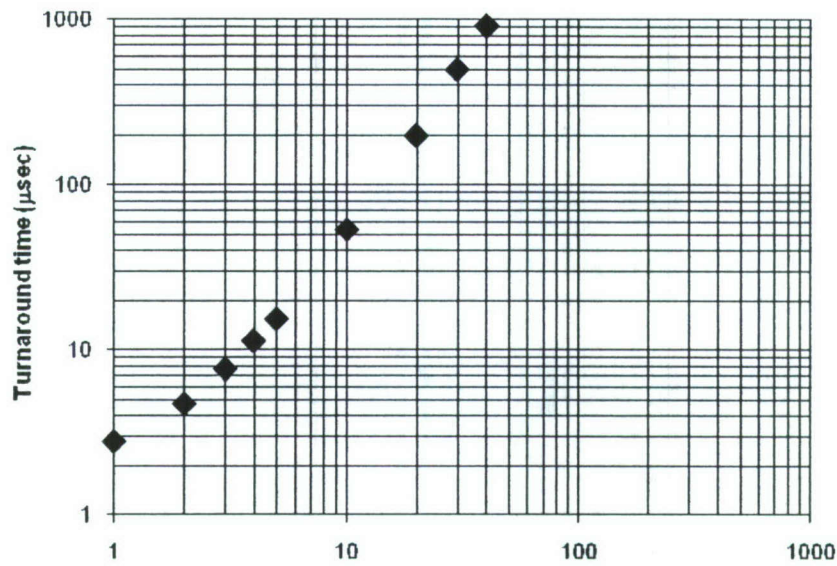
Figure 3-14. Effects of varying p on the computational intensity of the ARMARKOV/Toeplitz system ID.
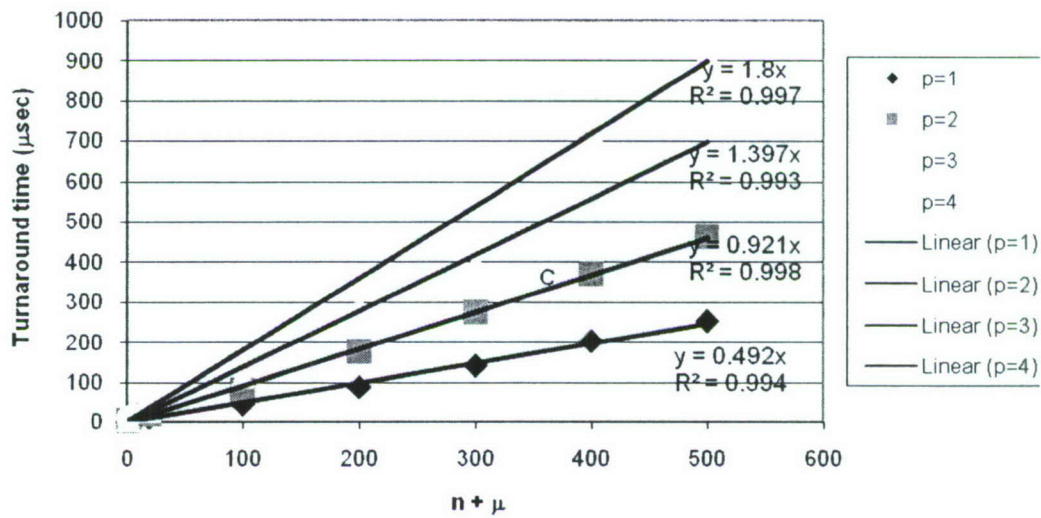
Figure 3-15. Effects of varying p on the growth rate of the computational intensity of the ARMARKOV/Toeplitz system ID with respect to $n+\mu$.
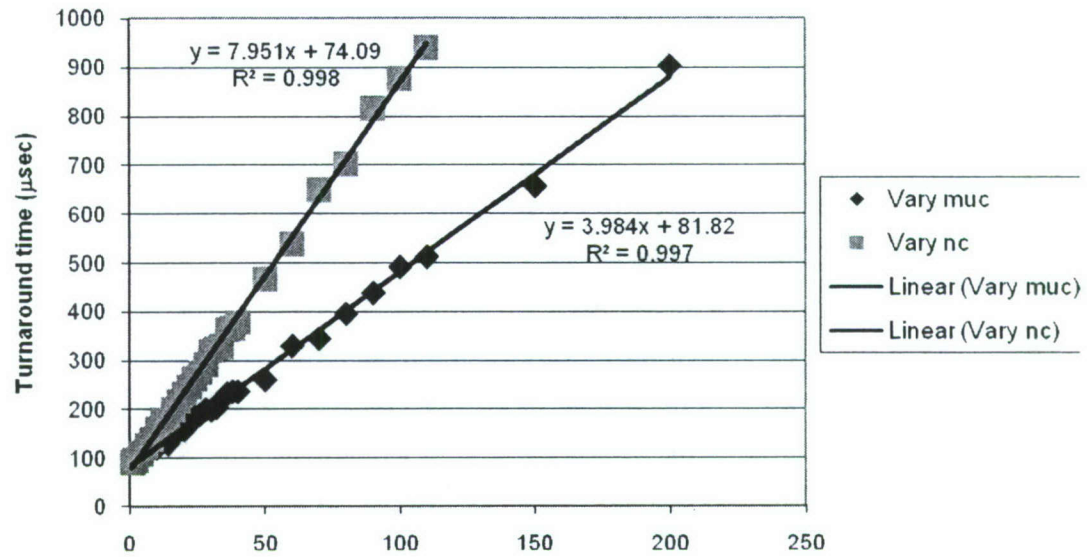
Figure 3-16. Effects of varying n_c or μ_c on the computational intensity of the ARMARKOV disturbance rejection.
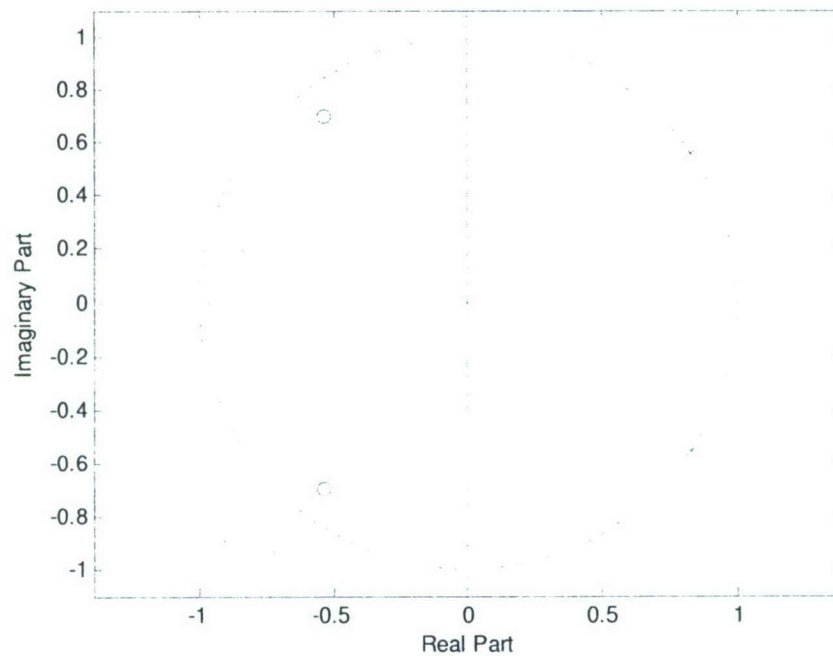
Figure 3-17. Zero-pole map of the non-parametric fit of the frequency response.
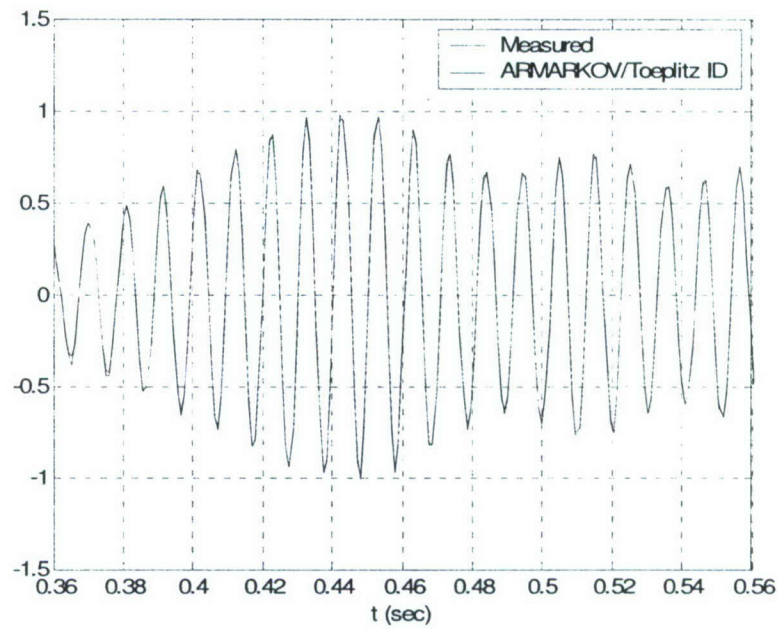
Figure 3-18. Measured output and fitted output by the ARMARKOV/Toeplitz system ID with $p=n=2$, $\mu=10$ and SNR=20 dB.
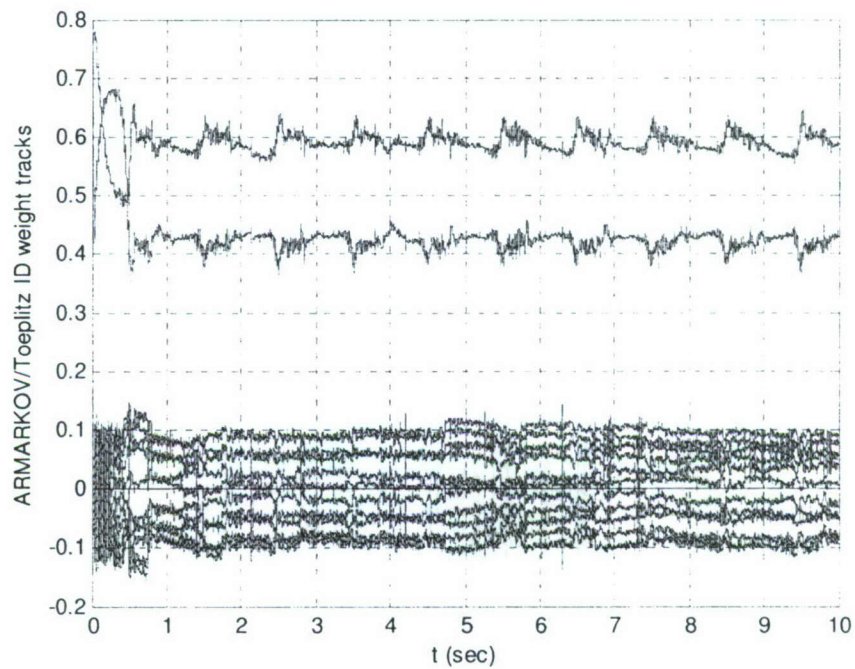
Figure 3-19. Weight tracks of the ARMARKOV/Toeplitz system ID with $p=n=2$, $\mu=10$ and SNR=20 dB.
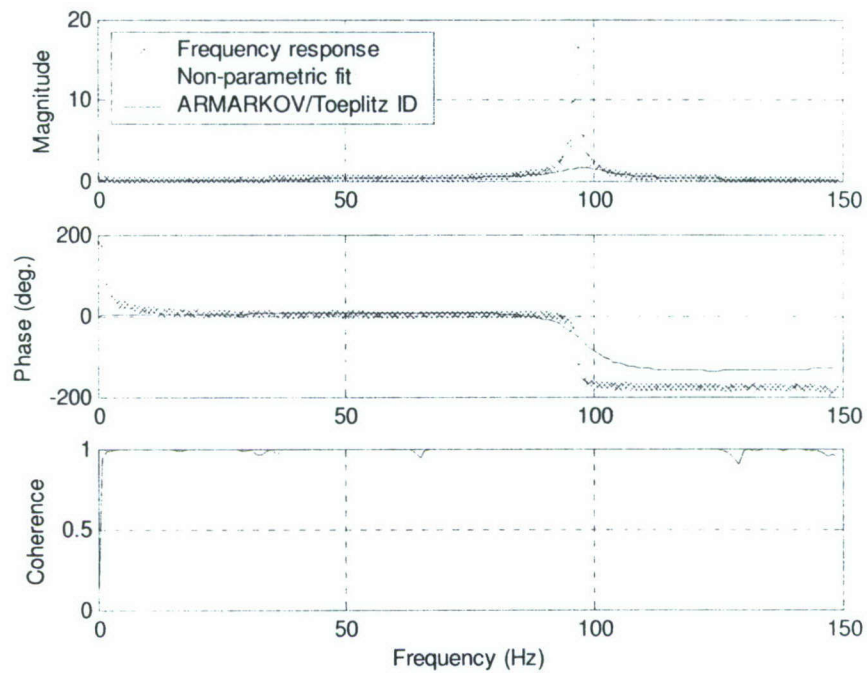
Figure 3-20. Comparison of measured frequency response, non-parametric fit and the ARMARKOV/Toeplitz system ID with p=n=2, μ=1 and SNR=20 dB.
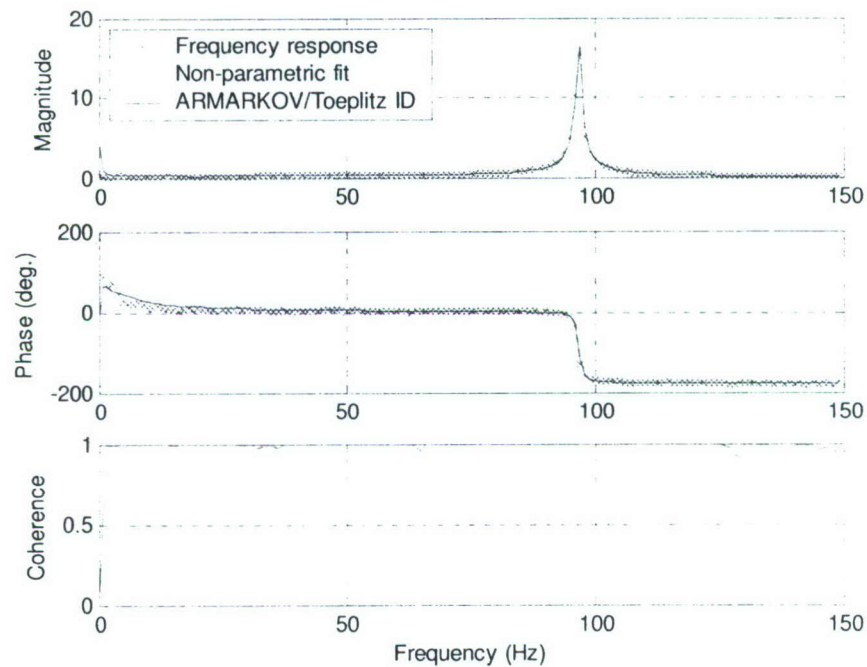
Figure 3-21. Comparison of measured frequency response, non-parametric fit and the ARMARKOV/Toeplitz system ID with p=n=2, μ=10 and SNR=20 dB.
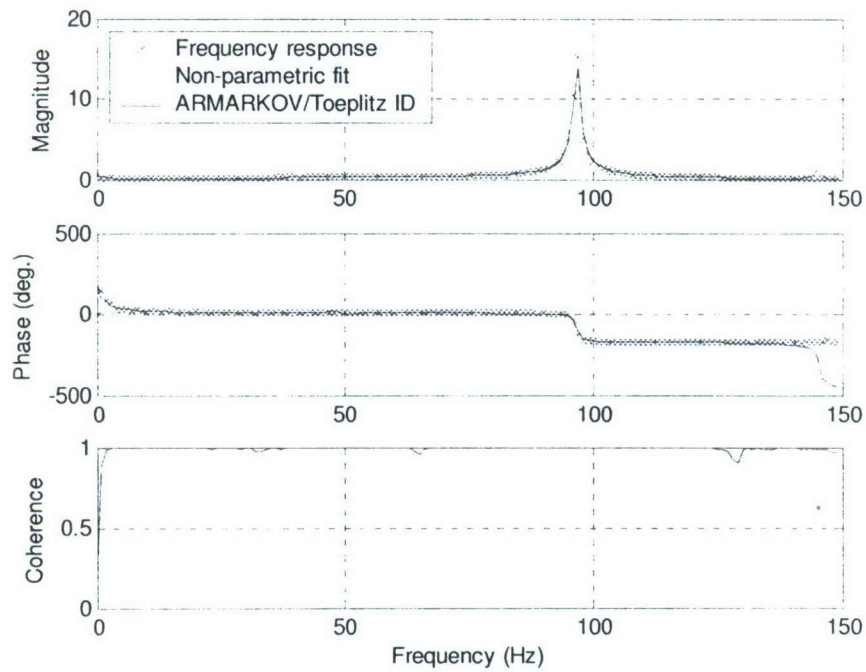
Figure 3-22. Comparison of measured frequency response, non-parametric fit and the ARMARKOV/Toeplitz system ID with $p=n=2$, $\mu=20$ and SNR=20 dB.
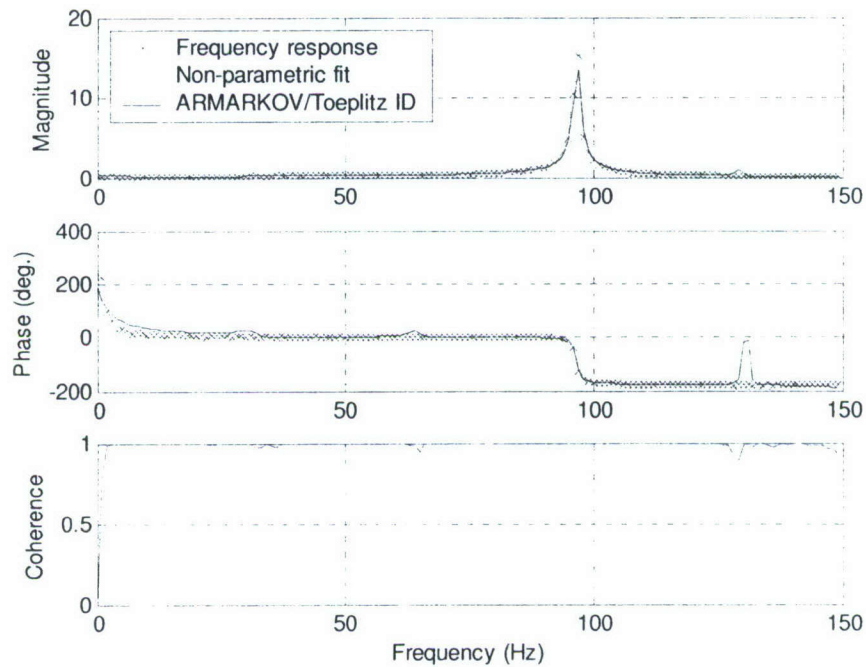
Figure 3-23. Comparison of measured frequency response, non-parametric fit and the ARMARKOV/Toeplitz system ID with $p=n=2$, $\mu=30$ and SNR=20 dB.
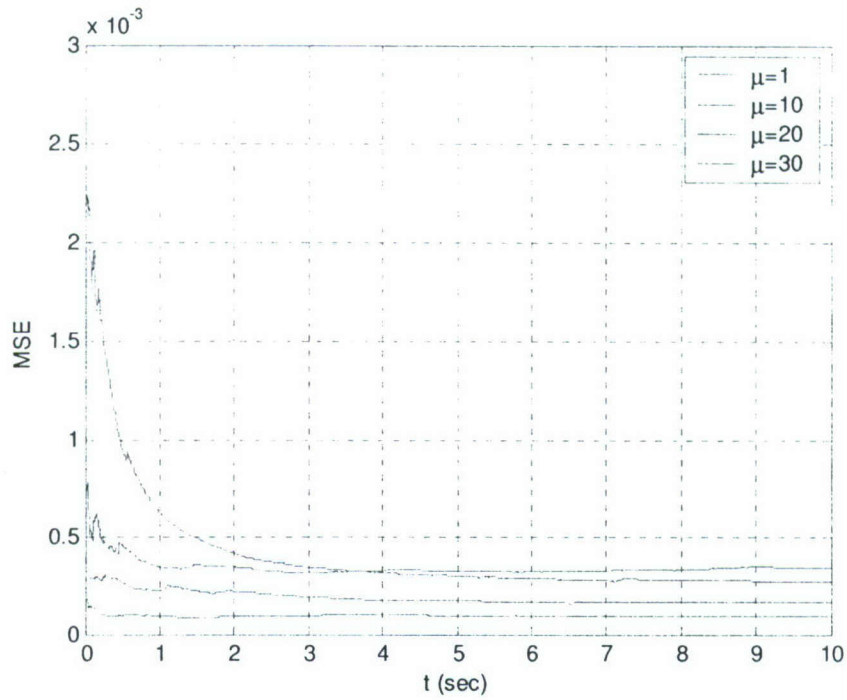
Figure 3-24. Comparison of MSE of the ARMARKOV/Toeplitz system ID with p=n=2, SNR=20 dB with different μ.
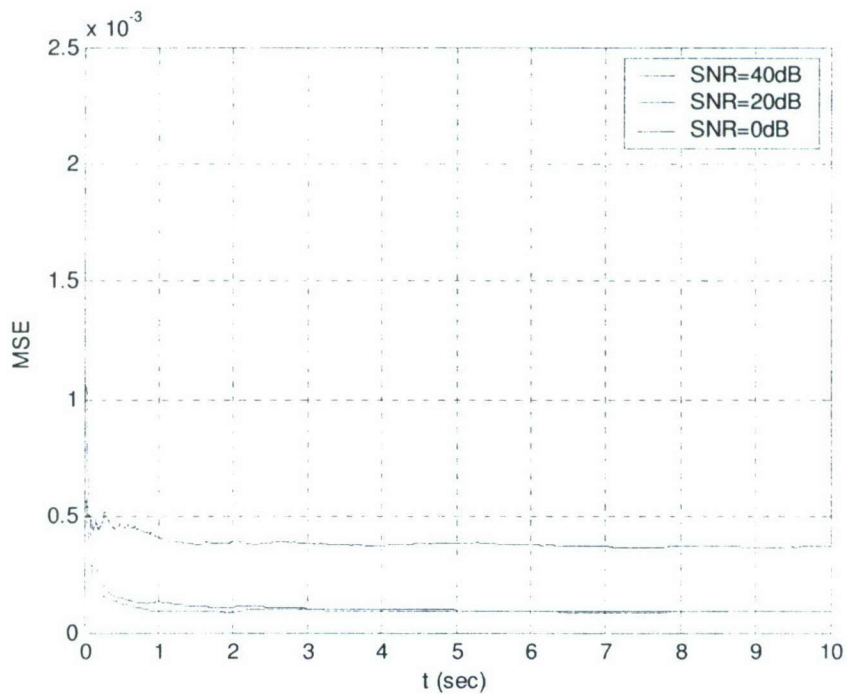
Figure 3-25. Comparison of MSE of the ARMARKOV/Toeplitz system ID with p=n=2, μ=20 with different SNR.
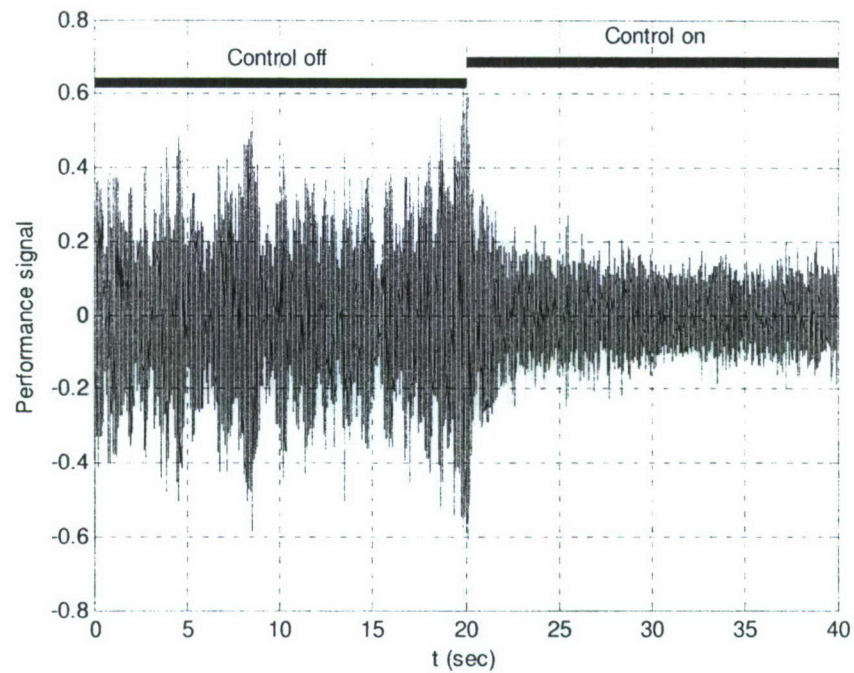
Figure 3-26.   Performance signal of the ARMARKOV disturbance rejection to band-limited white noise (0-150 Hz) with $n_c = 2$, $\mu_c = 20$ and $\Upsilon = 1$.
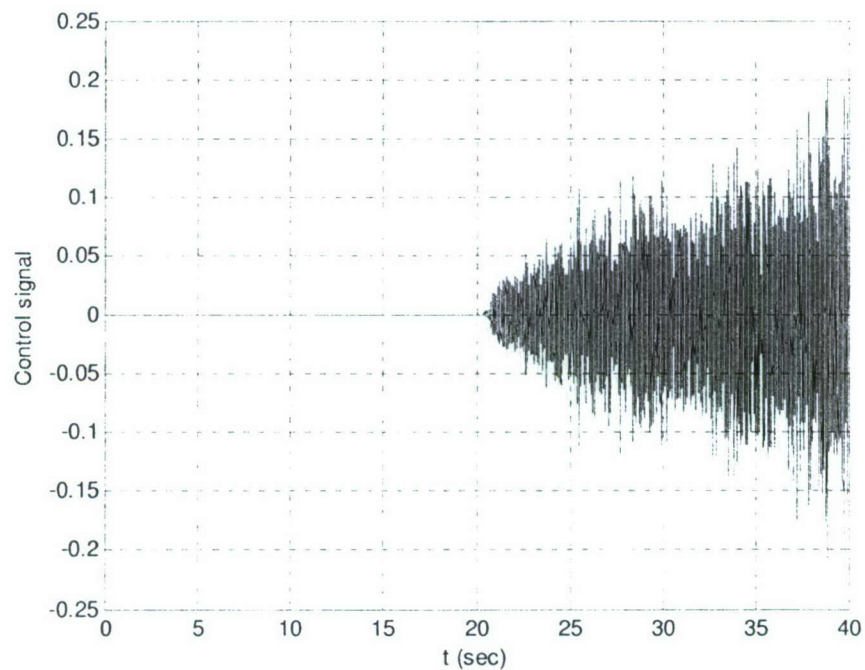
Figure 3-27.   Control signal of the ARMARKOV disturbance rejection with $n_c = 2$, $\mu_c = 20$ and $\Upsilon = 1$.
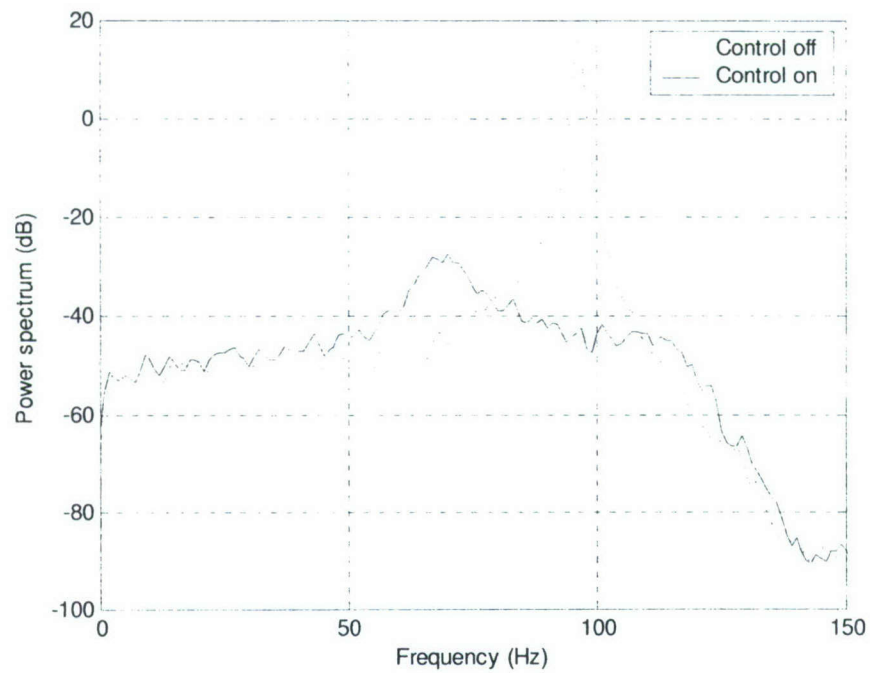
Figure 3-28.   Power spectra of the performance signals of the ARMARKOV disturbance rejection with $n_c=2$, $\mu_c=20$ and $\Upsilon=1$.
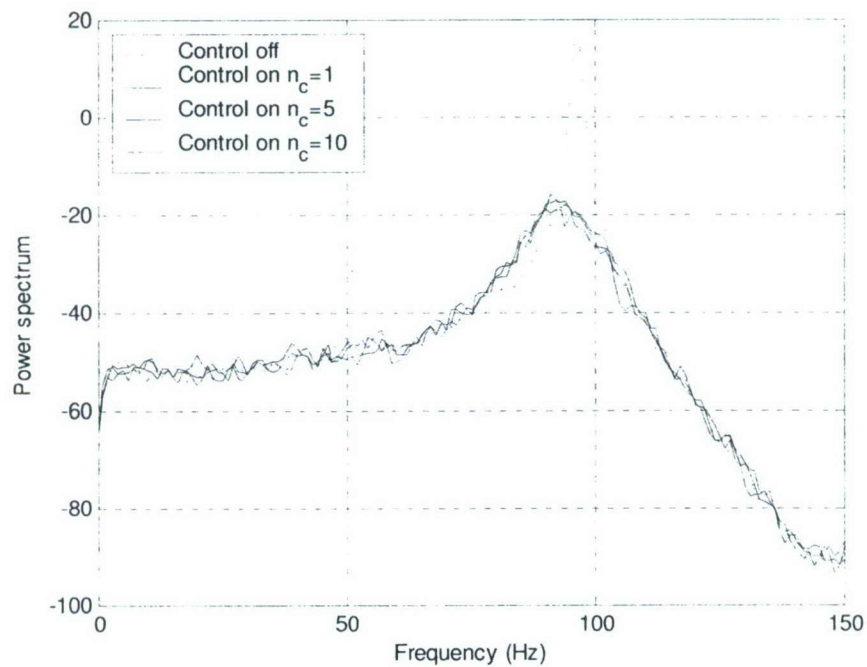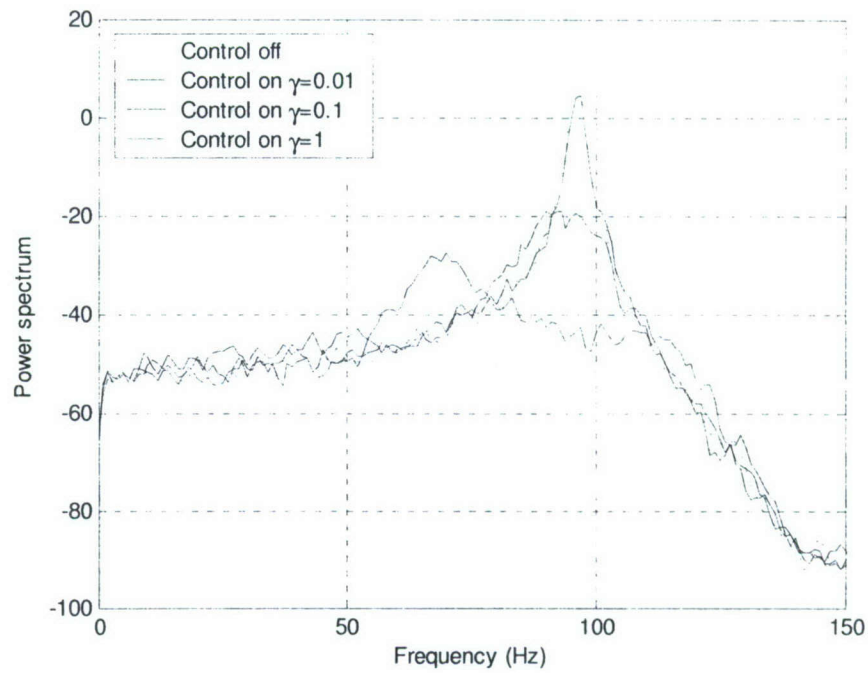

Figure 3-29.   Comparison of power spectra of the performance signals of the ARMARKOV disturbance rejection with $\Upsilon=0.1$, $\mu_c=20$ and different n_c.
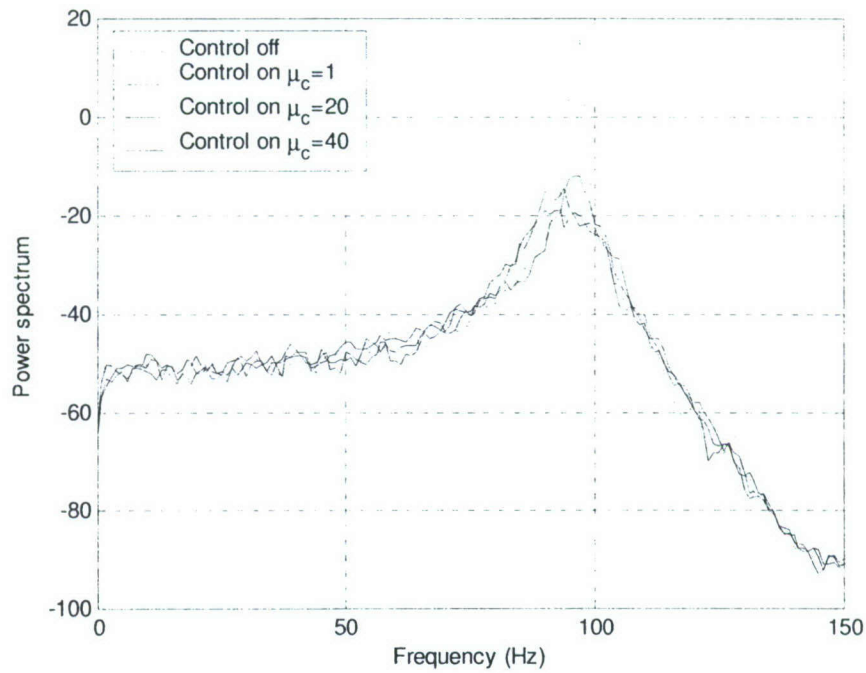
Figure 3-30. Comparison of power spectra of the performance signals of the ARMARKOV disturbance rejection with $n_c = 2$, $\Upsilon = 0.1$ and different μ_c.
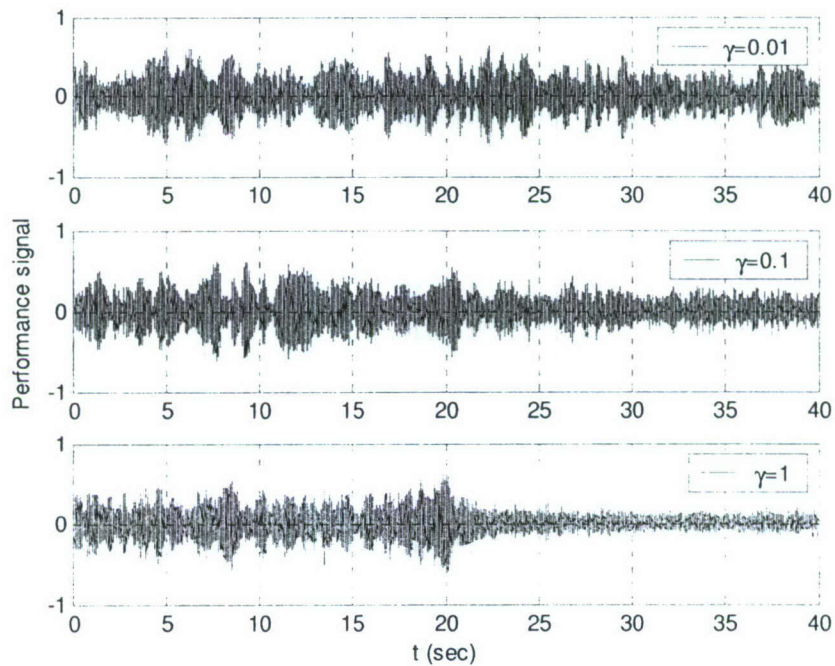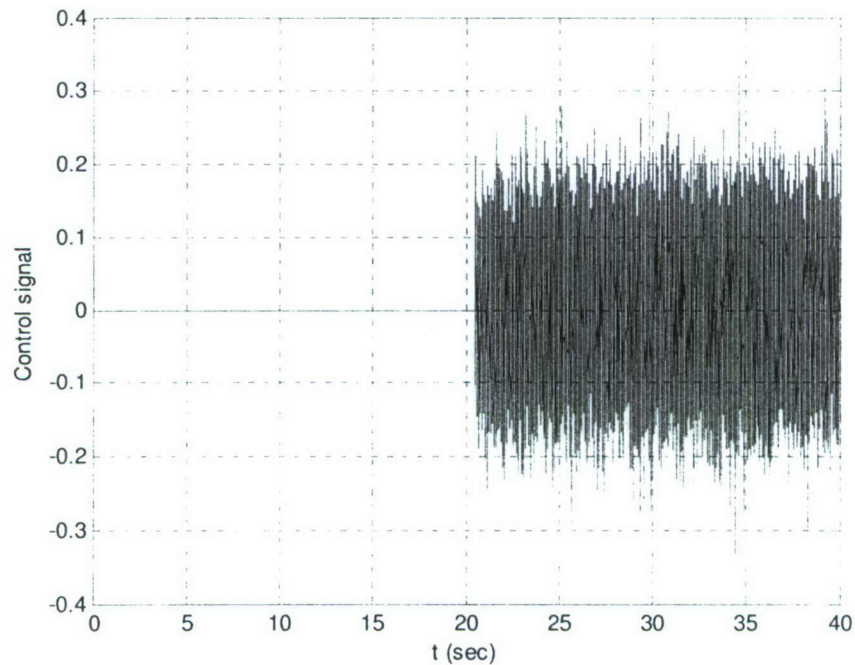

Figure 3-31. Comparison of convergence of the ARMARKOV disturbance rejection with $n_c = 2$, $\mu_c = 20$ and different Υ.

Figure 3-32. Comparison of power spectra of the performance signals of the ARMARKOV disturbance rejection with $n_c = 2$, $\mu_c = 20$ and different Υ.

Figure 3-33. Control signal of the ARMARKOV disturbance rejection at "ID and control" mode with $n_c = 2$, $\mu_c = 20$ and $\Upsilon = 0.1$.
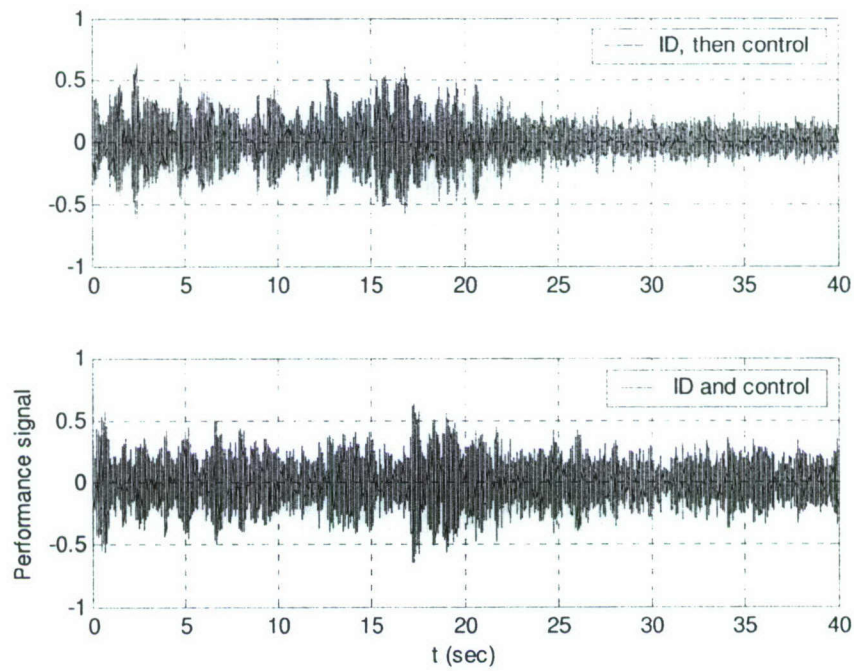
Figure 3-34. Comparison of convergence of the ARMARKOV disturbance rejection at different modes with $n_c = 2$, $\mu_c = 20$ and $\Upsilon = 0.1$.
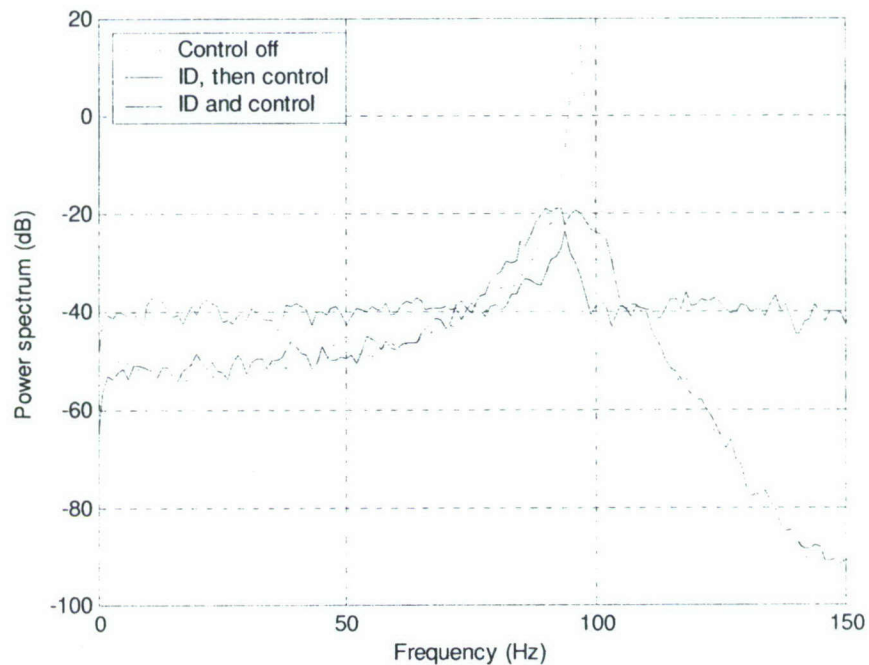

Figure 3-35. Comparison of power spectra of the performance signals of the ARMARKOV disturbance rejection at different modes with $n_c = 2$, $\mu_c = 20$ and $\Upsilon = 0.1$.

4   Experimental Setup and Data Analysis Method

The separation control experiments are conducted in an open-return low-speed wind tunnel with a 30.48 cm (1 ft) by 30.48 cm test section. The wind tunnel has two anti-turbulence screens, an aluminum honeycomb and a 9:1 contraction ratio. The airspeed is controlled by the variable frequency of the motor fan.

A two-dimensional NACA 0025 airfoil that is equipped with synthetic jet actuators, Kulite dynamic pressure transducers and a lift/drag balance is used as the test model. A Particle Image Velocimetry (PIV) system is used for flow visualization and quantitative flow field measurements. A Dantec CTA hot wire system is used to measure instantaneous velocity.

This chapter describes each part of the experimental setup in detail. A brief description of the Higher Order Statistical Analysis (HOSA) is also presented in this chapter because it may be used for nonlinear flow instability analysis.

4.1   NACA 0025 Airfoil Model

A two-dimensional NACA 0025 airfoil with chord length of 15.24 cm (6 in.) is built as a test bed for flow separation control (Figure 4-1). The span of the airfoil model is 29.21 cm (11.5 in.), which allows for a slight gap on either end to accommodate a sidewall-mounted strain-gauge sting balance. The boundary layer is tripped at the leading edge region using No. 60 sand grit. Two pairs of synthetic jets are embedded in the airfoil at approximately 3% chord and 30% chord, respectively. Six ports near the rear of the airfoil at the mid-span location are available for dynamic pressure transducers. The six ports are located at approximately 44.0%, 52.5%, 61.0%, 69.5%, 77.9% and 86.4% chord. A pre-amplifier PCB board for the dynamic pressure transducers can be also installed in the airfoil. The detailed side view of the airfoil is shown in Figure 4-1.

4.2   Synthetic Jet Actuators

The airfoil is fitted with two pairs of synthetic jet arrays (each with 0.5 mm wide slots separated by 2.4 mm), which are located in the central $1/3^{rd}$ spanwise region of the airfoil (see Figure 4-1). The first pair is located near the leading edge of the airfoil, at approximately 3% chord, while the second is placed near the point of maximum thickness at about 30% chord. The first array is fixed, while the second array can be translated between 25% chord and 37% chord. The detailed design procedures of the synthetic jet actuators that are used in this research can be found in Gallas et al. (2003) and Gallas (2005). The primary goal of the design is to maximize the magnitude of the volume flow rate through the orifice per applied voltage (i.e. $|Q_{out}/V_{ac}|$, where Q_{out} is the volume flow rate and V_{ac} is the applied ac voltage) over a frequency range of $O(kHz)$, while the size of the synthetic jet actuators are limited by the geometry of the airfoil.

As mentioned, the frequency response of the synthetic jet actuators is another important design criterion. The frequency response of the actuators must be chosen appropriately to effectively control (via amplitude and burst modulation techniques) the flow separation over a range of frequencies, ranging from the low frequency shedding in the wake to the high frequency shear layer instability. The side and top views of the synthetic jet actuators are shown in Figure 4-3. The cavity is 151 mm long, 28 mm high and 2 mm wide. Five piezoceramic disks are attached to one side of the cavity. They are driven in phase using a single amplified drive signal to achieve maximum flow rate. A thin slot (0.5 mm wide by 101.6 mm long) at the top of the cavity permits oscillatory fluid flow. Two closely spaced synthetic jets are obtained by

introducing a rigid wall to separate them, as shown in Figure 4-3. The two synthetic jet actuators are nominally identical. See the detailed characterization of the actuators in 0.

4.3 Experimental Methods

4.3.1 Flow Visualization

Flow field velocity data over the surface of the airfoil and in the wake are acquired using Particle Image Velocimetry (PIV). The PIV system consists of a pair of New Wave Minilase 15 Hz, 50 mJ per pulse, Nd:YAG lasers with appropriate light sheet optics. The width of the light sheet is approximately 1-2 mm at the plane of measurement. A TSI model 630157 Powerview Plus 2MP 10-bit CCD camera is used to acquire images. This camera contains 1600 x 1200, 7.4 μm square pixels. A series of Nikon lenses (60 mm, 75-240 mm, 200 mm) are available. The flow is seeded with water-based fog fluid by a LeMaitre G150 seeder and the seeding density is adjusted to insure uniform seeding density.

The laser pulse generator and the camera are synchronized by a TSI Model 610032 Synchronizer which is configured to acquire a pair of images using TSI INSIGHT Software version 6.1.1. The computation of the velocity field begins by dividing the image into a grid of interrogation windows overlapped in space by 50%. These windows typically range from 32 x 32 pixels to 64 x 64 pixels. The velocity is determined by the known distance that a particle is displaced during the known time dT. The INSIGHT Software utilizes an FFT cross-correlation process in conjunction with a Gaussian peak search algorithm to calculate the average velocity of the particles in the interrogation widow. A number of validation schemes are available in the software, such as range outlier rejection and median filtering.

4.3.2 Lift/Drag Balance

A strain-gauge balance is designed to measure lift and drag forces of the airfoil test bed. The detailed design procedure can be found in Griffin (2003). Two pairs of strain gauges are attached to the cantilever that supports the airfoil to measure the normal and axial forces on the airfoil, respectively (Figure 4-4). The layout of the strain gauges and Wheatstone bridge configuration are shown in Figure 4-5 and Figure 4-6. The output of the Wheatstone can be calculated by the following equation

$$V_{out} = \frac{\tilde{V} \Delta R}{R} \tag{81}$$

From the above equation, we can see that the output is linearly dependant on the change of resistance ΔR.

The output of the strain gauges is measured by a high-resolution HP34970A DAQ system and is averaged over 2 power line cycles to eliminate 60 Hz noise. The lift and drag are calculated from the normal and axial forces together with the angle of attack (Figure 4-4) via the following equations:

$$L = N\cos(AOA) - A\sin(AOA) \tag{82}$$

$$D = N\sin(AOA) + A\cos(AOA) \tag{83}$$

where L and D stand for lift and drag, respectively, while N and A stand for normal and axial force, respectively.

Before the balance can be used for the wind tunnel experiments, it is calibrated by adding known weights on the balance and measuring the output from the normal and axial strain gauges. Figure 4-7 and Figure 4-8 show typical normal and axial force calibrations vs. balance output. Very good linear relationships between the balance output and the forces on the balance are

achieved. The coefficients of the linear equations are used to back out the forces on the airfoil from the voltage output of the strain gauges.

The balance is also validated by comparing with the lift and pressure drag coefficients measured by integrating the static pressure around the airfoil. The pressure taps are located at the center span of the airfoil and the static pressure is measured via a Heise static pressure gauge. Figure 4-9 shows the static pressure distributions on the airfoil surface at different AOAs when $Re = 150,000$. From Figure 4-9, it can been identified that the flow is separated at AOA=$15°$ and $20°$. The suction zones on the upper surface shrink dramatically. This is generally referred to as pressure loss due to flow separation and is primarily responsible for deteriorating lift to drag ratio.

The lift and drag coefficients are calculated by integrating the static pressure around the airfoil surface, assuming surface friction is negligible compared with pressure forces and the flow is two-dimensional. Figure 4-10 and Figure 4-11 show the comparison of the lift and drag coefficients calculated by the two different methods at $Re = 100,000$ and $Re = 150,000$. The uncertainty was calculated at %95 confidence interval (i.e. uncertainty $= \dfrac{2\sigma}{\sqrt{N}}$, where σ is standard deviation and N is number of measurements). As shown, they agree reasonably well considering measurement uncertainties. This validates that the balance works as desired. The main reason for the differences is the three-dimensional effect as the pressure taps only measure at the center span.

4.3.3 Dynamic Pressure Transducers

To measure the pressure fluctuation on the airfoil surface, it is required that the pressure sensors must be compact so that they can be installed within the limited space in the airfoil. It is also desired that they have large enough bandwidth to capture the characteristics of the oscillations of the flow above the airfoil, and their response is linear with respect to the pressure load within the range of interest. For these reasons, a number of commercially available MEMS Kulite LQ125-5A dynamic pressure transducers (Figure 4-12) are used to obtain dynamic pressure response on the upper surface of the airfoil. The transducers can be flush mounted in the six available locations on the upper surface. A pre-amplifier/filter board for the transducers is designed to eliminate dc response ($f_{cutoff} = 1.5 \, Hz$) and amplify the outputs by a gain of 100. The pre-amplifier/filter board can be installed inside the airfoil so that the airfoil acts like an electronic enclosure. Before the transducers can be used in the experiments, they are dynamically calibrated in a 2.54 cm (1 in.) by 2.54 cm plane wave tube (PWT). A speaker was used as a source, and a Brüel & Kjær (Model 4318) microphone was used as a reference transducer. Figure 4-14 shows the linear response of a typical Kulite sensor that is obtained by fixing the frequency and increasing the input amplitude of the speaker. The frequency response is measured using a periodic chirp signal (Figure 4-14). As shown, the frequency response does not vary up to approximately 3000 Hz, which is sufficient for this research.

4.3.4 Hot Wire Anemometry

A Dantec constant-temperature hot wire anemometry system (CTA module 90C10) is used to measure time-resolved velocity in the unseparated flow above the airfoil. The CTA system includes A/D converter and all the signal conditioners needed. Before the measurements, a static calibration is performed by the calibration module and the flow unit (90H01 and 90H02). A typical calibration curve is shown in Figure 4-15. Since the output of the hot wire system usually drifts due to temperature changes, connections, etc, the calibration should be done before

each measurement. Two algorithms are commonly used for curve fitting. One is a polynomial that is used here, and the other is King's law (power law): $U = \left(\left(E^2 - A \right) / B \right)^{1/n}$, where E is the voltage output of the hot wire and U is the flow velocity (Jørgensen 1996). The difference between the temperatures at calibration and measurements should also be corrected by means of $E_{corr} = E_1 \sqrt{T_w - T_0 / T_w - T_1}$, where T_w is the wire temperature, T_0 is the temperature at calibration, E_1 is the raw wire voltage, T_1 is the temperature during measurement and E_{corr} is the corrected voltage (Jørgensen 1996). During experiments, the hot wire probe (55P11) is mounted on a 2-dimensional Velmex traversing system which has spatial resolution of about 1.6µm/step in both directions.

4.4 Control System Hardware and Software

The control systems for the separation control experiments are implemented by a dSPACE (Model DS1005) DSP system with a 466MHz PowerPC CPU. The dSPACE system has a 5-channel 16-bit A/D board (DS2001) and a 6-channel 16-bit D/A board (DS2102) as the data acquisition equipments. The range of the data acquisition boards can only be -10 to +10 V, 0 to 10 V or -5 to +5V. The control algorithms are first programmed in Matlab/Simulink and C programs (c-mex sfunction) and then compiled and downloaded to the dSPACE system. The compiled programs together with the data acquisition boards are able to run the experiments in real time. The computer is also able to acquire data into Matlab's workspace through the dSPACE system via the m-lib programs provided by the dSPACE.

4.5 Higher Order Statistical Analysis (HOSA)

Higher order spectral analysis is used to uncover the nonlinear interactions in signals or to identify nonlinear systems (Nikias and Mendel 1993). As discussed in **Error! Reference source not found.**, there are three characteristic frequencies and nonlinear interactions between them are inherent in separated flow. Unfortunately, the power spectrum alone is incapable of providing any conclusive proof of the nonlinear interactions. The power spectrum only provides proof of presence of power at certain frequencies. On the other hand, higher-order spectral method can quantify quadratic coupling between frequency pairs. For example, it can provide the information that the generation of power at a certain frequency is the result of quadratic coupling of other frequencies. The auto-bispectrum uses third order cumulants and is defined as

$$B_{xxx}\left(f_i, f_j\right) = \lim_{T \to \infty} \frac{1}{T} E\left[X\left(f_i\right)X\left(f_j\right)X^*\left(f_i + f_j\right)\right] \tag{84}$$

and the auto-bicoherence is defined as

$$b_{xxx}^2\left(f_i, f_j\right) = \frac{\left|B_{xxx}\left(f_i, f_j\right)\right|^2}{P_{xx}\left(f_i\right)P_{xx}\left(f_j\right)P_{xx}\left(f_i + f_j\right)} \tag{85}$$

where $X\left(f\right)$ denotes the Fourier transform of $x\left(t\right)$, * denotes the complex conjugate and $P_{xx}\left(f\right)$ denotes the auto-spectrum of $x\left(t\right)$.

The auto-bicoherence is bounded by zero and unity. Disturbances with frequencies f_i, f_j and $f_i + f_j$ are quadratically coupled if $b^2\left(f_i, f_j\right) = 1$, not quadratically coupled if $b^2\left(f_i, f_j\right) = 0$ and partially coupled if $0 < b^2\left(f_i, f_j\right) < 1$.

Just as the auto-spectrum has the cross-spectrum as its counterpart for signals $x(t)$ and $y(t)$, the auto-bispectrum has the cross-bispectrum as its counterpart, which is defined as:

$$B_{xxy}\left(f_i,f_j\right)=\lim_{T\to\infty}\frac{1}{T}\left[X(f_i)X(f_j)Y^*\left(f_i+f_j\right)\right]$$

(86)

Similarly, the cross-coherence is obtained by normalizing the cross-bispectrum and defined as follows:

$$b_{xxy}^2\left(f_i,f_j\right)=\frac{\left|B_{xxy}\left(f_i,f_j\right)\right|^2}{P_{xx}\left(f_i\right)P_{xx}\left(f_j\right)P_{yy}\left(f_i+f_j\right)}$$

(87)
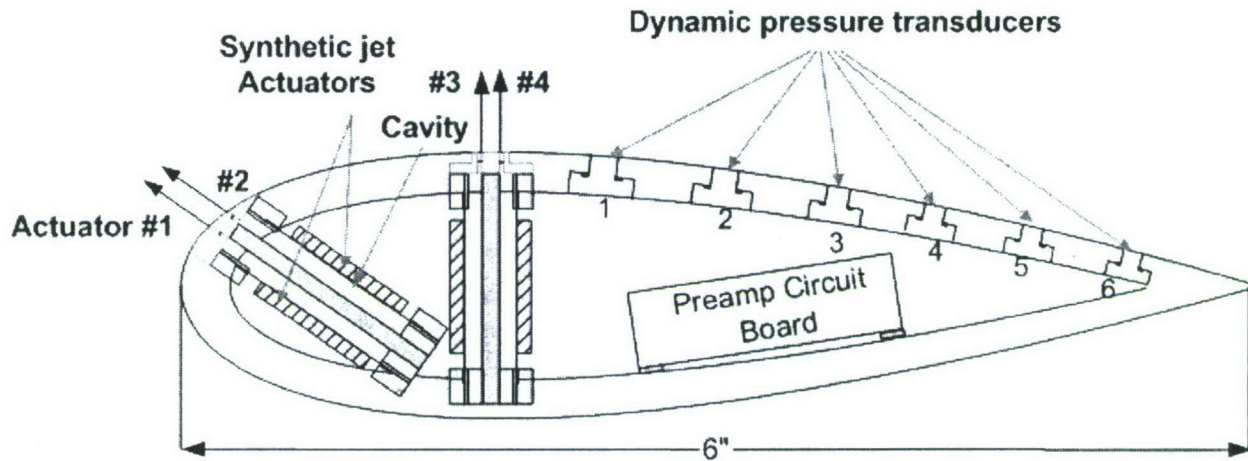
Figure 4-1.   NACA 0025 airfoil model with actuators and pressure transducers installed. (Adapted from Holman et al. 2003)
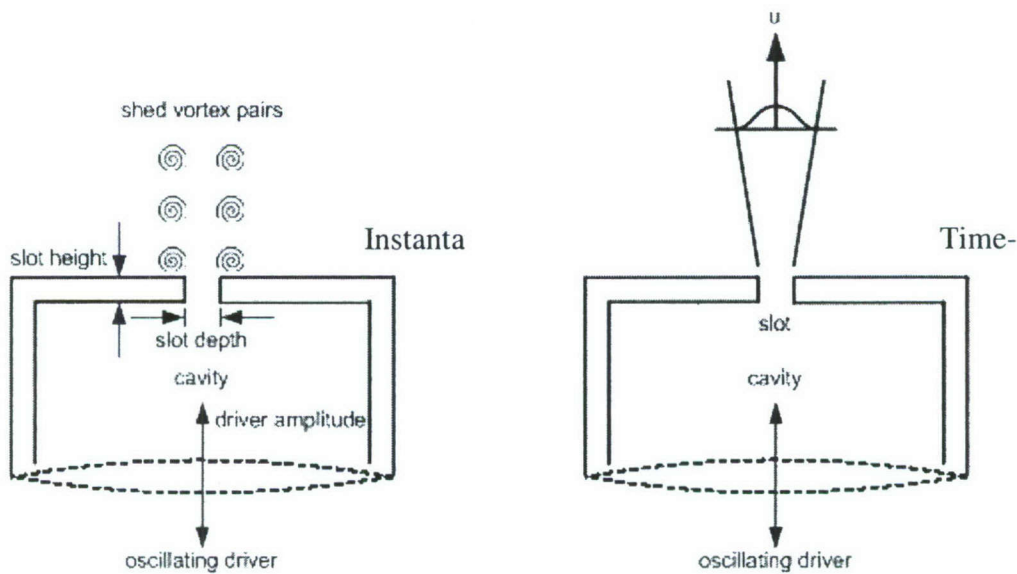
Figure 4-2. Schematic of a synthetic jet actuator.

66
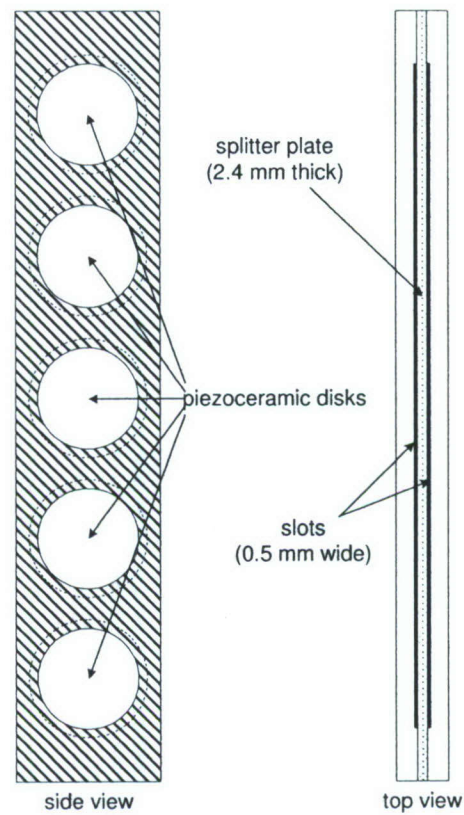
Figure 4-3. Synthetic jet array. (Adapted from Holman et al. 2003)
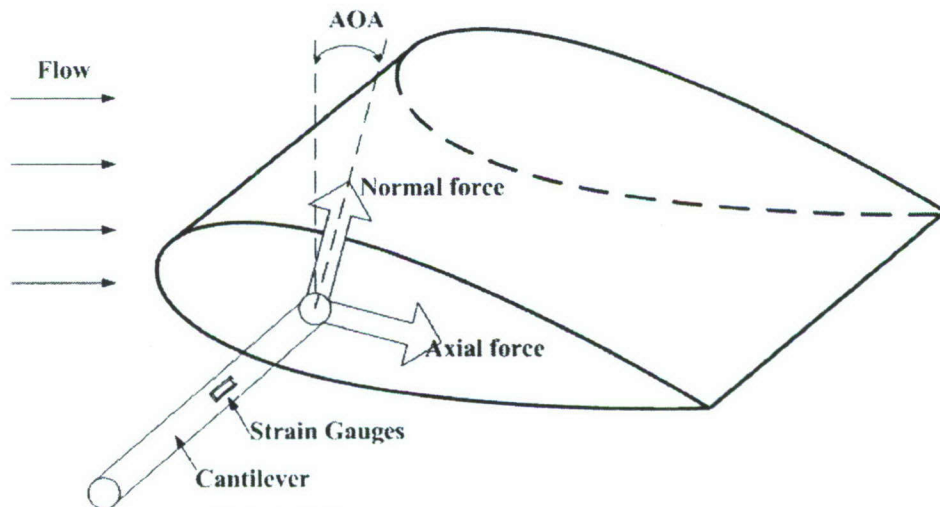
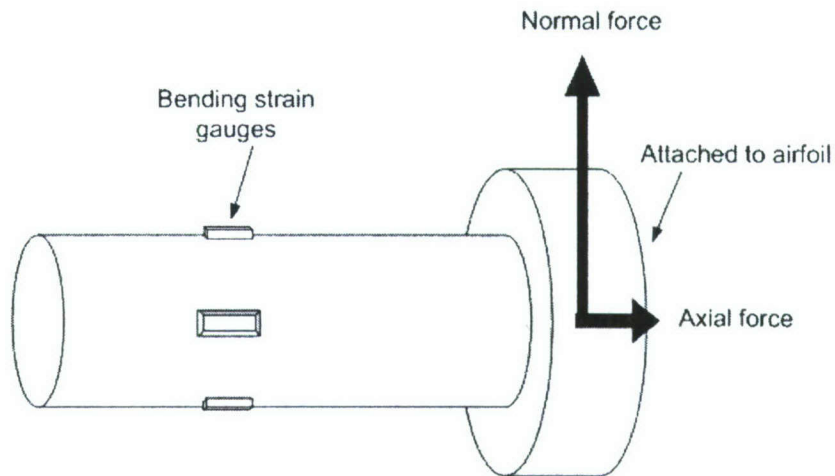Figure 4-4. Forces on NACA0025 airfoil
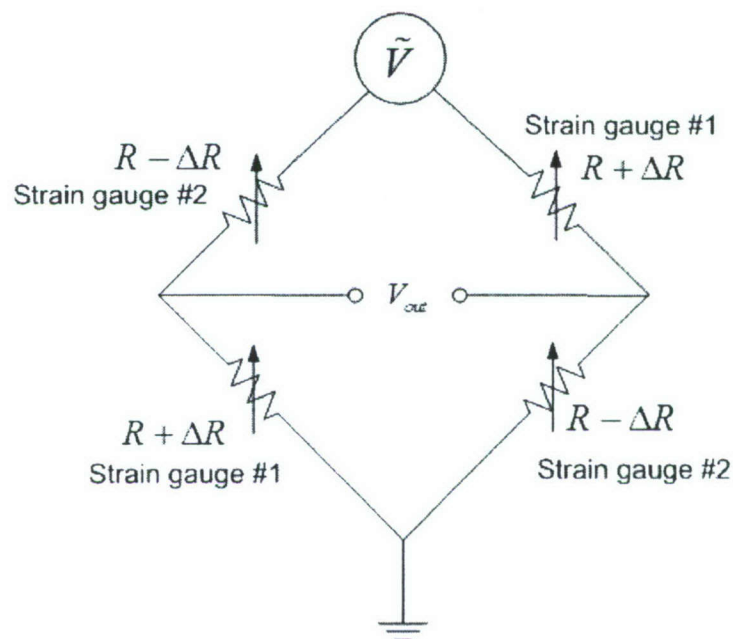
Figure 4-5. Closer view of the strain gauges.

Figure 4-6. Wheatstone bridge configuration of the balance.

Error! Objects cannot be created from editing field codes.

Figure 4-7. Normal force vs. balance output

Error! Objects cannot be created from editing field codes.
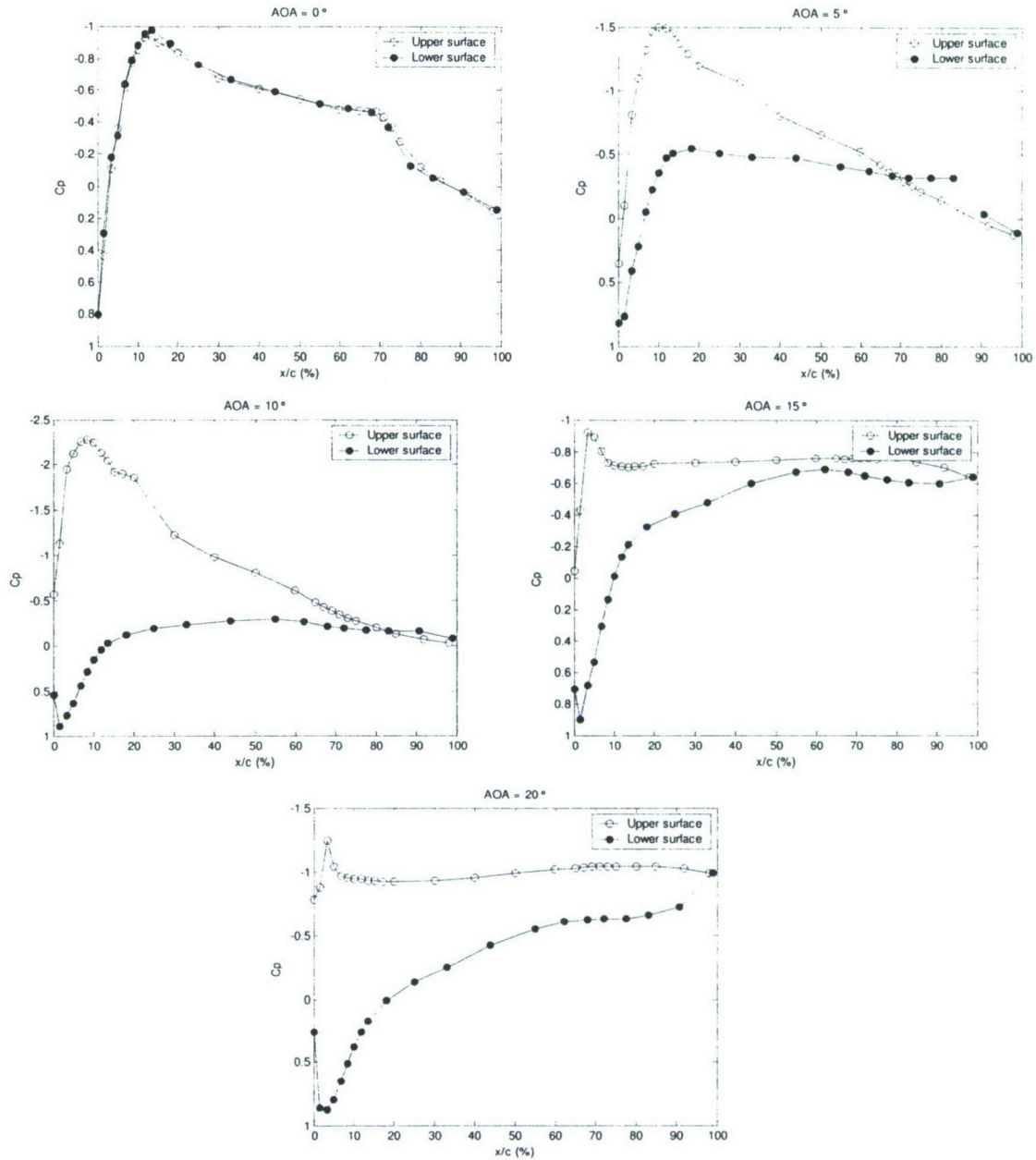
Figur   Axial force vs. balance output

Axial Force rmal

Figure 4-9. Static pressure distributions on the airfoil surface at different AOA at $Re = 150,000$.
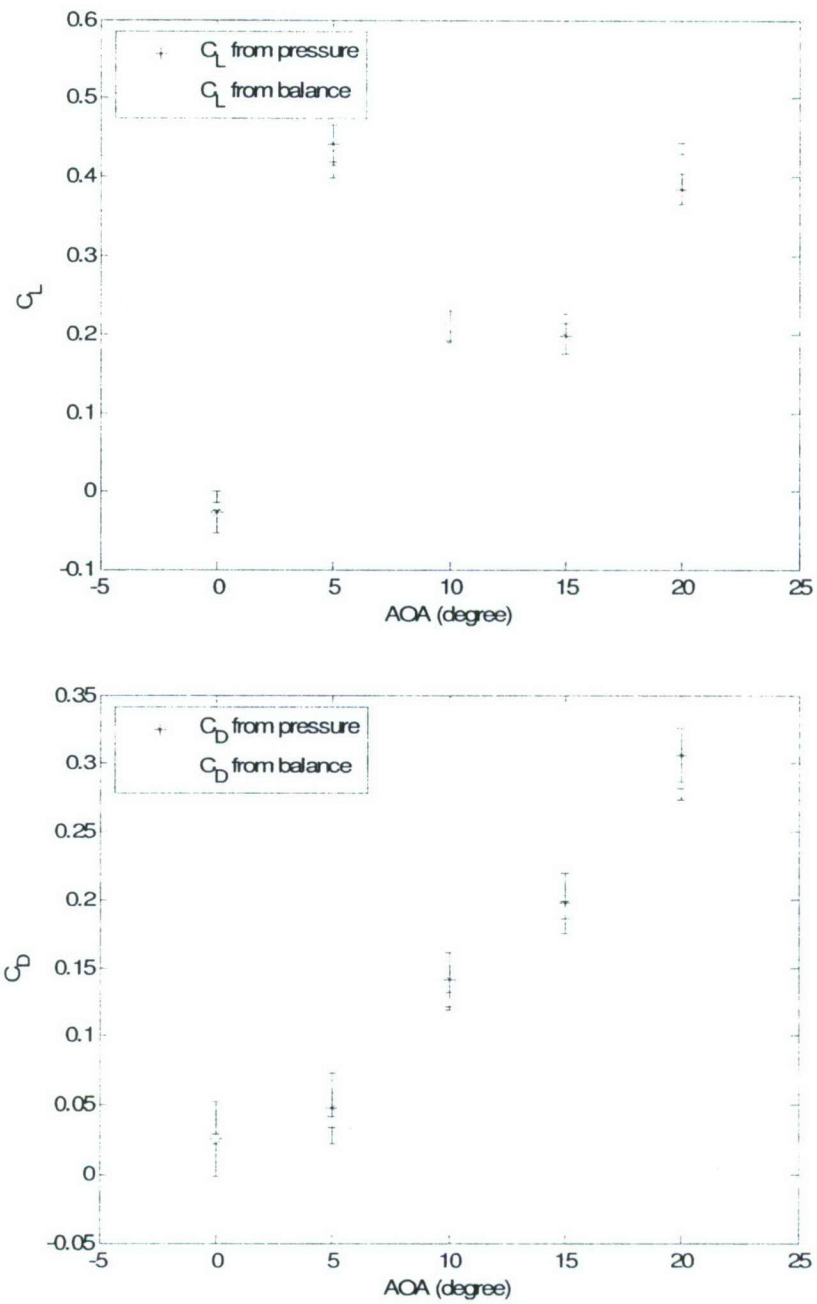
Figure 4-10. Comparison of lift and drag coefficients measured by the static pressure and the balance at $Re = 100,000$.
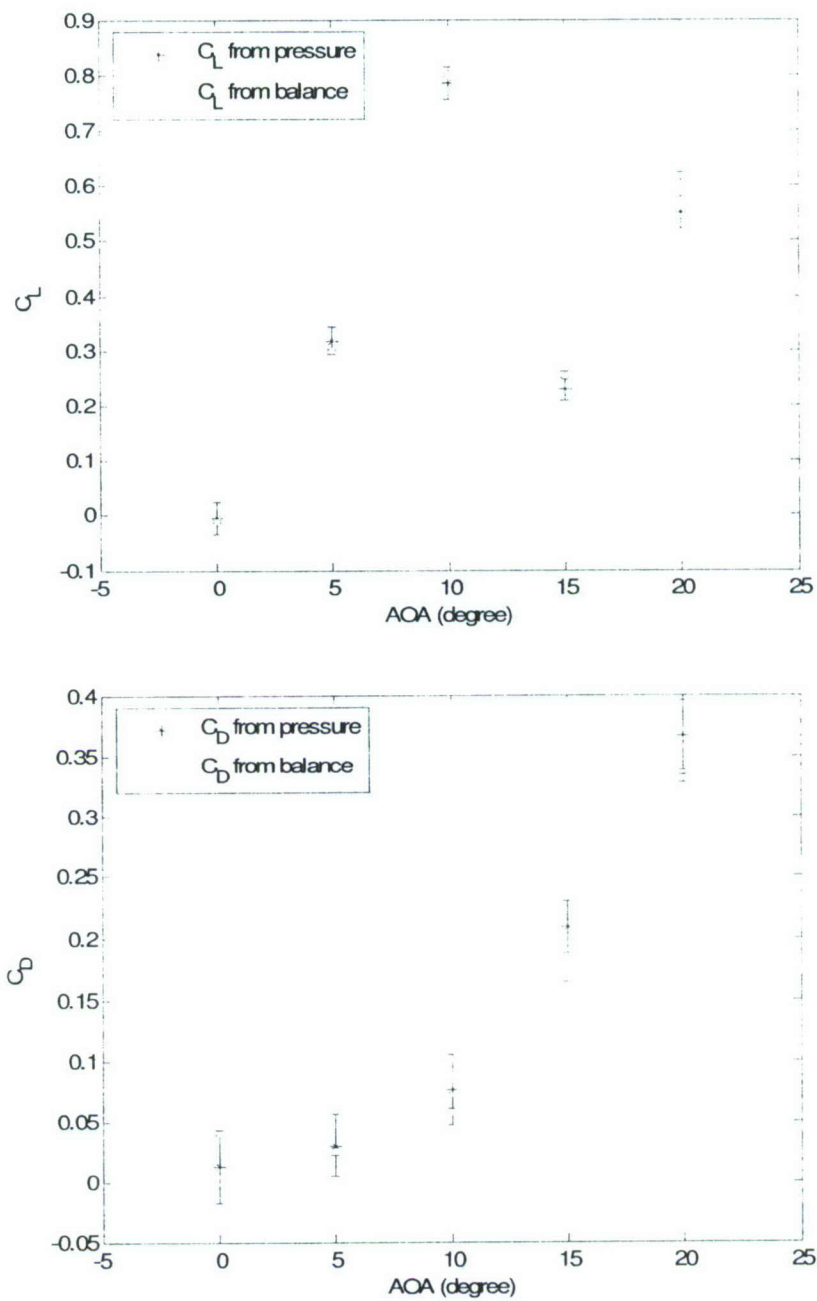
Figure 4-11. Comparison of lift and drag coefficients measured by the static pressure and the balance at $Re = 150,000$.
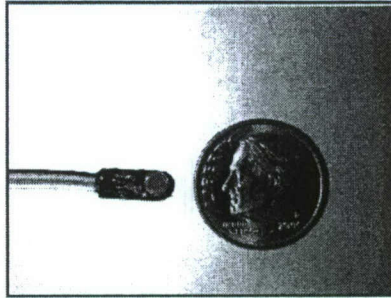
Figure 4-12. Picture of a Kulite transducer.

Error! Objects cannot be created from editing field codes.

Figure 4-13. Linear response (at 500Hz) of a typical Kulite transducer.

Error! Objects cannot be created from editing field codes.

Figure ⸱ Frequency response of a typical Kulite transducer.

Error! Objects cannot be created from editing field codes.

Figu Hot wire calibration curve.

Sensor output

Frequency

5   Results and Discussion

The experimental results of the dynamic feedback control and nonlinear control approaches are presented in two parts.

5.1   Dynamic Feedback Control

5.1.1   Experimental Configuration

Figure 5-1 shows the complete experimental configuration. The system ID and control algorithms run on the dSPACE controller system in real-time (~4 KHz). The controller generates control signal that is amplified by an amplifier. The pressure fluctuation signals measured by Kulite sensors are amplified and filtered before sending to the dSPACE controller.

5.1.2   System Identification

5.1.2.1 Coherent flow structures

Unlike POD-based approaches (Holmes et al. 1998; Tadmor et al. 2007; Ausseur et al. 2007), the unsteady surface pressure signals are used exclusive of the velocity field for feedback in this research. Although system ID and POD-based methods of modeling the flow are different, they all attempt to capture the signature of the separated flow – the coherent flow structures. In this section, we show that the surface pressure signals indeed represent the footprint of the coherent flow structures.

The following experiment is devised to show this. A continuous pulse train (repetition rate at 1 Hz and amplitude at 50 V) is fed to the actuator A1 at Re=120,000. The pressure signals are phase averaged relative to the pulse signal. Four thousand averages are taken to obtain the statistically converged pressure signal profiles. As shown in Figure 5-2, a vortex (produced by the actuator pulse) propagates downstream indicated by the surface pressure fluctuations. The vortex reaches the sensor S1 first and then S2 … S6. After the vortex passes by, the averaged surface pressure fluctuating approaches zero. This is because the random pressure fluctuations that are not correlated with the pulse input from the actuator possess random phase and are averaged out. The convective velocity is much slower than the free stream velocity, with a nominal lifetime of more than 5 airfoil chord lengths. With the link between the flow structure and the surface pressure clearly established, the goal of the system ID approach is to correlate the actuator input and the corresponding surface pressure fluctuations and utilize the relationship to model the coherent flow structure with linear dynamical equations.

5.1.2.2 Linear prediction

The control approach is based on the assumption that the coherent flow structures may be modeled by linear dynamical equations. This section demonstrates that the linear model is capable of predicting the downstream evolution of the flow dynamics (measured by the pressure sensors) subject to the actuation upstream (provided by the ZNMF actuators). In fact, previous studies in turbulent boundary layer (Rathnasingham and Breuer 2003) and cavity flows (Cattafesta et al. 1999) have suggested that linear approximations can reasonably predict inherently nonlinear flow structures.

The system ID algorithm is applied first to demonstrate this. The computational requirements are demanding for both the system ID and control algorithms. When implementing the algorithms, the algorithm parameters were chosen due to hardware limitations and were not optimized. The sampling frequency is chosen to be 4096 Hz. In Figure 5-3, z denotes the pressure signal measured by the #6 pressure sensor shown in Figure 5-1 subject to a band-limited random input provided to actuator A1. Using the input and z, one can fit a model to represent

the flow structures using the approach described in earlier sections. One should be aware that this model actually includes actuator and sensor dynamics and other hardware in the loop, e.g. amplifiers and filters. Here, **Error! Objects cannot be created from editing field codes.** in Figure 5-3 is the estimated **Error! Objects cannot be created from editing field codes.** using the model mentioned above, and the data show a reasonable match over a range of time or frequency scales. The errors are primarily due to the random turbulent structures that are uncorrelated with the actuator input, and they cannot be modeled by the system ID algorithm.

An indication of the convergence of the system ID to the actual flow model is the expected value of the Mean Squared Error (MSE), which is defined as $\text{MSE}=\text{E}\left[\left[z(k)\text{-}\hat{z}(k)\right]^2\right]$. As shown in Figure 5-4, at the beginning the MSE has a relatively large value. This is because the model parameters are initialized to zero. Then the model parameters are trained by the ARMARKOV system ID algorithm targeting the objective of minimizing the error.

5.1.2.3 Frequency response and the performance of system ID

To further evaluate the performance of system ID approach, we compare the frequency response of the flow system determined using conventional FFT methods for single-input/single-output systems described in Chapter 6 of Bendat and Piersol (2000) with that determined using the converged ARMARKOV system ID model parameters. When computing the frequency response, the parameters are f_s=4096 Hz, NFFT=1024, 75% overlap, a Hanning window and 320 effective averages.

Figure 5-5 shows that the system ID does not perfectly match the frequency response, but it does capture the essential characteristics over a broad frequency range. It is also clear that the coherence between the input and output is close to zero at frequencies less than 600 Hz, which is a characteristic of the present piezoelectric zero-net mass flux actuators, which posses a resonance near 1200 Hz (Holman et al. 2003). The low coherence renders the FFT-based frequency response estimate uncertain and highlights the difficulty of designing a control system using classical frequency domain approaches.

5.1.2.4 Acoustic contamination

In all of the discussions above, we have ignored an important potential issue related to acoustic contamination. It is well known that zero-net mass flux actuators can produce significant sound. In the present control problem, the pressure sensors are intended to capture the hydrodynamics of the coherent flow structures. However, as demonstrated by Figure 5-6, the pressure sensors do not discriminate between acoustic and hydrodynamic pressure fluctuations. Since the pressure measurements contain both components, the disturbance rejection control algorithm will try to suppress the acoustic power as well as the hydrodynamic power, possibly resulting in an undesirable reduction in the actuator amplitude. Furthermore, from a control standpoint, the acoustic and hydrodynamic paths have significantly different propagation speeds, leading to significant phase lag differences and an unstable controller.

One way to address this problem is to estimate a frequency-wavenumber spectrum using Fourier-based methods, but such a method is not amenable to a real-time control system. A second approach, adopted here, incorporates a digital filter to predict and remove the acoustic signal. We design this digital filter using the same system ID method described in the earlier section, i.e. using the system ID method to predict the acoustic signal with the actuators on and the flow off and then subtracting the computed acoustic component from the sensor measurement with both the actuators and flow on (see Figure 5-6). The ID parameters were p=1, n=100, μ=1. Note this filter has much higher order than that used in Figure 5-3. However, this

will not add significant computational intensity because after the filer is designed by the system ID algorithm the filter parameters are fixed during the closed-loop control. Figure 5-7 shows a comparison between the actual measured acoustic noise with wind tunnel off and the predicted acoustic noise by the digital filter. Good agreement is achieved. To test this digital filter further, we used the same digital filter in Figure 5-7 but reduced the actuator amplitude by 50%. Figure 5-8 shows the digital filter works well when the input signal is changed, indicating the linear behavior of the acoustic signal produced by the actuator for typical excitation levels used in the experiment.

Next, the digital filter is applied to the measurements with the wind tunnel running. Figure 5-9 shows the power spectra comparison of the pressure measurements before and after applying the digital filter for a system ID case. The power spectrum with the digital filter applied clearly shows lower power at the frequency band 500 Hz to 1500 Hz, where the piezoelectric actuator generates most of its acoustic noise due to the actuator resonance as indicated in Figure 5-6. The digital filter is thus able to mitigate the acoustic noise component and is used for all results presented below.

5.1.3   Disturbance Rejection
5.1.3.1 Closed-loop control

As described earlier, the disturbance rejection algorithm requires both reference (used for feedback) and performance signal measurements. As described earlier, the goal of the algorithm is to minimize the fluctuations of the performance signal. According to Venugopal and Bernstein (2000), the reference and performance signals can be the same. Herein, different reference and performance transducer combinations are tested for comparison. Since S1 is the closest to the leading edge and S6 is the closest to the trailing edge, it is reasonable to investigate the extremes shown in Table 5-1.

The disturbance rejection algorithm is applied to all four cases and the ID and controller parameters are summarized in

Case #	Reference transducer y	Performance transducer z	C_L	C_D	L/D
Baseline	-	-	0.21 ± 0.02	0.21 ± 0.09	1.01 ± 0.08
1	S1	S1	0.84 ± 0.01	0.12 ± 0.01	6.97 ± 0.37
2	S6	S6	0.83 ± 0.01	0.12 ± 0.01	7.21 ± 0.46
3	S1	S6	0.84 ± 0.01	0.12 ± 0.01	7.11 ± 0.40
4	S6	S1	0.84 ± 0.01	0.12 ± 0.01	7.09 ± 0.43

Table 5-2. Note that higher values increase the number of adjustable parameters in the system ID and the controller, which may increase performance. However, this is not guaranteed.

First, to make sure the control is inducing a global effect, we examine the lift/drag performance that is the aerodynamic objective of the separation control system. The control objective is to attach the separated flow and thereby reduce the fluctuating pressure spectrum associated with the convection of the vertical structures over the airfoil surface. The lift and drag are measured after the closed-loop control algorithm converges by the balance, which is only capable of providing mean or time-averaged data. The lift-to-drag ratios for all the cases are also summarized in Table 5-1 and include uncertainty estimates that account for calibration and random errors (Tian 2007). All four closed-loop control cases give similar L/D improvement, ~ 7x L/D of the uncontrolled baseline case. Note that the lift is increased while the drag is

decreased. Close inspection via tuft and smoke flow visualization reveals that, in all 4 cases, the controller is able to fully attach the separated flow. Since the four closed-loop control cases give the same L/D within experimental uncertainty, this indicates that the choice of the performance and reference sensor locations does not have a significant impact on the integrated lift/drag performance for this flow condition. In the following sections, we choose to study case #2 using S6 more closely.

5.1.3.2 Effect of control on surface pressure signals

Recall that we use the actuator and surface pressure signals to model the plant dynamics, and the disturbance rejection algorithm attempts to suppress the surface pressure spectra. Figure 5-10 shows the time traces of the performance surface pressure (measured by S6) and control input signals for case #2 before and after the control is turned on. The results clearly show that before the closed-loop control is initiated, the performance pressure signal has relatively large amplitude. After the ID and control is initiated from a zero initial condition for all parameters, the performance pressure signal starts to decrease driven by the control input from the ZNMF actuators generated by the disturbance rejection algorithm. The entire process takes approximately 79 convective time scales to learn the dynamics and optimize the controller. After a steady state is achieved, the pressure signal stays at the lower level corresponding to an attached low oscillation flow, as will be shown in the next section.

Figure 5-11 shows the comparison of the power spectra for baseline and case #2 measured by the performance transducer S6. For the closed-loop control case, the power spectra are based on the surface pressure signal after the disturbance rejection algorithm converges. The noise floor of the transducer is also plotted for comparison to verify that the pressure signals for all cases are well above the noise floor. Figure 5-11 clearly shows that the disturbance rejection algorithm is able to lower the spectrum of the surface pressure signal compared with the baseline case at all frequencies.

5.1.3.3 Quantitative flow visualization

Preliminary experimentation shows that A1 and A2 give similar results but A3 and A4 are ineffective because they are located downstream of the separation location. Thus, the results with A1 are studied closed. Normalized streamwise velocity and vorticity contours (obtained using 500 PIV image pairs) over the airfoil for the baseline and closed-loop control case #2 are shown in Figure 5-12 and Figure 5-13. For the closed-loop control case, the images are taken after the disturbance rejection algorithm converges. The actuator A1 and pressure sensors S1 – S6 are shown as circles on the airfoil surface. For the baseline case in Figure 5-12 (a), the flow separates from the leading edge just downstream of actuator A1 and all six pressure sensors are located inside the separated region. Instantaneous PIV data reveal that the separated flow features large coherent vortices sweeping over the airfoil upper surface, which results in highly unsteady pressure signals on the airfoil upper surface. The disturbance rejection algorithm "senses" the pressure fluctuations and generates actuation signals to negate the pressure fluctuations. This process ultimately organizes the unsteady flow into an attached turbulent flow in a closed-loop (smart) fashion. As shown in Figure 5-12 (b), the flow is fully attached for the closed-loop control case. This may explain why the four cases in Table 5-1 result in similar lift/drag performance, i.e. they share similar information about the flow before and after the closed-loop control is initiated.

5.1.3.4 Control input

In order to gain physical insight into the actuator control signal that the disturbance rejection algorithm generates to attach the flow, we examine the input *voltage* power as well as

the corresponding input *electrical* power to the actuator A1. The first quantity has units of V^2, while the second quantity has an SI unit of W. Note that these two quantities are different because piezoelectric actuators are capacitive devices that draw higher current as frequency is increased by virtue of the derivative operation, $i=C\,dV/dt$, where C denotes the capacitance of the piezoelectric actuators. The electrical power is calculated by multiplying the input voltage by the current of the actuator. The current is measured by a stand-alone current probe (Tektronix TCP A300).

The voltage and rms electrical power spectra are shown in Figure 5-14. The total rms electrical power sums up to 12.7 mW. It is clear from Figure 5-14 (a) that the disturbance rejection algorithm generates a broadband control input to the actuator with spectral peaks in both the low (20 Hz – 80 Hz) and the high (around 1 kHz) frequency ranges. The emphasis at low frequencies is due to the larger scale coherent flow structures described earlier, while the emphasis at higher frequencies corresponds to the smaller scale shear layer structures. More detailed discussions on the two types of flow structures can be found in Tian et al. (2006) and Wu et al. (1998). Since the flow is most receptive at these inherent frequency scales, the disturbance rejection algorithm attempts to utilize the two characteristic frequency scales by energy addition at these frequencies.

On the other hand, actuator characterization experiments reveal that the actuator produces very small output at low frequencies (< 500 Hz) (Tian et al. 2006). This is clear from Figure 5-5 and may be deduced from Figure 5-14 (b). The electrical power is concentrated at higher frequencies near the actuator resonance (than the voltage signal power) while remaining almost flat at low frequencies. This implies that although the controller attempts to control the low and high frequency instabilities associated with the wake and shear layer, respectively, the dynamic response of the actuator significantly influences the control system dynamics. It is important to recall that the "plant" includes the actuator.

Inspection of Figure 5-14 also brings into question whether the voltage power should be used as a penalty function. The electrical power may be a better choice for the penalty function since it reflects the actual power consumption by the actuator. Such questions must await future studies.

5.1.3.5 Discussion

To examine how the adaptive controller performs under different flow conditions, the angle of attack is varied continuously from 12° to 20°, with a fixed free stream Re of 120,000. The lift-to-drag ratios for the baseline and controlled cases are plotted in Figure 5-15. Clearly, the baseline flow separates starting from 12°. The adaptive controller gives the best performance at AoA=12°. The performance deteriorates as AoA increases. The improvement in lift-to-drag ratio becomes very small at AoA=20°, which means the controller is ineffective at this AoA.

The comparison of the power spectra for baseline and case #2 measured by the performance transducer S6 is shown in Figure 5-16. It is clear that unlike the 12° counterpart (shown in Figure 5-11), the power spectrum of the closed-loop control case is higher than that of the baseline case. This defeats the purpose of the closed-loop controller and therefore makes the controller ineffective. The key question is why the pressure spectral characteristics look conversely different at different AoAs. Our hypothesis is that the flow can only be partially attached at higher AoA in the mean sense. Instantaneously the partially attached flow contains highly unsteady flow vortices that cause the increase in the pressure spectra.

Possible solutions include using alternate surface sensors, such as MEMS-based direct shear stress sensors for feedback instead of pressure sensors. This can also solve the acoustic

contamination issue. However, we believe that the key limitation of the present scheme, as evidenced by its failure at higher angles of attack, include the assumption of linearity in the system identification and disturbance rejection algorithm. The nonlinearity, especially in the partially attached unsteady flow, has strong impact on the performance of the closed-loop controller.

Future improvements to the current approach include exploration of nonlinear control methods, which is the subject of the next section. By using the modulated signals as input (Tian et al. 2006), the nonlinear interactions in the unsteady flow is promoted. On the other hand, nonlinear dynamical approaches are desirable compared to the quasi-static approach in our companion study. The nonlinear system identification algorithms are demonstrated in simulations by Pillarisetti and Cattafesta (2001). Future direction includes implementing a nonlinear dynamical system identification and control scheme in the wind tunnel experiments.

5.2 Nonlinear Control

5.2.1 Experimental Configuration

As shown in Figure 5-17, dual-timing control loops are configured to implement the optimization algorithms (described in the next section). The first loop synchronously controls the actuators and measures the low-pass filtered and amplified balance signal, while the second loop averages the balance output and performs optimization in an asynchronous fashion. The second loop acts as a supervisory controller that updates the control parameters in the first loop. The sampling rate of the first loop is 40 kHz, while the second loop runs on a host PC at O(Hz). The optimization algorithm is programmed in Matlab and communicates directly with the dSPACE system to adjust the actuator signal parameters.

5.2.2 Flow Instabilities

In the present flow conditions (AoA=$20°$ and $Re_c = 120,000$), the baseline uncontrolled flow is massively separated and does not reattached before the trailing edge (i.e. post stall). As mentioned earlier, this type of post-stall flow is characterized by leading-edge shear layer rollup and vortex shedding in the wake (Wu et al. 1998). These two types of flow structures are clearly visible in the instantaneous snapshot of the flow shown in Figure 5-18. The shear layer rollup structures in the left figure have a much smaller length scale than the vortex shedding structures in the wake shown in the right figure.

To characterize the velocity fluctuations in the two flow structures, a hot-wire anemometer is used. The hot-wire is traversed vertically across the shear layer (near the separation point) and the wake vortices (1 chord aft of the trailing edge). The maximal u_{rms} location in the attached sub-regions is then determined at the two streamwise locations. Figure 5-19 shows a plot of the power spectral density (PSD) of the wake and the shear layer at the respective peak rms locations. The PSD was estimated using a 4096 point FFT, a Hanning window with 75% overlap, and 320 effective blocks. The plots zoom in on two interesting regions. The left plot clearly shows the dominant wake frequency $f_{wake} \sim 40$ Hz. The right plot shows the much higher shear layer frequency at $f_{SL} \sim 2040$ Hz. The plot also provides evidence for the nonlinear coupling between the shear layer and wake instabilities via the presence of the shear layer frequency f_{SL} and the sum/difference frequencies $f_{SL} \pm f_{wake}$. Note that f_{SL} is much higher than f_{wake} in accordance with classical scaling arguments that $f_{SL} \sim U_\infty / \theta_{sep}$ and $f_{wake} \sim U_\infty / W_{wake}$. Based on the definition $F^+ = fc/U_\infty$, $f=f_{SL}$ gives $F^+ \sim O(30)$ and $f=f_{wake}$ give $F^+ \sim O(0.6)$. This evidence supports our hypothesis that more than a single characteristic

frequency exists, perhaps explaining the wide range of effective forcing frequencies reported in the literature.

To study our hypothesis about the nonlinear quadratic coupling between the instabilities, higher-order spectral analysis of the same velocity data in Figure 5-19 is performed (Nikias and Petropulu 1993). The auto-bicoherence contour plot shown in Figure 5-20 is bound between 0 and 1 and is only nonzero due to nonlinear quadratic phase coupling (lock-on). The auto-bicoherence thus quantifies the fraction of power in a random signal as a function of triad between two frequency components f_1, f_2 and their sum or difference $f_1 \pm f_2$. A close inspection of the contour plot reveals distinct features at $f_2 = f_w$ (in particular near $f_{SL}/2, f_{SL}, 1.5 f_{SL}$), $f_2 = f_{SL}$ and $f_2 = f_{SL} - f_w$ (in particular between f_{SL} and $1.5 f_{SL}$), and especially along the lines $f_1 + f_2 = f_{SL}$ and $f_1 + f_2 = f_{SL} - f_w$. These data conclusively show the presence of nonlinear quadratic coupling between the Kelvin-Helmholtz and wake instabilities.

5.2.3 Actuator Calibration
5.2.3.1 Frequency response

ZNMF actuator dynamics is a critical issue for the control of a separated flow. A typical ZNMF device contains a cavity and a vibrating diaphragm to drive oscillatory flow through a small orifice on the cavity. The synthetic jet represents a coupled electro-mechanical-acoustic system with frequency dependent properties determined by device dimensions and material properties (Gallas et al. 2003). Gallas et al. use the lumped element modeling approach to model these actuators. In this research, although modeling our ZNMF devices is not needed, we do need to characterize the frequency response of the actuator A1 (that is used in this research). Since the ZNMF actuator is an inherently nonlinear device, the traditional approach that uses a swept sine as an input signal is not appropriate. Instead, a single sine wave is used as input, and the anemometer signal is recorded. The frequency is then increased in a loop, while the forcing amplitude is held constant. Figure 5-21 shows the rms velocity per input voltage in the frequency band from 500 Hz to 2500 Hz. Three different input levels are used. The peak output occurs at approximately 1200 Hz, and significant output is apparently limited to a bandwidth of 500-1500 Hz. The output level is very low for frequencies less than 500 Hz and larger than 1500 Hz. This precludes the possibility of directly forcing either the low-frequency (~40 Hz) wake or high frequency (~2020 Hz) shear layer instabilities via sinusoidal excitation. It also highlights the preferential output of the actuator near its resonance frequency. Furthermore, the nonlinear nature of the actuators is revealed, since the frequency response function is not independent of the input voltage. (If the actuator were linear, these curves would collapse.) However, that is this nonlinear behavior that is leveraged to enable forcing at low and high frequencies, as explained below.

5.2.3.2 Types of actuation waveforms

Three typical multi-modal waveforms are studied to take advantage of the multiple instabilities of a separated flow. They are shown in Figure 5-22: (a) amplitude, (b) burst and (c) pulse modulation. In (a) and (b), the lower plot in the figure is the result of a point-by-point product of the top two waveforms. Such forcing is, in general, a modulation of a (usually) high frequency carrier signal, (e.g., a sine wave with frequency f_c) by a low frequency modulation signal (either a sine wave or square pulse with frequency f_m). In addition, a parameter A is multiplied to determine the amplitude. For the BM signal, there is an additional parameter, the duty cycle, which determines how many sine wave periods occur in each burst. In this research, the duty cycle is adjusted such that only one period occurs in each burst. The last case in part (c)

is a pulse train, which can be interpreted as the modulation of a constant signal by square pulse. Similar to the BM signal, the duty cycle can be an additional parameter. In this research, it is kept to be the shortest achievable width on the dSPACE control, i.e. one discrete sample Δt. In this case, there is only one waveform parameter f_m to vary. As one moves from amplitude to burst to pulse modulation, the modulation process results in an increasingly rich signal spectrum with broader spectral content, which improves the likelihood that the excitation waveform will excite an inherent instability. Furthermore, the required actuator power reduces as will be shown in the following section.

Next we study the output of the actuator subject to the AM waveform excitation as an example. Figure 5-23 shows the velocity output of the ZNMF actuator A1 measured by the hot-wire anemometry subject to an AM excitation, where $A=50$ V_{pp} (peak-to-peak voltage), $f_m=50$ Hz and $f_c=1180$ Hz. The wire was placed at a sufficient distance (~1mm) above the actuator slot so that there is no reverse flow occurs and, hence, no signal rectification is needed. The temporal record shown in (a) clearly shows the low frequency oscillations at 50 Hz and the high frequency oscillations at 1180 Hz. The corresponding power spectral density of the velocity signal shown in (b) reveals that the high power is at the low modulation frequency 50 Hz while the second highest power is at the high carrier frequency, with additional harmonic distortion peaks. Recall that the response to the sinusoidal excitation at frequencies less than 500 Hz is very low, as shown in Figure 5-21. The modulation enables the actuator to generate high power signals at low frequencies, while the sinusoidal response is limited by the actuator dynamics. This allows an actuator operating at or near its resonant frequency via a carrier signal at f_c to generate significant disturbances at characteristic frequencies of the flow that are far from the natural frequency of the device. This characteristic is attributed to the nonlinear nature of the actuator system. Similar behavior is observed for BM and PM.

5.2.3.3 C_μ and electrical power calibration

Figure 5-21 showed that the actuator u_{rms} response varies significantly with actuation frequency when subjected to sinusoidal excitation. This is typical for a ZNMF actuator. When the performance of separation control is studied, the actuation frequency is always of prime importance. However, when the actuation frequency is varied, the actuator response is also varied even for constant amplitude. As mentioned earlier, it has been shown that sinusoidal authority varies monotonically with V_J/U_∞ up to some maximum value (Seifert et al. 1993, 1996, 1999; Glezer and Amitay 2002; Mittal and Rampunggoon 2002). In other words, when the actuation frequency is varied, the two performance-determining parameters (namely frequency and amplitude) are varied simultaneously. Unfortunately, this can lead to misleading results. For example, one may find that the performance is the best at the peak response frequency of the actuator, which could be simply because the actuator is providing higher output as opposed to the flow being more receptive as that frequency.

The same problem above still exists even when multi-modal waveforms are used; the actuator response varies when A, f_m and f_c are varied. To separate amplitude forcing effects, the following calibration is performed. For the AM and BM signals, a two-dimensional grid in the (f_m, f_c) space is generated, and C_μ and rms electrical power consumed by the actuator are measured for various excitation amplitudes. This time-consuming task takes days to complete and verify repeatability. The results are shown in Figure 5-24 and Figure 5-25. The profiles for five amplitudes (30 V_{pp}, 35 V_{pp}, 40 V_{pp}, 45 V_{pp} and 50 V_{pp}) are recorded and shown. The lowest

profile is for the 30 V_{pp} case and the highest profile is for the 50 V_{pp} case. For the PM signal, there is only one frequency parameter f_m; thus a contour plot in the (A, f_m) space is shown in Figure 5-26. The amplitudes are again 30 V_{pp} to 50 V_{pp} with 5 V_{pp} increment.

There are several important observations in the results. For the AM signal, the response (C_μ and electrical power) is approximately independent of the modulation frequency f_m but strongly dependent on f_c. The C_μ at a fixed f_m is similar to the sinusoidal velocity response shown in Figure 5-21. In addition, the shape of the electrical power surfaces are somewhat different than the shapes of the C_μ, and the peak frequencies are different too. This means that when the actuator provides the maximum velocity output, the electrical power consumption is not maximized.

For the BM signal, the C_μ and electrical power responses are dependent on both f_m and f_c. They monotonically increase with f_m as expected. As with the AM signal, the shapes of the C_μ and electrical power surfaces are different and possess different peak frequencies. The profiles are simpler for the PM signal since there is only one frequency parameter. Both the C_μ and electrical power responses increase with f_m and A as expected. Furthermore, typical levels of C_μ are 10^{-4}, 10^{-5} and 10^{-6} for the AM, BM and PM signals, respectively.

With this information on C_μ and electrical power, additional constraint functionality is added to the adaptive optimization program to hold C_μ or electrical power constant, while f_m and f_c are varied. This is done by adjusting A in accordance with Figure 5-24, Figure 5-25 and Figure 5-26 in each iteration of the optimization algorithm. Thus, it is possible that at certain (f_m, f_c) combinations, constant C_μ or electrical power cannot be achieved. In this case, f_m and f_c are set to the values at the boundary such that the momentum or power constraint is maintained. This will hopefully become clearer when the optimization results are discussed in the next section.

5.2.4 Adaptive Control Results

First, the constrained optimization is carried out at AoA=12° and Re=120,000. At this AoA, the dynamic control approach in our companion study works well. The constraint is set at $C_\mu = 7.15 \times 10^{-6}$. This is a relatively low level, which can be achieved in most portions of the (f_m, f_c) space for the AM and BM signals and all values of f_m for the PM signal. To protect the actuator from physical damage, the maximum amplitude is limited to 50 V_{pp}. The results are summarized in

Table 5-3. The lift-to-drag ratios are comparable with the results using the dynamic control approach (within uncertainties). This is not surprising because the flow is completely attached by both approaches at AoA=12°.

On the other hand, when the AoA is 20° where the dynamic control approach fails to attach the flow, the present nonlinear control shows its clear performance improvement. Therefore, a more detailed study is performed at this AoA.

In addition to the constrained cases for $C_\mu = 7.15 \times 10^{-6}$, the constrained optimization is also carried out with constant electrical power of 0.0005 W. The constrained optimization results are summarized in Table 5-4. Typical search paths are plotted in Figure 5-27 to Figure 5-29. The shaded areas in Figure 5-27 and Figure 5-28 denote the achievable parameter space, inside which the optimization is constrained. It is clear that the achievable areas cover most of the parameter space for the AM cases while limited space for the BM cases. Since there are two parameters: f_m and f_c, three initial points are needed in each optimization run as mentioned in earlier sections. The symbols ▲, ■, ● denote the search paths following each initial point during the optimization. On the other hand, for the PM signal, only two initial points are needed. Different sets of initial points are chosen to cover most of the operational space to achieve a global optimum.

In Table 5-4, the first column indicates if the constraint is active in the optimization process. The last three columns summarize the optimal values for converged results. The experimental uncertainties are also added to the L/D values. By simply observing the L/D values, we find that the performance for the AM case (a) gives the best performance. The AM and BM signal are superior to the PM signal with constant $C_\mu = 7.15 \times 10^{-6}$. For the AM and BM cases (a), note that the converged f_c is near the shear layer frequency f_{SL}. On the other hand, the modulation frequency f_m assumes a value near the wake frequency f_{wake} and its superharmonics. Most importantly, effective separation control is achieved by using the multimodal waveforms with C_μ of at least an order-of-magnitude smaller than typical values reported in the literature (Table 2 in Greenblatt and Wygnanski 2000). Selected sinusoidal excitations are also tested on our airfoil model to compare with the results using the multimodal waveforms. The voltage amplitude for these tests is held at 50 Vpp. The results are summarized in

Table 5-5. It is clear that sinusoidal control (even with higher C_μ) gives poorer performance than the AM and BM excitations.

In addition, except the PM signal, the nonlinear control is able to achieve much better performance than the dynamic control in our companion study at AoA=20°. The nonlinear control approach benefits from the nonlinear coupling of the instabilities and the integrated performance (L/D) measurements instead of local unsteady pressure measurements.

Table 5-1. Case descriptions and performance for disturbance rejection experiments. (AoA=12° and Re=120,000)

Case #	Reference transducer y	Performance transducer z	C_L	C_D	L/D
Baseline	-	-	0.21 ± 0.02	0.21 ± 0.09	1.01 ± 0.08
1	S1	S1	0.84 ± 0.01	0.12 ± 0.01	6.97 ± 0.37

2	S6	S6	0.83 ± 0.01	0.12 ± 0.01	7.21 ± 0.46
3	S1	S6	0.84 ± 0.01	0.12 ± 0.01	7.11 ± 0.40
4	S6	S1	0.84 ± 0.01	0.12 ± 0.01	7.09 ± 0.43

Table 5-2. Summary of parameters in disturbance rejection algorithm.

p	n	μ	p_c	n_c	μ_c
1	2	10	p+n+μ-1	2	20

Table 5-3. Constrained optimization results using the AM, BM and PM signals. (Baseline L/D=1.01 at AoA=12° and Re=120,000)

Signal type	Constraint	Constraint Active?	Converged f_m	Converged f_c	Converged L/D
AM	$C_\mu = 7.15 \times 10^{-6}$	No	74	1667	7.47 ± 0.45
BM	$C_\mu = 7.15 \times 10^{-6}$	Yes	48	1305	7.63 ± 0.36
PM	$C_\mu = 7.15 \times 10^{-6}$	No	16	NA	7.14 ± 0.25

Table 5-4. Constrained optimization results using the AM, BM and PM signals. (Baseline L/D=1.1 at AoA=20° and Re=120,000)

Signal type	Constraint	Constraint Active?	Converged f_m	Converged f_c	Converged L/D
AM: Case (a)	$C_\mu = 7.15 \times 10^{-6}$	Yes	61	2405	2.18 ± 0.07
AM : Case (b)	Power=0.0005	No	202	1005	1.77 ± 0.05
BM : Case (a)	$C_\mu = 7.15 \times 10^{-6}$	Yes	55	1979	1.95 ± 0.05
BM : Case (b)	Power=0.0005	Yes	56	1318	1.52 ± 0.04
PM : Case (a)	$C_\mu = 7.15 \times 10^{-6}$	No	16	NA	1.49 ± 0.04

PM : Case (b)	Power=0.005	No	29	NA	1.48 ± 0.04

Table 5-5. Results using sinusoidal excitations.

$F^+ = fL_{sep}/U_\yen$	C_μ	L/D
0.5	~0	1.14 ± 0.02
15	3.16×10^{-4}	1.76 ± 0.03
26	7.79×10^{-6}	1.77 ± 0.03
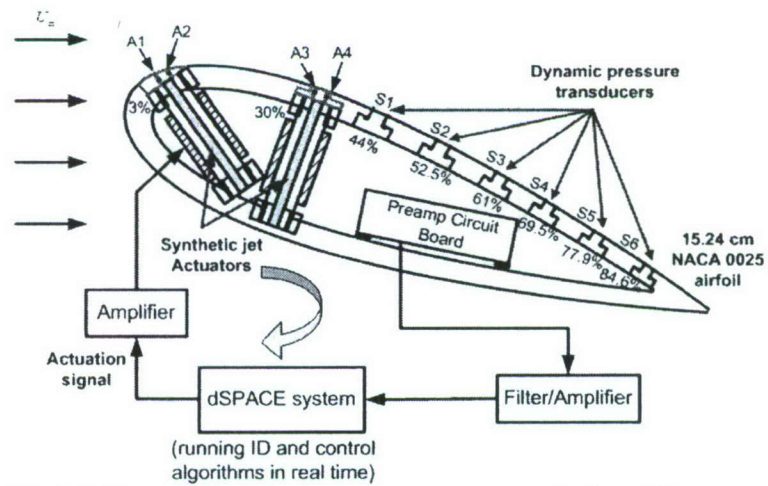
Figure 5-1. NACA 0025 airfoil model with actuators, sensors and closed-loop control system.
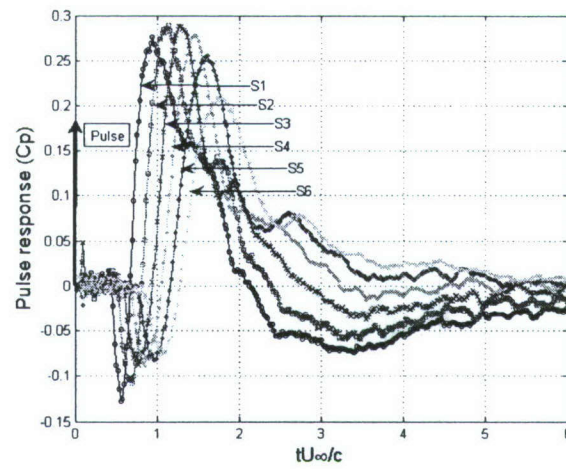
Figure 5-2. Phase averaged pulse response measured by six pressure sensors. The slow propagation velocity of the coherent flow structures is clearly visible.

85
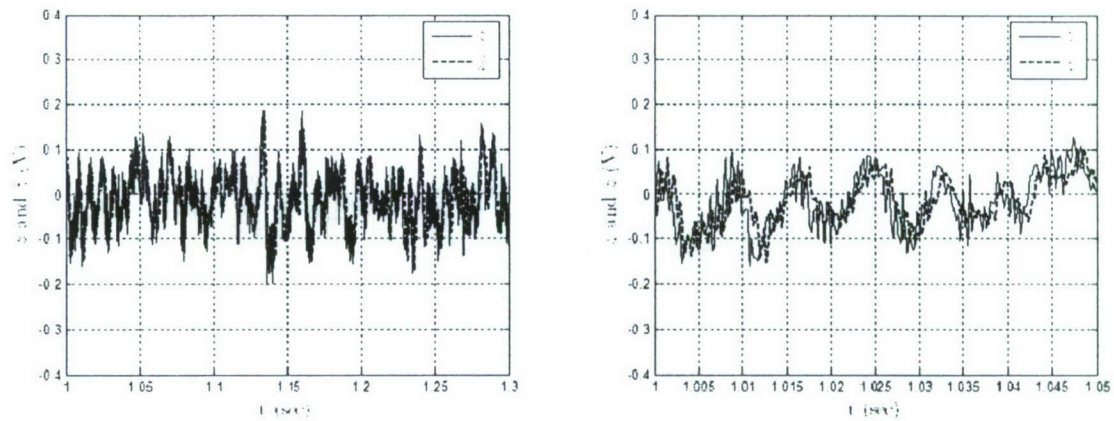
Figure 5-3. Comparison between measured signal from the pressure sensor (#6 in Figure 5-1) and the fitted output by ARMARKOV system ID algorithm for long and short time intervals. Results show a reasonable match at low frequencies between measured and fitted outputs. For ARMARKOV ID: p=1, n=2, **Error! Objects cannot be created from editing field codes.**=10.
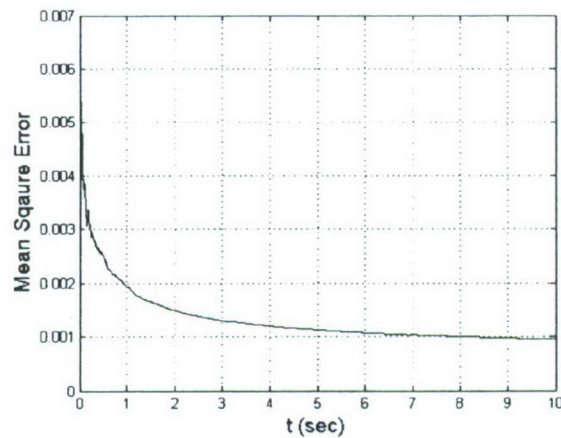
Figure 5-4. Mean Squared Error (Running MSE) between measured and fitted outputs. Results show that the ARMARKOV ID algorithm converges, i.e. error being minimized.
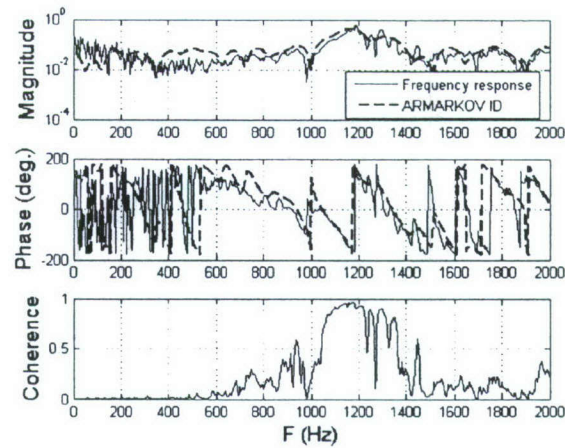
Figure 5-5. Comparison between frequency response (FR) and fitted response by ARMARKOV ID algorithm. Parameters for FR: **Error! Objects cannot be created from editing field codes.**=4096 Hz, NFFT=1024, 75% overlap and Hanning window. For ARMARKOV system ID: p=1, n=2, **Error! Objects cannot be created from editing field codes.**=10.
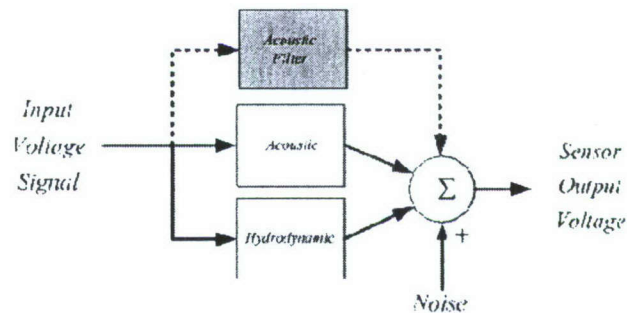
Figure 5-6. Dual signal paths from the actuator to the pressure sensor (acoustic and hydrodynamic). A digital filter is introduced to remove the acoustic component by turning off the flow to isolate the acoustic path.
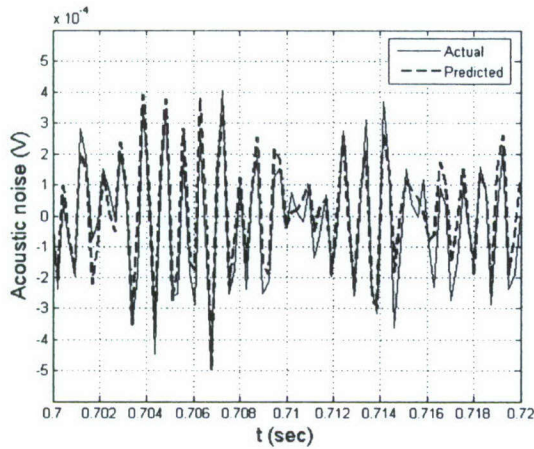
Figure 5-7. Actual measured and predicted acoustic noise using a band-limited random signal to the actuator.
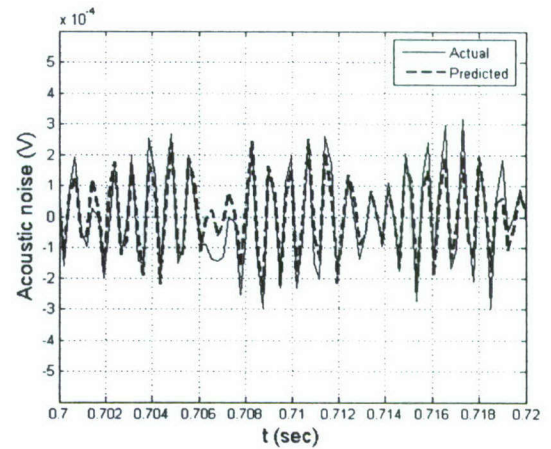
Figure 5-8. Actual measured and predicted acoustic noise using the same filter as in Figure 5-7 but with one half of the input amplitude.
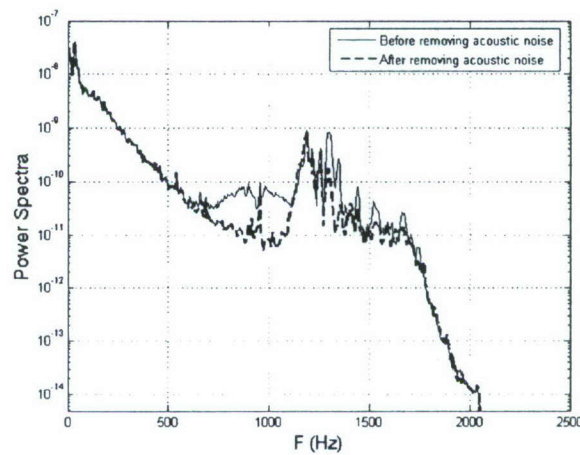
Figure 5-9. Power spectra of the sensor signals (with wind tunnel running) before and after applying acoustic filter.
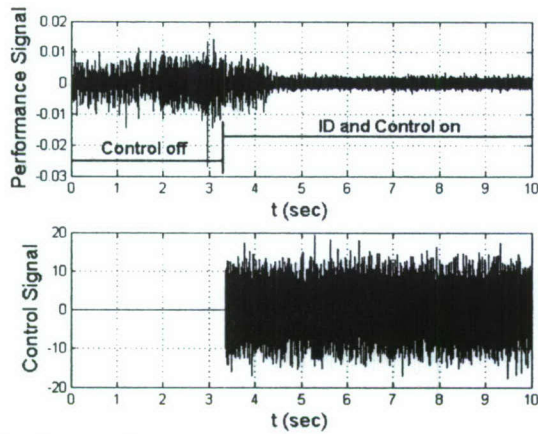
Figure 5-10. Performance surface pressure (S1) and control input signals (in Volt) before and after the ID and control is initiated for case #2. Control is established within 1 second or <100 convective time scales.
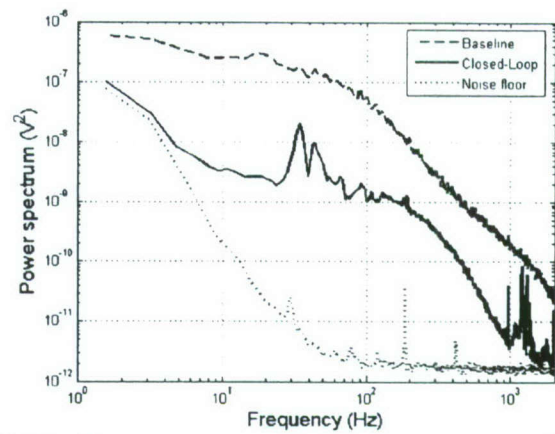
Figure 5-11. Power spectra of the pressure transducer output for the baseline and the closed-loop control cases measured by S6 (performance).
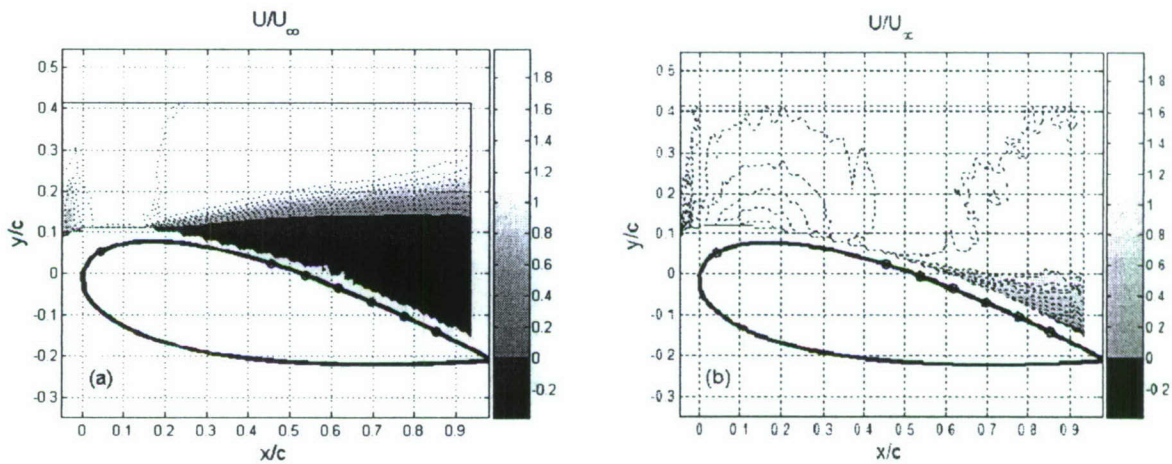

Figure 5-12. Contours of streamwise velocity **Error! Objects cannot be created from editing field codes.** for (a) baseline and (b) closed-loop control case #2 at AoA = 12° and Rec=120,000.
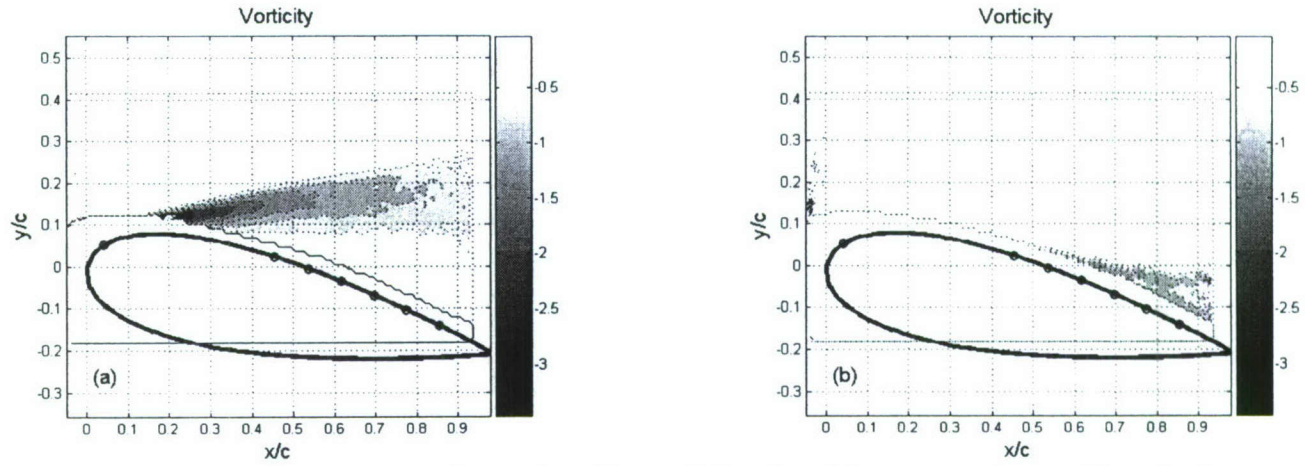
Figure 5-13. Contours of vorticity for (a) baseline and (b) closed-loop control case #2 at AoA = 12° and Rec=120,000.
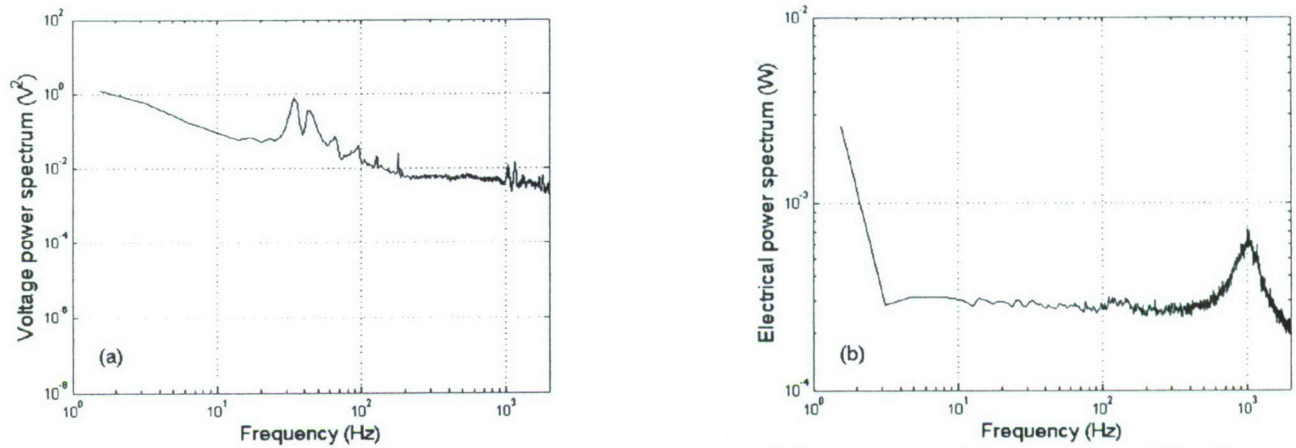
Figure 5-14. (a) Voltage and (b) electrical power spectra of the actuator A1 input signal for the closed-loop control case.
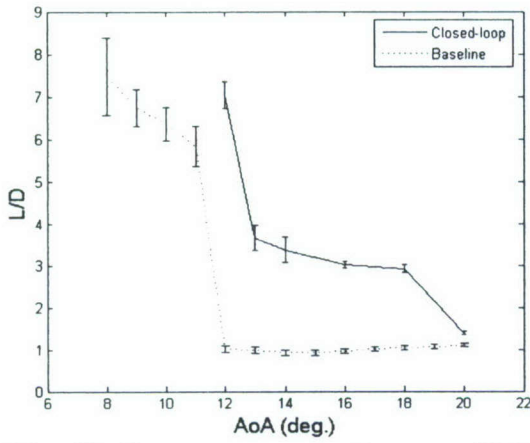
Figure 5-15. Performance comparison at different AoA.
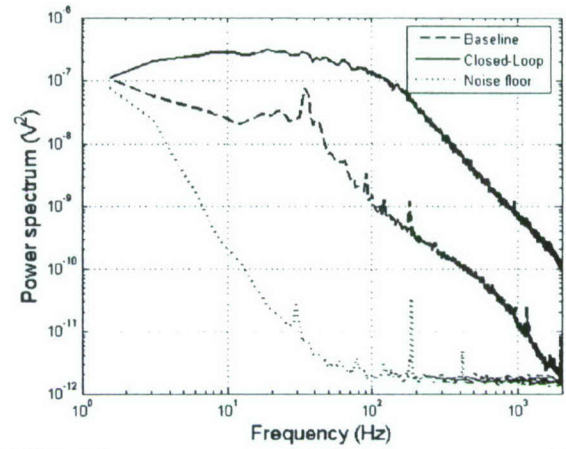
Figure 5-16. Power spectra of the pressure transducer output for the baseline and the closed-loop control cases measured by S6 (performance) at AoA = 20° and Rec=120,000.
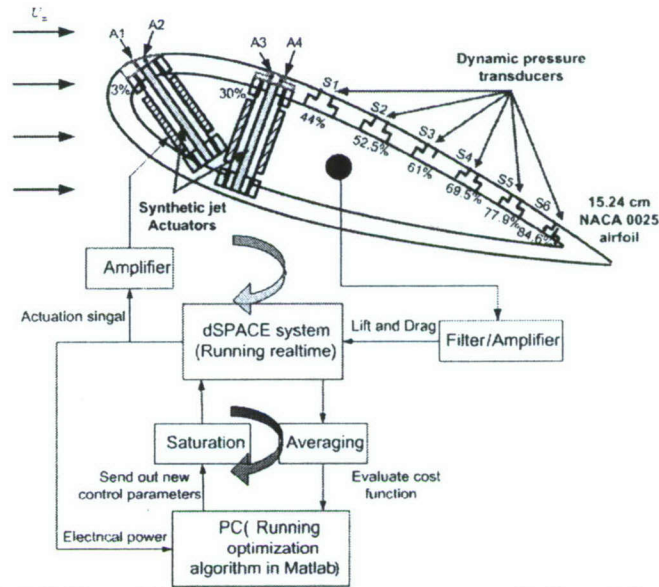
Figure 5-17. NACA 0025 airfoil model with actuators, sensors and closed-loop control system.
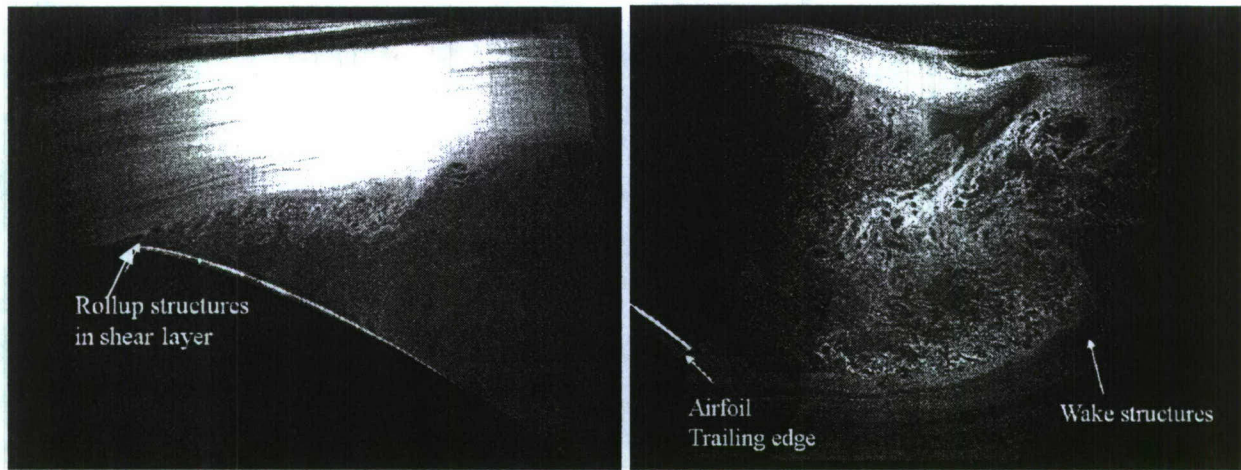
Figure 5-18. Flow structures in separated flow.
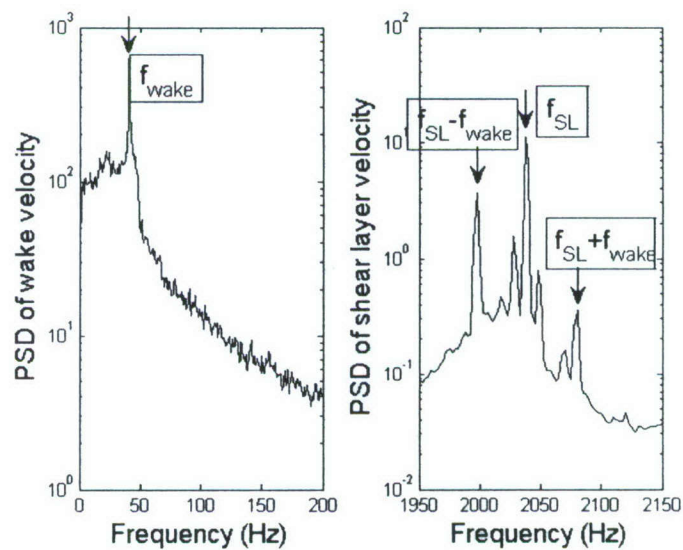
Figure 5-19. Wake (1 chord aft of TE) and shear layer (near separation) power spectral density functions at peak rms location.
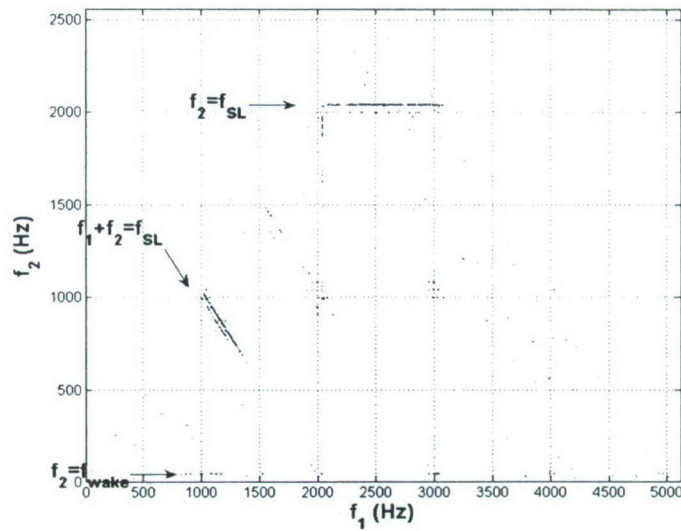
Figure 5-20. Auto-bicoherence of the same velocity signal analyzed in Figure 5-19 using the same parameter settings. The auto-bicoherence is zero except where nonlinear phase quadratic phase coupling occurs due to interactions between the shear layer and wake instabilities.
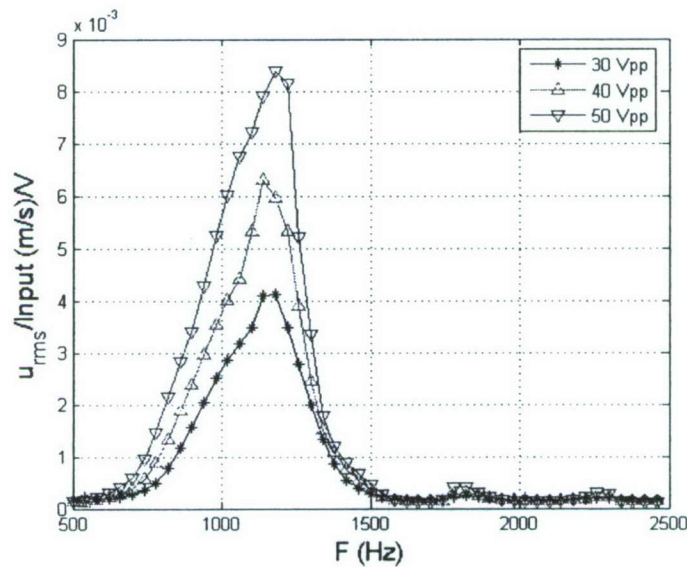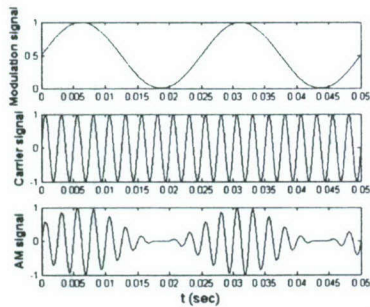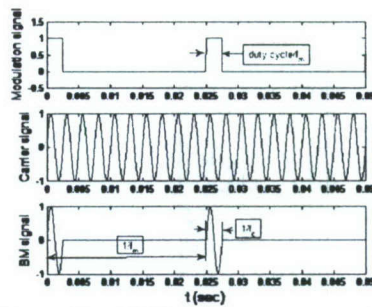

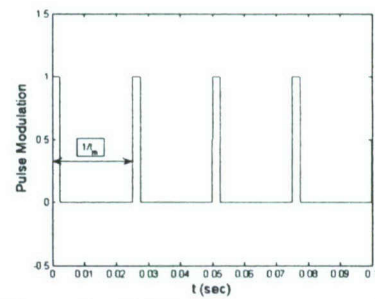Figure 5-21. Frequency response of ZNMF actuator A1.

(a) amplitude modulation (AM)

(b) burst modulation (BM)

(c) pulse modulation (PM)

Figure 5-22. Various waveforms of unit amplitude $A=1$ that can be used to excite multiple instabilities or modes in a separated flow.
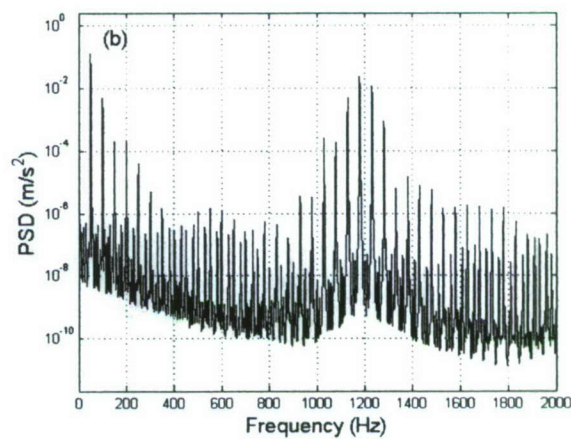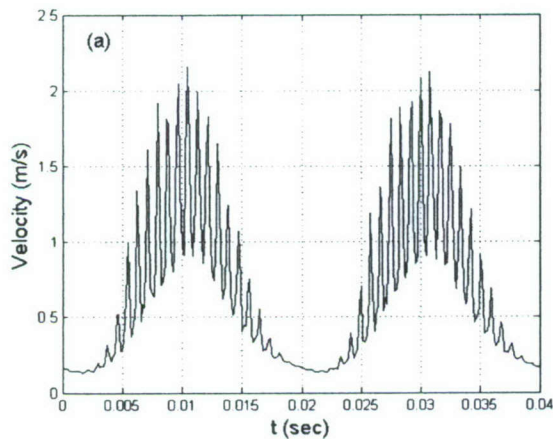

Figure 5-23. Velocity response (a) and its power spectral density (b) subject to an AM excitation for the ZNMF actuator A1. $A=50$ V_{pp}, $f_m=50$ Hz and $f_c=1180$ Hz. Measurements were made outside the region of reverse flow.

Figure 5-24. C_μ (a) and electrical power (b) profile subject to AM excitation. Five actuation amplitudes (30 V_{pp}, 35 V_{pp}, 40 V_{pp}, 45 V_{pp} and 50 V_{pp}) are shown.

Figure 5-25. C_μ (a) and electrical power (b) profile subject to BM excitation. Five actuation amplitudes (30 V_{pp}, 35 V_{pp}, 40 V_{pp}, 45 V_{pp} and 50 V_{pp}) are shown.
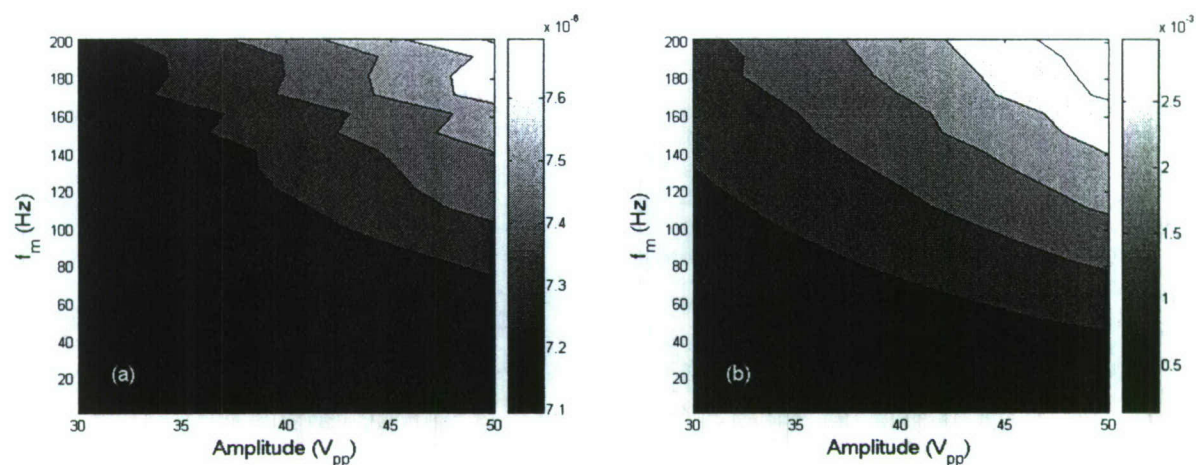
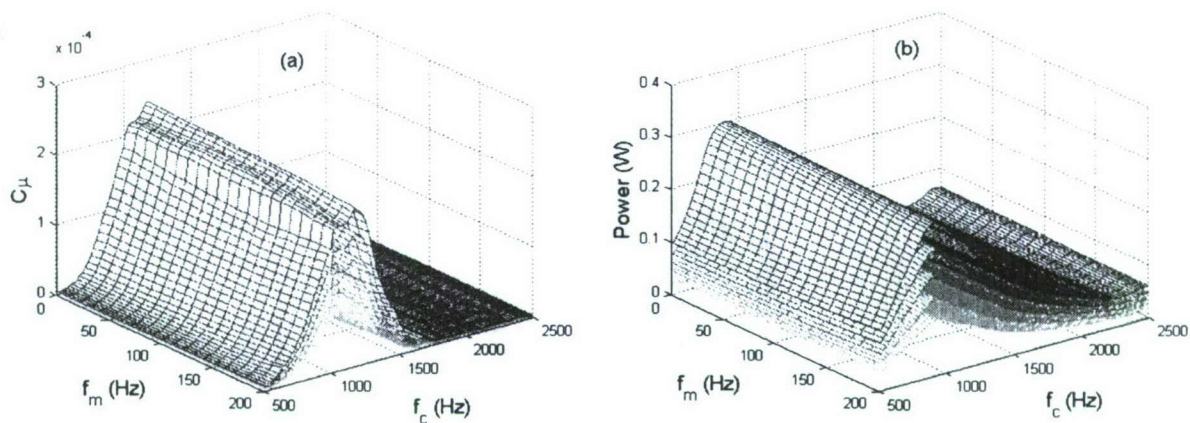Figure 5-26. C_μ (a) and electrical power (b) profile subject to PM excitation. Five actuation amplitudes (30 V_{pp}, 35 V_{pp}, 40 V_{pp}, 45 V_{pp} and 50 V_{pp}) are shown.
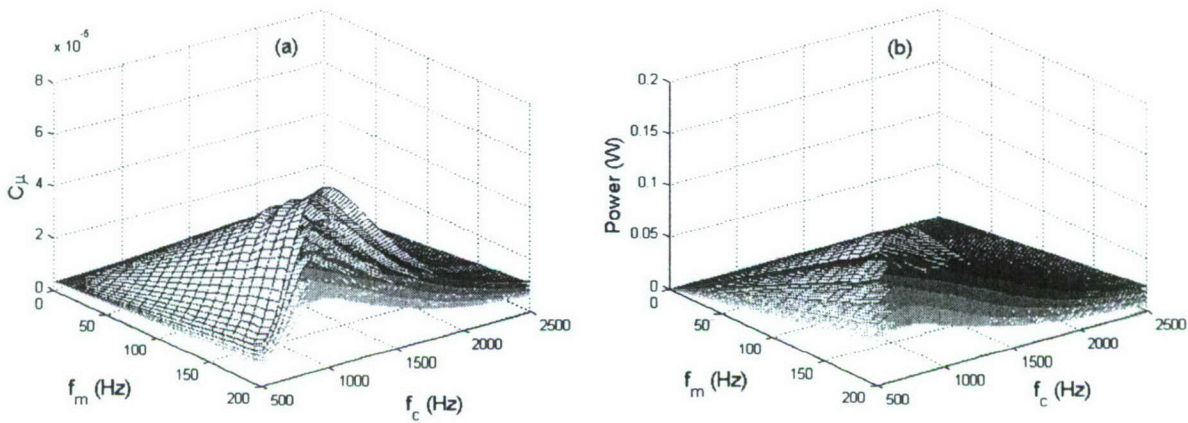

Figure 5-27. Constrained search using AM: Cases (a) and (b). The shaded area denotes the constraint area and amplitude is adjusted at each step to satisfy the constraint criteria. AOA = 20 deg. and Re = 120,000.

Figure 5-28. Constrained search using BM: Cases (a) and (b). The shaded area denotes the constraint area and amplitude is adjusted at each step to satisfy the constraint criteria. AOA = 20 deg. and Re = 120,000.

Figure 5-29. Constrained search using PM: Cases (a) and (b). AOA = 20 deg. and Re = 120,000.

6   Summary and Future Work
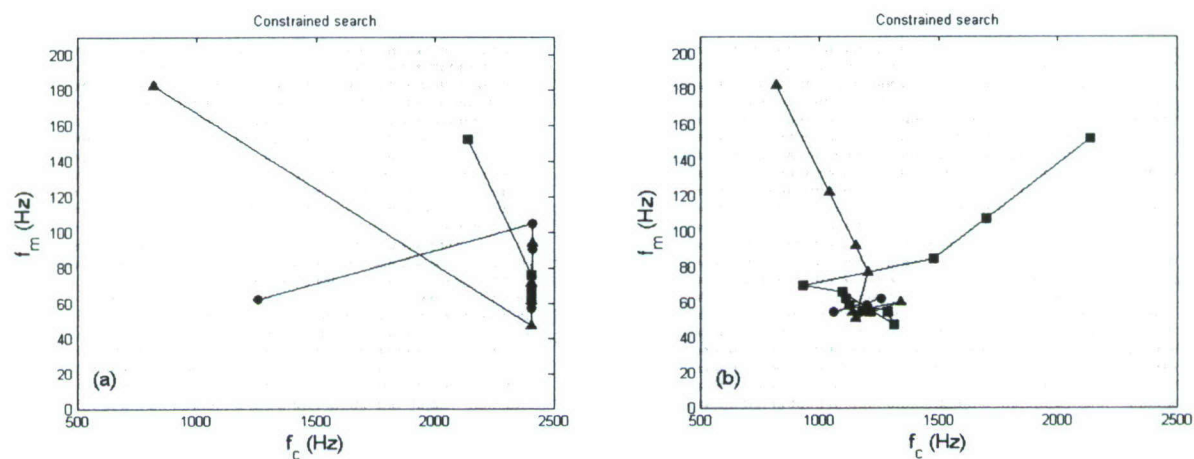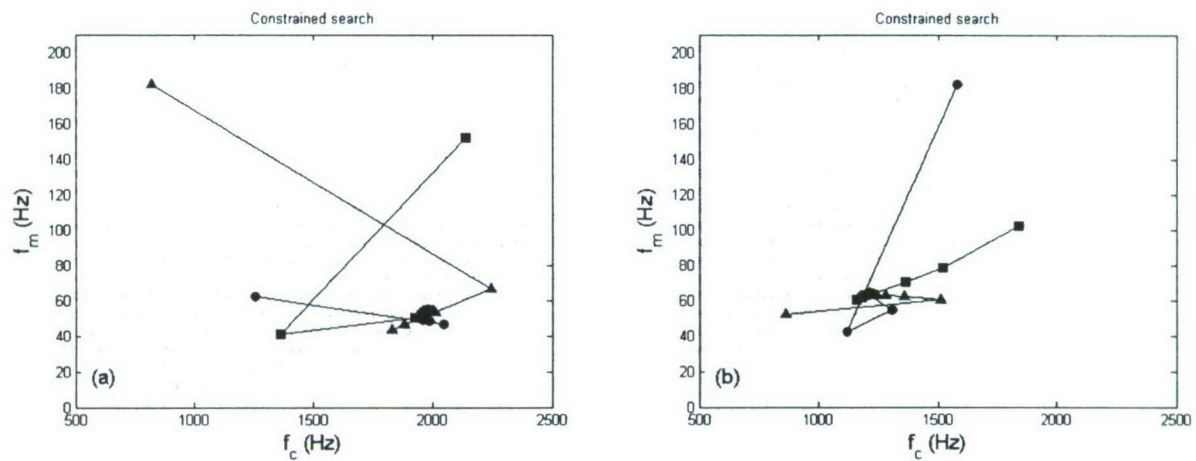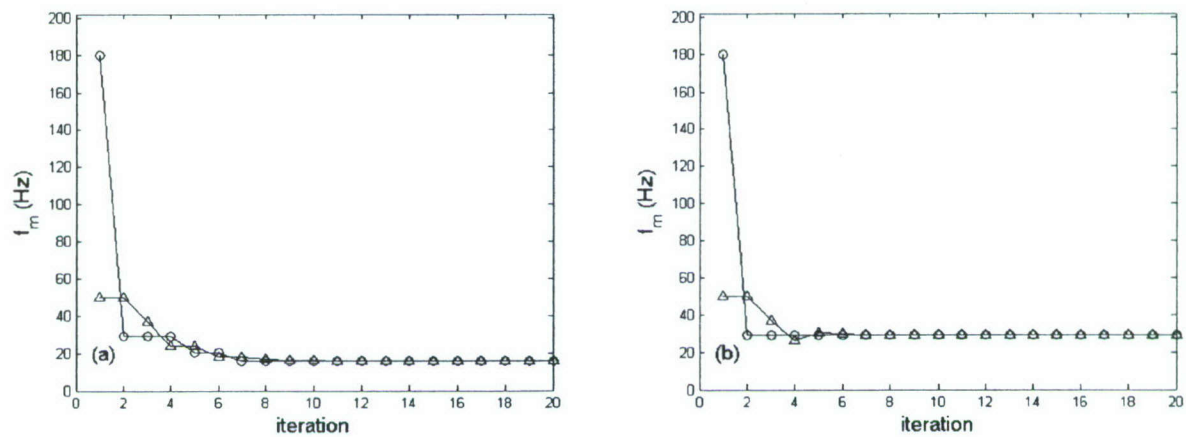
An adaptive system identification and feedback control algorithm is applied to the separation control problem for a NACA 0025 airfoil at nominal angles of attack of 12° and 20° and a chord Reynolds number of 120,000 with a tripped boundary layer, corresponding to control of a massively leading-edge separated flow. In particular, a recursive ARMARKOV system ID algorithm is used to model the flow dynamics and provide the information required to implement the disturbance rejection algorithm in real time with no prior knowledge of the system dynamics. Phase-locked PIV and fluctuating surface pressure measurements provided evidence of the link between the separated flow vertical structures and the surface pressure fluctuations. The chosen control objective was thus to suppress the airfoil surface pressure fluctuations. The disturbance rejection algorithm was able to automatically generate control input to the ZNMF actuator, emphasizing low (i.e., wake) and high (i.e., shear layer) characteristic frequencies of the separated flow. The effect of the control is to enhance near-wall mixing and suppress the highly unsteady flow structures. This adaptive control scheme is able to completely reattach the flow using low (~12.7 mW) power to a single piezoelectric synthetic jet actuator. The closed-loop control results show ~ 7 x improvements in the lift/drag ratio, with a corresponding increase in lift and reduced drag and concomitant reductions in the fluctuating surface pressure spectra. The present results are, to the best of our knowledge, the first experimental demonstration of an adaptive dynamic feedback control of a separated flow. The results reveal the tremendous potential of closed-loop flow control to real aircraft applications but also reveal key issues worthy of further study.

First, in terms of positives, the adaptive closed-loop control scheme has several attractive features. It is quite general, and no prior knowledge of the system dynamics is required. The system identification and disturbance rejection algorithms are integrated, and the system dynamics can be obtained with minimal a priori user knowledge. The controller is implemented using DSP hardware and can be easily incorporated in hardware-in-the-loop applications. It can be applied to not only flow separation control problems, but also, for example, cavity oscillation control and turbulent boundary layer control.

Second, in terms of unresolved technical issues, there remain many concerning the actuator and sensor dynamics. Clearly, better actuators with not just higher output but flatter dynamic response over wider frequency range are desirable. While measuring unsteady surface pressure is relatively straightforward, the potential acoustic contamination issue was highlighted. This difficulty was mitigated with an acoustic digital filter here but at the cost of additional computational complexity from an already limited DSP. This issue suggests the use of alternate surface sensors, such as MEMS-based direct shear stress sensors for feedback instead of pressure sensors. Or perhaps thermal sensors may be sufficient despite their sensitivity to more than just shear stress. Ultimately, it is believed that the key limitation of the present scheme, as evidenced by its failure at higher angles of attack, include the assumption of linearity in the system identification and disturbance rejection algorithm. The second part explores nonlinear control methods.

In the post-stall separated flow where the flow does not reattach, there are two characteristic instabilities: the shear layer Kelvin-Helmholtz instability and wake instability. Our experiments have the evidence for such instabilities. In addition, the second order spectral

analysis has quantified the quadratic phase coupling between the two instabilities, which indicates the separated flow is a complex multi-frequency system.

Three multi-modal waveforms (namely amplitude modulation, burst modulation and pulse modulation) are used targeting excitation of the multi-frequency separated flow system. A simplex optimization approach for controlling the separated flow has been developed to search for the optimal actuation parameters of the three waveforms using the ZNMF devices. It is typical for the C_μ response to vary when the waveform frequency parameters vary for the ZNMF devices. This can potentially lead to misleading results about the optimal forcing frequency. The actuator dynamics is taken into consideration in the optimization approach. To offset the actuator dynamics implications, a special routine is devised to hold the C_μ at constant during the optimization process utilizing the pre-calibrated actuator response profiles. This is specifically done by varying the actuation voltages according to the response profiles to keep the C_μ at constant levels.

The constrained optimization results seeking to maximize L/D are promising and reveal the importance of forcing nonlinear interactions between the shear layer and wake instabilities. Effective separation control is achieved by using oscillatory momentum coefficients $O(10^{-6}\text{-}10^{-5})$, which is more than an order-of-magnitude smaller than typical values reported in the literature (see summary in Greenblatt and Wygnanski 2000). Specifically, the optimized carrier frequency f_c targets the shear layer frequency while the optimized modulation frequency f_m targets the wake frequency and its super-harmonics. The nonlinear control is able to achieve similar performance at AoA=12° and much better performance than the dynamic control in our companion study at AoA=20°. The nonlinear control approach benefits from the nonlinear coupling of the flow instabilities and the integrated performance (L/D) measurements instead of local unsteady pressure measurements.

7 List of References

Akers, J. C. and Bernstein, D. S., "ARMARKOV Least-Squares Identification", Proceeding of the American Control Conference, pp. 191-195, New Mexico, June 1997A.

Akers, J. C. and Bernstein, D. S., "Time-Domain Identification Using ARMARKOV/Toeplitz Models", Proceeding of the American Control Conference, pp. 186-190, New Mexico, June 1997B.

Allan, B., Juang, J., Seifert A., Pack L. and Brown, D, "Closed-loop Separation Control Using Oscillatory Flow," ICASE Report No. 2000-32.

Amitay, M, and Glezer, A., "Controlled transients of flow reattachment over stalled airfoils," Heat and Fluid Flow, vol 23, pp 690 – 699, 2002.

Amitay, M., Smith, D., Kibens, V., Rarekh, D. and Glezer A., "Aerodynamic Flow Control over an Unconventional Airfoil Using Synthetic Jet Actuators," AIAA Journal, Vol. 39 No.3, pp 361-370, , March 2001.

Artiyur, K. B. and Krstic, M., Real-Time Optimization by Extremum-Seeking Control, Wiley-Interscience, 2003.

Ausseur, J.M., Pinier, J.T., Glauser, M.N and Higuchi, H., "Controller Development for Closed-Loop Feedback Control of Flows," 35th AIAA Fluid Dynamics Conference and Exhibit, AIAA-2005-5264, Toronto, Canada, 2005.

Ausseur, J., Pinier, J. and Glauser, M, "Flow Separation Control Using a Convection Based POD Approach," 3rd AIAA Flow Control Conference, AIAA-2006-3017, San Francisco, California, 2006.

Banaszuk, A., Narayanan S. and Zhang Y., "Adaptive Control of Flow Separation in a Planar Diffuser," AIAA paper 2003-0617, 2003.

Bendat, J.S. and Piersol, A.G., "Random Data: Analysis & Measurement Procedures, 3rd ed.", Wiley-Interscience, 2000.

Becker, R., King, R., Petz, R. and Nitsche, W., "Adaptive Closed-Loop Separation Control on a High-Lift Configuration using Extremum Seeking", AIAA 2006-3493, June 2006.

Camacho, E.F. and Bordons, C., Model Predictive Control in the Process Industry, Springer-Verlag Berlin Heidelberg New York, 1995.

Cattafesta, L.N., Garg, S., Choudhari, M. and Li, F., "Active Control of Flow –Induced Cavity Resonance," AIAA –97- 1804, 1997.

Cattafesta, L. N., Shulkla, D., Garg, S. and Ross, J.A., "Development of an Adaptive Weapons-Bay Suppression System," AIAA- 99 – 1901, 1999.

Cattafesta, L.N., Garg, S. and Shukla, D., "Development of Piezoelectric Actuators for Active Flow Control," AIAA Journal, Vol. 39, No. 8, Aug. 2001.

Clarke, D.W., D. Phil, M. A., Gawthrop, P. J. and D. Phil, B. A., "Self-Tuning Control," IEEE Proc., Vol. 126, No. 6, June 1979.

Clarke, D.W., Mhtadi C. and Tuffs, P.S., "Generalized Predictive Control-Part I. The Basic Algorithm," Automatica, Vol. 23, No. 2, pp. 137-148, 1987A.

Clarke, D.W., Mhtadi C. and Tuffs, P.S., "Generalized Predictive Control-Part II. Extensions and Interpretations," Automatica, Vol. 23, No. 2, pp. 149-160, 1987B.

Clarke, D.W.,"Application of Generalized Predictive control to industrial Processes," IEEE Control Systems Magazine, pp. 49-55, April 1988.

Coller, B., Noack, B., Narayanan, S., Banaszuk, A. and Khibnik, A., "Reduced-Basis Model for Active Separation Control in a Planar Diffuser Flow", AIAA 2000-2562, 2000.

Crook, A., Sadri, A. M. and Wood, N. J., "The Development and Implementation of Synthetic Jets for the Control of Separated Flow," AIAA-99–3176, 1999.

Cutler, C.R, and Ramaker, B.L., "Dynamic Matrix Control- A Computer Control Algorithm," Proc. JACC, San Francisco, WP5-B, 1980.

Gad-el-Hak M., Flow Control: Passive, Active, and Reactive Flow Management, Cambridge, 2000.

Gallas, Q., Holman, R., Nishida, T., Carroll, B., Sheplak, M., and Cattafesta, L., "Lumped Element Modeling of Piezoelectric-Driven Synthetic Jet Actuators," AIAA Journal, Vol. 41, No. 2, pp. 240-247, 2003.

Gallas, Q., Ph.D Thesis, University of Florida, 2005.

Golub, G. H. and Van Loan, C. F., Matrix Computations, 3rd ed., Baltimore, MD: Johns Hopkins, 1996.

Greenblatt, D and Wygnanski, I, "Dynamics Stall Control by Periodic Excitation, Part 1: NACA 0015 Parametric Study," Journal of Aircraft, Vol. 38, No. 3, May- June 2001A.

Greenblatt, D and Wygnanski, I, "Dynamics Stall Control by Periodic Excitation, Part 1: Mechanisms," Journal of Aircraft, Vol. 38, No. 3, May- June 2001B.

Greenblatt, D and Wygnanski, I, "Effect of Leading-Edge Curvature on Airfoil Separation Control," Journal of Aircraft, Vol. 40, No. 3, May-June 2003.

Greenblatt, D and Wygnanski, I, "The control of flow separation by periodic excitation," Progress in Aerospace Sciences, Elsevier Science Ltd, 36:487-545, 2000.

Greenblatt, D., Nishri, B., Darabi A. and Wygnanski, I. "Some Factors Affecting Stall Control with Particular Emphasis on Dynamic Stall," AIAA-99-3504, June-July 1999.

Griffin, B., Senior Thesis, 2003.

Haftka, R.T. and Gürdal, Z., Elements of Structural Optimization, 3rd edition, Kluwer, 1992.

Halfon, E., Nishri, B., Seifert, A. and Wygnanski, I., "Effects of Elevated Free-Stream Turbulence on Actively Controlled Separation Bubble", Journal of Fluids Engineering, Vol. 126, P 1015 – 1024, Nov. 2004.

Hajj, M. R., Miksad, R. W. and Powers, E.J., "Perspective: Measurements and Analyses of Nonlinear Wave Interactions with Higher-Order Spectral Moments", Journal of Fluids Engineering, v119, Mar. 1997, pp 3-13.

Haykin, S., Adaptive Filter Theory, 4th edition, Prentice Hall, 2002.

Ho, C. M. and Huerre, P, "Perturbed Free Shear Layers," Annual Review Fluid Mechanics, 16: 365-424, 1984.

Holland, J., Adaptation of Natural and Artificial Systems, The University of Michigan Press, Ann Arbor, MI, 1975.

Holman, R. and Gallas, Q., Carrol B. and Cattafestta, L.N., "Interaction of Adjacent Synthetic Jets in An Airfoil Separation Application," AIAA paper 2003-3709, June 2003.

Holmes, P., Lumley, J.L. and Berkooz, G., Turbulence, Coherent Structures, Dynamical Systems and Symmetry. Cambridge University Press, Cambridge, 1998.

Hong, J. and Bernstein, D., "Bode Integral Constraints, collocation, and Spillover in Active Noise and Vibration control, " IEEE Transactions on Control Systems Technology, vol. 6, No.1, January, 1998.

Honohan, A. M., Amitay, M., and Glezer, A., "Aerodynamic Control Using Synthetic Jets," AIAA-2000-2401, 2000.

Hsiao, F.-B., Liu, C.F., and Shyu, J.-Y., "Control of Wall-Separated Flow by Internal Acoustic Excitation," AIAA Journal, Vol. 28, No. 8, pp 1440-1446, 1990.

Huang, L.S., Maestrello, L. and Bryant, T.D., "Separation Control over an Airfoil at High Angle of Attack by Sound Emanating from the Surface," AIAA Paper 87-1261, 1987.

Huerre, P. and Monkewitz, P., "Local and Global Instabilities in Spatially Developing Flows," Annual Review Fluid Mechanics,. 22: pp 473-537, 1990.

Johnson, C. R., and Larimore, M. G., "Comments on and Additions to 'An Adaptive Recursive LMS Filter'", Proc. of the IEEE, Vol. 65, No. 9, pp 1399-1402, Sep. 1977.

Jørgensen, F. E., "The Computer-Controlled Constant-Temperature Anemometer. Aspects of Set-up, Probe Calibration, Data Acquisition and Data Conversion", Meas. Sci. Technol. 7, pp 1378-1387, 1996.

Juang, J., Applied System Identification, Prentice-hall, New Jersey, 1994.

Juang, J.N. and Phan, M.Q., "Deadbeat Predictive Controllers," NASA TM 112862, May, 1997.

Juang, J.N. and Phan, M.Q., "Identification and Control of Mechanical Systems," Cambridge University Press.

Kegerise, M. A., Spina, E. F., Garg, S. and Cattafesta, L., "Mode-Switching and Nonlinear Effects in Compressible Flow over a Cavity", Physics of Fluids, v16 n3, Mar. 2004, pp 678 – 687.

Kegerise, M.A., Cattafesta L.N. and Ha, C., "Adaptive Identification and Control of Flow-Induced Cavity Oscillations," AIAA Paper 2002-3158, June 2002.

Kennedy, J., "The particle swarm: social adaptation of knowledge," Proc. Intl. Conf. on Evolutionary Computation, Indianapolis, IN, 303-308. Piscataway, NJ: IEEE Service Center, 1997.

Kumar, V. and Alvi, F. S., "Efficient Control of Separation Using Microjets," AIAA Paper 2005-4879, June 2005.

Kuo, S.M. and Morgan, D.R., "Active Noise Control: A Tutorial Review," Proceedings of the IEEE, Vol. 87, No. 6, June 1999.

Kuo, S.M. and Morgan, D.R., Active Noise Control Systems, New York: Wiley, 1996.

Kuo, S.M., Kong X. and Gan W. S., "Application of Adaptive Feedback Noise Control System," IEEE Transactions on Control Systems Technology, Vol. 11, No. 2, March 2003.

Larimore, M. G., Johnson, C. R., and Shah, N., Theory and Design of Adaptive Filters, Pearson Education, Mar. 2001.

Ljung, L., System Identification: Theory for the User, Prentice Hall PTR, Upper Saddle River, New Jersey, 1987.

Lee, K.H., Cortelezzi, L., Kim J. and Speyer J.," Application of reduced-order controller to turbulent flows for drag reduction", Physics of Fluids, Vol. 13, NO. 5, 2001.

Margalit, S., Greenblatt, D., Seifert, A., and Wygnanski, I., "Active Flow Control of a Delta Wing at High Incidence using Segmented Piezoelectric Actuators," AIAA-2002-3270, 2002.

Mittal, R., Kotapati, B. and Cattafesta, L., "Numerical Study of Resonant Interactions and Flow Control in a Canonical Separated Flow," AIAA paper 2005-1261, Reno, Nevada, Jan. 2005.

Mittal, R. and Rampunggoon, P., "On the Virtual Aero-Shaping Effect of Synthetic Jets," Phys. Fluids, vol. 14, no. 4., pp. 1533-1536, 2002.

Morari, M. and Ricker, N.L., "Model Predictive Control Toolbox," User's Guide, The MathWorks, Version 1, October, 1998.

Narayanan, S. and Banaszuk A., "Experimental Study of a Novel Active Separation Control Approach," AIAA paper 2003-60, Reno, Nevada, Jan. 2003.

Netto, S. L., and Diniz, P. S. R, "Composite Algorithms for Adaptive IIR Filtering", Electronics Letters, Vol. 28 No. 9, p. 886-888, 23rd Apr. 1992.

Netto, S. L., and Diniz, P. S. R., "Adaptive IIR Filtering Algorithm for System Identification: A General Framework", IEEE Transactions on Education, Vol. 38, No. 1, Feb. 1995.

Nishri, B. and Wygnanski I., "Effects of Periodic Excitation on Turbulent Flow Separation from a Flap," AIAA Journal, Vol. 36, No.4, April 1998.

Nikias, C.L. and Mendel, J.M., "Signal Processing with Higher-Order Spectra," IEEE Signal Processing Magazine, 1053-5888, July 1993.

Nikias, C. L. and Petropulu, A. P., Higher-Order Spectra Analysis – A Nonlinear Signal Processing Framework, Prentice-Hall, Upper Saddle River, NJ, 1993.

Ol, M., McCauliffe, B., Hanff, E., Scholz, U., and Kaehler, C. "Comparison of Laminar Separation Bubble Measurements on a Low Reynolds Number Airfoil in Three Facilities ," AIAA-2005-5149, June 2005.

Pack, L., Schaeffler, N., Yao, C., and Seifert, A., "Active Control of Flow Separation from the Slat Shoulder of a Supercritical Airfoil," AIAA-2002-3156, 2002.

Pinier, J.T., Ausseur, J.M., Glauser, M.N and Higuchi, H., "Proportional Closed-loop Feedback Control of Flow Separation," AIAA Journal, in review.

Pillarisetti, A. and Cattafesta, L. N., "Adaptive Identification of Fluid-Dynamic Systems," AIAA Paper 2001-2978, June 2001.

Prandtl, L. Proceedings of Third International Mathematical Congress, Heidelberg, pp 484-491, 1904.

Prasad, A. and Williamson, C., "The Instability of the Separated Shear Layer from a Bluff Body," Physics of Fluids, Vol. 8, No.6, pp 1347-1349, June 1996.

Press, W. H., Flannery, B. P., Teukolsky, S. A. and Vetterling, W. T., Numerical Recipes in Fortran, 2nd edition (January 15, 1992), Cambridge University Press.

Raju, R., Mittal, R., and Cattafesta, L., "Towards Physics Based Strategies for Separation Control over an Airfoil using Synthetic Jets," AIAA Paper 2007-1421, January 2007.

Rathnasingham, R. and Breuer K., "Active Control of Turbulent Boundary Layers," Journal of Fluid Mechanics, Vol 495, pp. 209-233, 2003.

Rathnasingham, R. and Breuer K., "System Identification and Control of Turbulent Boundary Layer," Phys. Fluids, pp1867-1869, July 1997.

Roshko, A. "On the Development of Turbulent Wakes from Vortex Streets," NACA Report 1191, 1954.

Rouhani, R., and Mehra, R.K., "Model Algorithmic Control (MAC), Basic Theoretical Properties," Automatica, Vol. 18, No. 1, pp.401-414, 1982.

Sane, H.S., Venugopal, R. and Bernstein, D.S., "Disturbance Rejection Using Self-Tuning ARMARKOV Adaptive Control with Simultaneous Identification," IEEE Transactions on Control Systems Technology, Vol. 9, No. 1, January 2001.

Schubauer, G.B. and Skramstad H.K., "Laminar boundary layer oscillations and transition on a flat plate," NASA Report 909, 1948.

Seifert, A., Darabi, A. and Wygnanski, I., "Delay of Airfoil Stall by Periodic Excitation," Journal of Aircraft, Vol. 33, No. 4, July- August 1996.

Seifert, A. and Pack, L. G., "Compressibility and Excitation Location Effects on High Reynolds Numbers Active Separation Control," Journal of Aircraft, Vol. 40, No. 1, Jan. – Feb. 2003 A.

Seifert, A. and Pack, L. G., "Effects of Sweep on Active Separation Control at High Reynolds Numbers," Journal of Aircraft, Vol. 40, No. 1, Jan. – Feb. 2003 B.

Seifert, A., Pack, L. G., "Active Flow Separation Control on Wall-Mounted Hump at High Reynolds Numbers," AIAA Journal, Vol. 40, No.7, July 2002.

Seifert, A., Pack, L. G., "Oscillatory Control of Shock-Induced Separation," Journal of Aircraft, Vol. 38, No. 3, May – June 2001.

Seifert, A., Pack, L. G., "Separation Control at Flight Reynolds Numbers: Lessons Learned and Future Directions," AIAA paper 2000-2542, June 2000.

Seifert, A., Pack, L. G., "Oscillatory Control of Separation at High Reynolds Numbers," AIAA Journal, Vol. 37, No.9, pp 1062-1071, Sep. 1999.

Sheplak, M., Cattafesta, L., and Tian, Y. "Micromachined Shear Stress Sensors for Flow Control Applications," IUTAM Symposium on Flow Control and MEMS, London, September 2006.

Shynk, J. J., "Adaptive IIR Filtering", IEEE ASSP Magazine, p. 4-21, Apr. 1989.

Sinha, S.K., "Flow Separation Control with Microflexural Wall Vibrations," Journal of Aircraft, Vol. 38, No.3, May-June 2001.

Soderstrom, T. and Stoica, P., System Identification, Prentice-Hall, New York, 1989.

Song, Q., Tian, Y. and Cattafesta, L., "MIMO Feedback Control of Flow Separation", AIAA Paper 2007-0109, Jan. 2007.

Tadmor, G., Centuori, M., Noack, B., Luchtenburg, M., Legmann, O. and Morzyński, M., "Low Order Galerkin Models for the Actuated Flow Around 2-D Airfoils", AIAA 2007-1313, January, 2007.

Tian, Y., Cattafesta, L., and R. Mittal, "Adaptive Control of Separated Flow," AIAA Paper 2006-1401, Jan. 2006.

Tian, Y., Song, Q., and Cattafesta, L., "Adaptive Feedback Control of Flow Separation," 3rd Flow Control Conference, San Francisco, CA, AIAA-2006-3016, June 2006.

Venugopal, R. and Berstein D.S., "Adaptive Disturbance Rejection Using ARMARKOV System Representation," Proceeding of the 36th Conference on Decision & Control, pp1884-1889, Dec. 1997.

Wang, Y., Haller, G., Banaszuk, A. and Tadmor, G., "Closed-Loop Lagrangian Separation Control in a Bluff Body Share Flow Model", Physics of Fluids, Vol. 15, No. 8, P 2251 – 2266, August, 2003.

White, F. M., Viscous Fluid Flow, 2nd edition, McGraw-Hill, 1991.

Wiltse, J. N. and Glezer, A., "Manipulation of Free Shear Flows Using Piezoelectric Actuators," Journal of Fluid Mechanics, vol. 249 pp. 261-285, 1993.

Wu, J. -Z., Lu, X. -Y., Denny, A. G., Fan, M., and Wu, J. -M. "Post-Stall Flow Control on an Airfoil by Local Unsteady Forcing," J. Fluid Mech., vol. 371, pp. 21-58, September 1998.

Wygnanski, I., "Some New Observations Affecting the Control of Separation by Periodic Forcing,"AIAA-2000-2314, 2000.

Zhou, Kemin, Essentials of robust control, Prentice-Hall, New Jersey, 1998.